EXAMINING TISSUE MICROSTRUCTURE WITH TEMPORAL DIFFUSION MAGNETIC RESONANCE SPECTROSCOPY

By

Daniel Christopher Colvin

Dissertation

Submitted to the Faculty of the

Graduate School of Vanderbilt University

in partial fulfillment of the requirements

for the degree of

DOCTOR OF PHILOSOPHY

in

Physics

December, 2009

Nashville, Tennessee

Approved:

Professor John C. Gore

Professor Mark D. Does

Professor Adam W. Anderson

Professor Bruce M. Damon

Professor David J. Ernst

For Jason Andrew Myers

Absens sed non in oblivione

ACKNOWLEDGEMENTS

The research outlined in this dissertation would not have been possible without the financial support of NIH grants U24CA126588, 1K25 EB005936, RO1CA109106, R01NS034834, R01EB00214 and P30 CA68485, as well as the support of the Vanderbilt University Institute of Imaging Science (VUIIS). I am particularly grateful to my advisor, Dr. John Gore, for providing me with the opportunity, support, and guidance in achieving my academic and research goals. I consider myself very fortunate to have been a part of the VUIIS these past years. I have not only had the opportunity to work with exceptional people at a premiere imaging facility, but I have also had the good fortune of making some wonderful friends along the way.

I would also like to thank Dr. Mark Does for the significant insight he has provided regarding many of my studies, as well as for his guidance with numerous hardware and software related issues. I am also grateful to Dr. Adam Anderson and Dr. Bruce Damon for numerous helpful conversations along the way, as well as to Ken Wilkens and Jarrod True for all of their technical assistance.

Last, but not least, I would like to thank my family and friends, who have been unbelievably supportive throughout my graduate career. They have been there with me through all the ups and downs, and the hard work I have invested over these past years would mean nothing if I couldn't share the rewards with them.

TABLE OF CONTENTS

LIST OF FIGURES

CHAPTER V

CHAPTER VI

LIST OF TABLES

Table Page

LIST OF ABBREVIATIONS

VUIIS (Vanderbilt University of Imaging Science)

NMR (Nuclear Magnetic Resonance)

MRI (Magnetic Resonance Imaging)

RF (Radiofrequency)

EM (Electromagnetic)

EPI (Echo Planar Imaging)

CAT (Computerized Axial Tomography)

PGSE (Pulsed Gradient Spin Echo)

ADC (Apparent Diffusion Coefficient)

OGSE (Oscillating Gradient Spin Echo)

CSAI (Center for Small Animal Imaging)

DMSO (Dimethyl Sulfoxide)

BSA (Bovine Serum Albumin)

PBS (Phosphate Buffered Saline)

CHAPTER I

PHYSICAL PRINCIPLES OF NMR AND MRI

Brief History of NMR

Magnetic Resonance Imaging (MRI) has become one of the most widely implemented imaging modalities in radiological science today. Yet the concept of receiving an MRI exam is relatively new, with the first *in vivo* anatomical images appearing just over three decades ago. Since Sir Peter Mansfield produced the first cross sectional image of human anatomy, a finger, in 1977, the field of MRI has progressed through tremendous advances in image quality and scanning efficiency, and witnessed the emergence and evolution of numerous imaging applications and research specializations. While a full account of these developments would be exhaustive, it is worth noting, in light of the concepts outlined in this thesis, several key innovations that paved the way to our understanding of the nuclear magnetic resonance (NMR) phenomenon.

Perhaps the most fundamental development in the history of NMR was the discovery of the spin nature of protons and electrons. Early experiments by Otto Stern and Walther Gerlach, as well as Wolfgang Pauli, had hinted at the existence of space quantization, but it wasn't until 1925 that scientists Samuel Goudsmit and George Uhlenbeck interpreted this quantization as an intrinsic angular momentum of the electron itself, a property responsible for providing the electon with a magnetic moment (1-2). Several years later, in 1933, Otto Stern

confirmed that the proton exhibits spin as well (3). He was awarded the Nobel Prize in Physics in 1943 for his work.

Following upon the work of Stern and Gerlach, Isador Rabi, an American physicist at Columbia University, performed the first successful “molecular beam magnetic resonance” experiment in 1937 (4). In this experiment, Rabi demonstrated that the precessional frequency of the magnetic moments in lithium chloride molecules could be made to match the frequency of an applied radiofrequency (RF) field by adjusting the strength of an applied magnetic field. When the appropriate ‘resonance’ frequency was achieved, the molecules were able to absorb the RF energy, thereby inducing a transition in the spin state of the nuclei, and allowing for direct calculation of the strength of the magnetic moment. He continued to develop these resonance techniques to examine the magnetic properties and internal structure of other molecules, atoms, and nuclei and was awarded the Nobel Prize in Physics in 1944 for his work.

A few years later, in 1946, two scientists, Edwin Purcell at Harvard University and Felix Bloch at Stanford University, independently demonstrated a similar phenomenon using the hydrogen nucleus in condensed materials (5-6). They were able to show that the absorption and subsequent re-emission of radiofrequency energy by nuclear spins precessing in an applied magnetic field could be used to determine the chemical composition of a physical sample. Thus, NMR spectroscopy was born. For this, and related work, these scientists received the Nobel Prize in physics in 1952.

In 1950, E.L. Hahn published an article describing “spin echoes,” a nuclear magnetic resonance signal induced by a succession of radio-frequency pulses applied to freely precessing magnetic moments (7). In 1973, chemist Paul Lauterbur demonstrated that the application of a magnetic field gradient across a sample could be used to spatially label a spin’s position, and thus, could be used to create a map, or image, of spin locations (8). Around this time, Raymond Damadian demonstrated that a fundamental property of spin precession, a phenomenon known as spin relaxation, could be used to delineate tissue types, thus distinguishing healthy tissue from that of diseased tissue (9). This insight perhaps provided the motivation for application of NMR techniques to medical and biological problems, and in particular, the diagnosis of cancerous tissues in human patients. In 1974, Richard Ernst introduced the concept of frequency and phase encoding with pulsed magnetic field gradients, which could be analyzed with a Fourier transform to produce a two-dimensional image (10). He was awarded the Nobel Prize in Chemistry in 1991 for his work. A few years after this discovery, in 1976, Sir Peter Mansfield developed a mathematical framework for analyzing NMR signals, and developed a fast imaging techniques known as echo-planar imaging (EPI), which was deemed crucial to the development of this imaging technique in clinically feasible times (11-12). Sir Peter Mansfield and Paul Lauterbur received the Nobel Prize in 2003 for their work.

While the previously described achievements may be the most widely cited in references concerning the history of NMR, there are notable other

events, although seemingly unrelated to NMR, which have contributed significantly to the field. From Joseph Larmor, who determined the relationship between a precessing electron (or proton) and an applied magnetic field, to Joseph Fourier, who provided the theoretical analysis for connecting time-frequency data through a series of oscillatory functions, the modern concept of MRI could not be realized without the contributions of numerous scientists over several decades. Furthermore, while the events just outlined provide a rough overview of the evolution of basic NMR imaging research, the development of each specific imaging application and research specialization has a history of its own. In the following sections, a more thorough description of these achievements will be outlined, in the language of physics and mathematics, and the development of one particular area of NMR research, diffusion-weighting imaging, will be thoroughly explored.

Nuclear Magnetization

The previous introductory section of this dissertation summarized the historical scientific achievements that paved the way to current state of NMR techniques. In the sections that follow, the physical principles that govern the NMR experiment will be further explained, in the language of physics and mathematics. This includes a thorough description of relevant NMR physics, including spin dynamics, NMR relaxation, and advanced imaging techniques, followed by a chapter describing the physical laws of diffusion, particularly as they relate to NMR studies. Subsequent chapters will then focus upon the

application of these specialized NMR techniques to specific areas of biomedical interest.

It has been known since the 1920's that subatomic particles, such as protons and electrons, possess a fundamental property known as spin, which gives rise to the nuclear magnetic resonance phenomenon. While a thorough description of this spin property would require the language of quantum mechanics, a classical electrodynamic treatment is sufficient for describing most of the physics relevant to NMR experiments on water protons, and will be outlined in the following pages. Furthermore, while it is known that protons, neutrons, and electrons all possess this fundamental property, the focus here shall remain solely on the proton, for reasons that will be discussed following some introductory physics.

It has already been stated that protons possess an intrinsic angular momentum analagous to a particle spinning on its own axis. Since the proton is also known to possess an electrical charge, this spinning charge behaves like a tiny loop of electric current, which according to Ampere's law, will induce a magnetic dipole moment. This magnetic dipole then behaves like a microscopic bar magnet, free to interact with external electromagnetic (EM) fields in the radiofrequency (RF) range. It is the manipulation of these proton spins with RF energy that gives rise to the NMR experiment. (It should be noted that the neutron, despite its electrical neutrality, also possesses this property, as it is composed of smaller particles known as quarks, which are known to contain both charge and spin as well.)

Quantitatively, the magnetic moment μ of a proton is proportional to the spin angular momentum S:

$$\vec{\mu} = \gamma \vec{S} \tag{1.1}$$

by a constant of proportionality, γ, which is *approximately* equal to the particle's charge over twice its mass. If a single spin is placed in an external magnetic field $\vec{B}$, the magnetic potential energy will described by the Hamiltonian:

$$H = -\vec{\mu} \cdot \vec{B} \tag{1.2}$$

If we suppose that this external field $\vec{B}$ is aligned along the z-axis of a laboratory reference frame such that:

$$\vec{B} = |B|\hat{z} \tag{1.3}$$

then, combining equations 1.1, 1.2, and 1.3, the total energy (assuming zero kinetic energy) of the spin will be

$$\vec{H} = \gamma |B| \vec{S} \cdot \hat{z} \,. \tag{1.4}$$

Since the measured value of the spin, $\vec{S}$, along the z-axis can assume only quantized values, such that $S_z = m_s \hbar$, where $m_s = \pm \frac{1}{2}$ and $\hbar$ = Planck's constant, equation 1.4 becomes:

$$\vec{H} = \pm \frac{\gamma |B| \hbar}{2} \,. \tag{1.5}$$

The spin "up" proton is parallel to the external field and has lower energy (- sign), and the spin "down" proton is anti-parallel, with higher energy, (+ sign). The energy difference between these states is therefore:

$$\Delta E = E_{down} - E_{up} = \hbar\gamma\left|B\right| . \tag{1.6}$$

Therefore, the energy difference between the two quantum spin states is dependent upon the strength of the magnetic field as well as the gyromagnetic ratio, which is dependent upon the spin's charge and mass. A spin that exists in the higher energy state while experiencing the constant magnetic field $\vec{B}$ can make the transition to the lower energy state by releasing a photon of the appropriate energy, or conversely, move from the lower to the higher state by absorption of a photon.

Since we know that the energy of a photon is equal to $\hbar\omega$, we see from equation 1.6 that the resulting photon has angular frequency:

$$\omega_0 = \gamma B . \tag{1.7}$$

This relationship is known as the Larmor equation.

It should be noted here that, although every magnetic moment of every molecular species in the human body experiences the previously described phenomenon, the laws of physics restrict our NMR measurements to only a small class of spin-bearing particles. First, since nucleons "pair" themselves with other like nucleons of opposite spin (according to the Pauli exclusion principle), only nuclei containing an odd sum of protons and/or neutrons are suitable for NMR experiments. This is because only these odd mass number nuclei will have a nonzero spin angular momentum capable of producing the quantized magnetic moments that are measured. Furthermore, despite the abundance of electron spins in our body, their low mass makes them unsuitable for use in human

imaging. Because the gyromagnetic ratio of a particle is inversely proportional to its mass, the small mass of the electron produces an excessively large gyromagnetic ratio, γ, which in turn, produces an excessively large angular frequency, ω, even at low field strengths. The result is the need for photons in the microwave range of the spectrum, which are unsuitable for human imaging. Finally, although the isotopes of several other nuclei (^{14}N, ^{15}N, ^{19}F, ^{23}Na, ^{29}Si, ^{31}P, etc) are detectable with NMR methods, their relatively low abundance or low sensitivity make them less desirable for NMR studies. Fortunately, much of the human body is composed of water (H_20) or lipids (CH_2), both of which contain hydrogen atoms, each with a single nuclear proton - it is therefore this proton that is the most dominant (and commonly used) source of signal in NMR experiments, and thus, will be the focus of nearly all subsequent discussion.

However, despite the vast number of hydrogen protons in a single drop of pure water (~6.7 x 10^{22}/ml), NMR measurements are sensitive to only a very small fraction of these spins. In the absence of any external magnetic field, the magnetic moments of each spin within an ensemble of spins at room temperature is randomly orientated as a result of the continuous thermal agitation experienced by each of the particles, resulting in an overall net magnetization of zero. Placed within an external magnetic field, however, these spins will align themselves as described earlier, with *nearly* equal populations in the low and high energy states. From equation (1.6), for B = 1 Tesla,. Thus protons within the human body have a thermal energy, $kT \left(\sim \frac{1}{40}\, eV\right)$, that is millions of times larger than the transition energy of the spin states, $\hbar\omega$, there will be only a small

excess of protons existing in the lower energy state, according to Boltzmann statistics. Quantitatively, if an ensemble of *N* proton spins is in an external magnetic field at thermal equilibrium at typical lab temperature *T*, as is the case in nearly all NMR experiments, the Boltzmann distribution of energies dictates that the probability of finding a proton with energy ε_m *(=± ½ħω),* is given by:

$$P(E_m) = \frac{e^{-\varepsilon_m / kT}}{\sum_m e^{\varepsilon_m / kT}} \tag{1.8}$$

The divisor is a normalization factor referred to as the partition function, and is simply a sum over all possible energy states. Under normal laboratory temperatures and field strengths, equation (1.8) reveals that the probability of finding a spin in the lower (parallel) energy state is only a few parts per million higher than finding one in the higher (antiparallel) state. As a consequence, only perhaps a few protons out of every million actually contribute to the signal we detect, rendering NMR a seemingly insensitive imaging tool. However, because most NMR measurements involve samples containing Avogadro's numbers of water molecules, even a single proton per million water molecules adds up to over sixty quadrillion per single mL of water (~6.7 x 10^{16}), resulting in a significant net magnetization. For example, given an ensemble of protons, as described above, with spin density $\rho_0 = N/V$, placed within a spatially uniform magnetic field B_0 orientated along the z-axis, the net magnetization along this axis per unit volume will be determined using equation (1.8) such that:

$$\vec{M}_{0,z} = \rho_0 \sum_{m=-1/2}^{1/2} P(\varepsilon_m)\vec{\mu}_z(\varepsilon_m) \tag{1.9}$$

$$= \rho_0 \cdot \frac{m_\uparrow \hbar\gamma \cdot e^{-\varepsilon_\uparrow/kT} + m_\downarrow \hbar\gamma \cdot e^{-\varepsilon_\downarrow/kT}}{e^{-\varepsilon_\uparrow/kT} + e^{-\varepsilon_\downarrow/kT}} \hat{z} \tag{1.10}$$

where $m_\uparrow = 1/2$ and $\varepsilon_\uparrow = -1/2\,\hbar\omega$. Expanding equation (1.7) in a Taylor series and keeping only terms linear in $\hbar\omega/kT$ (since $\hbar\omega/kT$ << 1 at typical laboratory temperatures), we find that the magnitude of the magnitization vector along the z-axis is approximately:

$$M_{0,z} \cong \left(\frac{\rho_0 \gamma^2 \hbar^2}{4kT}\right) B_0 \tag{1.11}$$

The term in parentheses, which clearly depends on the laboratory conditions and spin density and species, is often denoted the magnetic susceptibility, and routinely symbolized as χ_m.

Spin Dynamics: Bloch Equations and NMR Relaxation

Although it has been shown that proton spins occupy one of two quantized spatial orientations when subjected to an external magnetic field, the transition between states is not instantaneous. Furthermore, the introduction of additional time-dependent and position-dependent magnetic fields to a system of spins produces a range of spin dynamics beyond simple energy state transitions. In the following section, the physics of spin dynamics will be addressed, beginning with the equations of motion first described by Felix Bloch in 1946 (6).

Assuming the presence of a bulk magnetization vector $\vec{M}$ due to a static $\vec{B}_0$ field, as described in equation (1.11), the generalized equation of motion for this vector will take the form:

$$\frac{d}{dt}\vec{M} = \gamma\vec{M} \times \vec{B}, \tag{1.12}$$

where $\vec{B}$ is the total external magnetic field, which includes the static field, $\vec{B}_0$, as well as any other applied fields. Assuming there is zero external field, and that $\vec{M}$ is originally parallel to $\vec{B}_0$, there will be zero force, or torque, on the net magnetization. However, if the net magnetization has any components transverse to the static field, which we again assume to be aligned along the z-axis, $\vec{B}_0 = B_0\hat{z}$, then the corresponding equations of motion (still assuming zero external field) along each laboratory axis will be:

$$\frac{dM_x(t)}{dt} = \gamma M_y(t)B_0 = \omega_0 M_y(t), \tag{1.13}$$

$$\frac{dM_y(t)}{dt} = -\gamma M_x(t)B_0 = -\omega_0 M_x(t), \tag{1.14}$$

$$\frac{dM_z(t)}{dt} = 0. \tag{1.15}$$

In this simple case, it is beneficial to combine the *x*- and *y*-components into a single transverse component such that:

$$M_+(t) = M_x(t) + iM_y(t). \tag{1.16}$$

It then follows that:

$$\frac{dM_+(t)}{dt} = \frac{dM_x(t)}{dt} + i\frac{dM_y(t)}{dt} = \omega_0\left[M_y(t) - iM_x(t)\right] \tag{1.17}$$

which has the simple solution:

$$M_+(t) = e^{-i\omega_0 t}M_+(0). \tag{1.18}$$

Therefore, in the presence of a static magnetic field $B_0\hat{z}$, any transverse components of the magnetization will precess about the static field at angular frequency ω_0.

Since the transverse component of the net magnetization, equation (1.16), describes a vector in a complex two-dimensional space, it may be useful to rewrite this equation in terms of its magnitude and phase:

$$M_+(t) = \left|M_+(t)\right|e^{i\phi(t)}, \tag{1.19}$$

where ϕ(t) represents the angle (in radians) between the magnetization vector and some arbitrarily defined axis (for example, the x-axis) corresponding to zero phase. In light of equation (1.19), as well as the fact that $\left|M_+(t)\right| = \left|M_+(0)\right|$, the solution represented in equation (1.18) may be recast as:

$$M_+(t) = \left|M_+(0)\right|e^{i\phi_0(t)}, \tag{1.20}$$

where $\phi_0(t) = -\omega_0 t + \phi_0(0)$.

While equation (1.18), or (1.20), is valid for non-interacting protons, under normal laboratory conditions additional terms must be added to the Bloch equation to account for the *relaxation* effects created by neighboring spins. In this case, the full Bloch equation is:

$$\frac{d}{dt}\vec{M} = \gamma\vec{M} \times \vec{B} - \frac{1}{T_2}\vec{M}_+ + \frac{1}{T_1}(M_0 - M_z)\hat{z}, \tag{1.21}$$

where two relaxation time constants, T_1 and T_2, have been introduced. These time constants, which are sample dependent, will be explained in more detail in the following paragraphs and represent the decay of longitudinal and transverse magnetization, respectively, due to the interaction of protons with their neighbors.

The relaxation of transverse magnetization is due to 'spin-spin' interactions, and is defined by the time constant T_2. Although the microscopic physical processes governing this effect are complex, the source of this magnetization decay is the interaction of each spin with those in its local neighborhood. As each magnetic moment precesses about the static field $\vec{B}_0$, its magnetic field interacts in a temporary and random fashion with the magnetic fields of those spins around it, slightly modifying each spin's instantaneous precession rate. As a result, there is a cumulative loss of phase coherence over time which leads to a loss in the net transverse magnetization. The rate at which this dephasing occurs is dependent upon such factors as sample composition and to a lesser extent, local magnetic field strength. As mentioned earlier, this T_2 decay leads to an additional term in the transverse components of the Bloch equation, such that:

$$\frac{d}{dt}\vec{M}_+ = \gamma\vec{M}_+ \times \vec{B} - \frac{1}{T_2}\vec{M}_+. \tag{1.22}$$

It was already shown earlier in this chapter that the first term on the righthand side of equation (1.22) leads to precession about the static magnetic field at

angular frequency ω_0. The relaxation term then is solved simply by an additional exponentially decaying function, such that:

$$M_+(t) = M_+(0)e^{-i\omega_0 t - t/T_2}. \quad (1.23)$$

In vector notation, the net magnetization (without relaxation) will precess in the transverse plane such that:

$$\vec{M}_\perp(t) = M_+(0)\left[cos(\omega_0 t + \phi_0)\hat{x} - sin(\omega_0 t + \phi_0)\hat{y}\right]. \quad (1.24)$$

Since we have experimental control over the initial phase of the net magnetization, we may, for simplicity, arbitrarily set $\phi_0 = 0$ such that the initial magnetization vector lies along the x-axis at *t = 0*. We may then combine equations (1.23) and (1.24) such that the magnitude of the magnetization *with respect to the vector* $\vec{M}_\perp(0)$ *precessing at* ω_0 decays according to T_2:

$$M_\perp(t) = M_\perp(0)e^{-t/T_2}. \quad (1.25)$$

In other words, in a reference frame rotating at the precessional frequency ω_0, the magnitude of the transverse magnetization will decay exponentially with time constant T_2. Typical values for T_2 in biological tissues are in the range of tens of milliseconds, and an example of this type of signal decay is illustrated in Figure 1.1 for three such T_2 values (25 ms, 60 ms , and 100 ms).

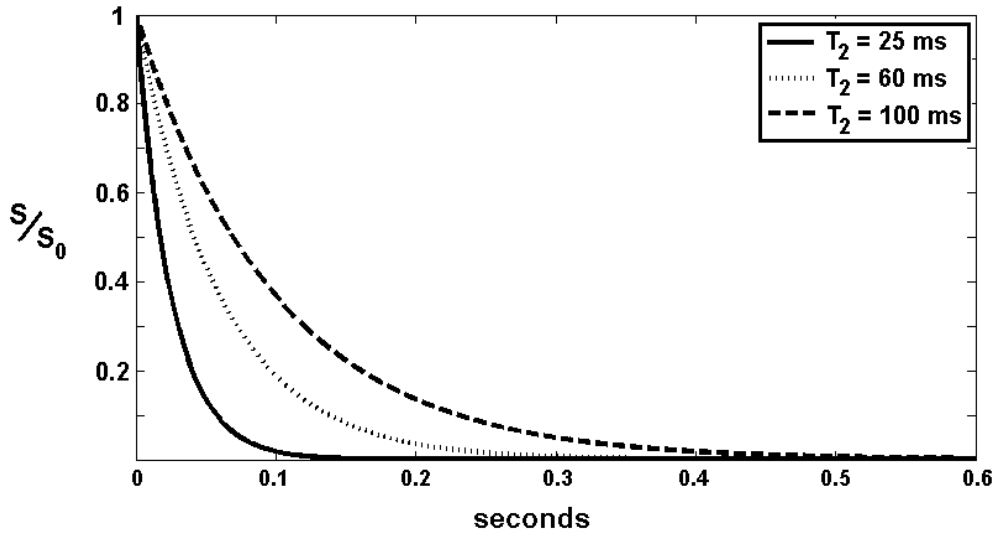

Figure 1.1. Transverse signal decay curves for three values of T_2.

As shown in equation (1.21), an additional magnetization relaxation occurs along the z-axis. This relaxation is termed 'spin-lattice' relaxation, and occurs on a time scale dictated by the physical time constant T_1. As with T_2 relaxation, this process is rather complex; however, the source of this magnetization decay is attributed to the redistribution of energy from spins with higher energy to those with lower energy. When a radiofrequency pulse of electromagnetic energy is applied to a spin ensemble, thereby exciting spins into a higher energy state, their increased vibrational and rotational energies are dissipated into the surrounding lattice, causing a slight increase in temperature followed by a gradual return to thermal equilibrium, dictated by the time constant T_1:

$$\frac{d}{dt}\vec{M} = \gamma\vec{M} \times \vec{B} + \frac{1}{T_1}\left(M_0 - M_z\right)\hat{z} \tag{1.26}$$

As shown earlier, the first term on the right-hand side of equation (1.26) describes the torque and subsequent precessional motion of the net magnetization about the static field $\vec{B}_0$ at frequency ω_0. However, in the case of a static field, this term has no effect on the z-component of the net magnetization, and may be eliminated from the discussion. The solution to this equation is therefore simply:

$$M_Z(t) = M_Z(0)e^{-t/T_1} + M_0\left(1 - e^{-t/T_1}\right). \tag{1.27}$$

Typical T_1 values in tissue are in the range of tens to thousands of milliseconds. A plot of $M_z(t)$ as a function of time, with $M_z(0) = 0,$ is illustrated in Figure 1.2, for T_1 values of 600 ms, 1000 ms, and 2000 ms.

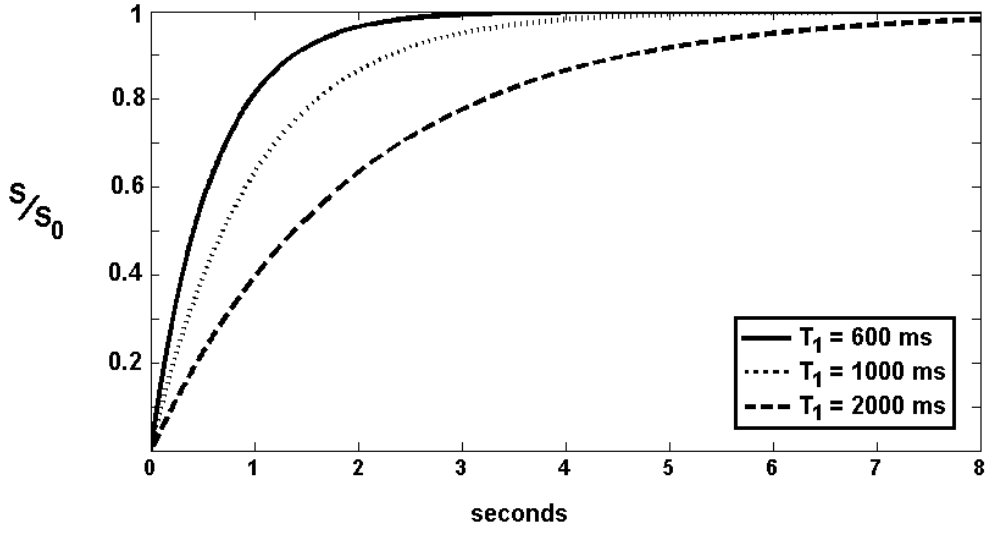

Figure 1.2. Longitudinal relaxation curves for three values of T_1.

Although the spin dynamics of precession and relaxation have been described above, the mechanism of excitation, which moves the net magnetization away from its equilibrium value along $\hat{z}$, has been ignored up to this point. Here, we introduce, in addition to the static magnetic field $B_0\hat{z}$, a time dependent magnetic field $\vec{B}_1(t)$ in the xy-plane, such that the total effective field in the laboratory reference frame is:

$$\vec{B}(t) = B_1\left[\hat{x}\cos(\omega_1 t) - \hat{y}\sin(\omega_1 t)\right] + B_0\hat{z}. \tag{1.28}$$

Ignoring relaxation effects momentarily, the components of the net magnetization along all three axes are therefore:

$$\frac{dM_x(t)}{dt} = \omega_0 M_y(t) + \gamma M_z(t) B_1 \sin(\omega_1 t), \tag{1.29}$$

$$\frac{dM_y(t)}{dt} = -\omega_0 M_x(t) + \gamma M_z(t) B_1 \cos(\omega_1 t) \tag{1.30}$$

$$\frac{dM_z(t)}{dt} = -\gamma\left[M_x(t) B_1 \sin(\omega_1 t) + M_y B_1 \cos(\omega_1 t)\right] \tag{1.31}$$

While the brief mention of a rotating reference frame was useful earlier for visualizing transverse T_2 relaxation, it is of great benefit here to provide a more formal definition of such a rotating frame. In Cartesian notation, a coordinate system rotating at angular velocity (in the negative ϕ direction):

$$\vec{\Omega} = -\omega_1\hat{z}, \tag{1.32}$$

will have coordinates:

$$\hat{x}' = \hat{x}\cos(\omega_1 t) - \hat{y}\sin(\omega_1 t) \tag{1.33}$$

$$\hat{y}' = \hat{x}\,sin(\omega_1 t) + \hat{y}\,cos(\omega_1 t). \tag{1.34}$$

Referring back to equation (1.28), we can see that the circularly polarized $\vec{B}_1(t)$ field in this rotating reference frame will simply be:

$$\vec{B}_1' = B_1 \hat{x}'. \tag{1.35}$$

In other words, in this rotating reference frame, the applied $\vec{B}_1$ field vector remains constant, along the $\hat{x}'$ axis. Therefore, if we apply a $\vec{B}_1$ field for some duration τ, along the $\hat{x}'$ axis, where τ is much less than the relaxation times T_1 and T_2, the equilibrium magnezation along the $\hat{z} = \hat{z}'$ axis will precess in the y'z'-plane at angular frequency ω_1. We may therefore apply this $\vec{B}_1$ field for some τ in order to create some angle α between the net magnetization and the $\hat{z}$ axis:

$$\alpha = \gamma B_1 \tau \tag{1.36}$$

For example, if one chooses $|B_1|$ and τ such that α = 90°, the net magnetization will precess in the y'z plane 90°, resulting in a net magnetization along the $\hat{y}'-$axis. This is illustrated more clearly in Figure 1.3, which depicts the net magnetization experiencing a 90° flip angle in both the laboratory and rotating reference frames:

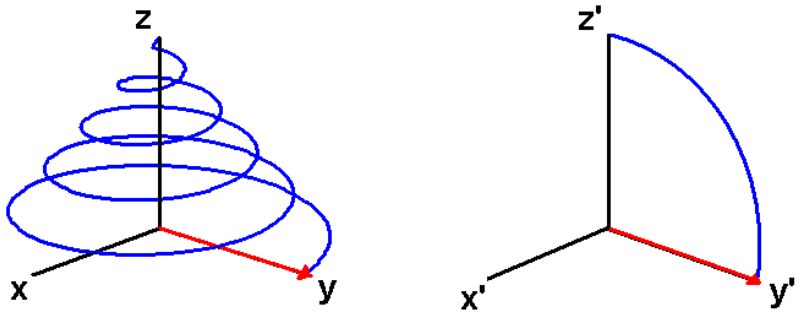

Figure 1.3. Path of the net magnetization following a 90° $\vec{B}_1$ pulse in the laboratory (left) and rotating (right) reference frame.

Typically, one may choose $\vec{B}_1(t)$ and τ in order to create a 90° flip angle, followed by a 180° degree flip angle, such as in the case of 'spin-echo' imaging, which will be discussed in the next section. However, the choice of a smaller flip angles may be more appropriate with other imaging sequences if one wishes the net magnetization to return to equilibrium much faster via T_1 processes. Furthermore, while we have assumed that the magnitude of this $\vec{B}_1(t)$ field remains constant over τ, changing only its direction with angular frequency ω_1, in reality, most $\vec{B}_1(t)$ fields used in modern imaging applications will have an amplitude that is time-dependent as well. Gaussian and sinc-shaped pulses are good examples, and will be desribed in further detail in the following section. The details of these types of pulses may be found elsewhere (13-14).

The NMR Imaging Experiment

The fundamental physics behind nuclear magnetic resonance were explored in the previous sections. Equations describing the dynamics of magnetization vectors were explored, along with the interactive processes responsible for spin excitation and relaxation. In the following section, the principles underlying NMR imaging will be addressed.

While the science of nuclear magnetic resonance had been realized and studied as early as the 1920's, it wasn't until the mid 1970's that this technology evolved into a modality capable of producing two-dimensional anatomical images. It was Paul Lauterbur, in 1973, who first suggested the idea of superimposing magnetic field gradients upon a uniform static magnetic field in order to manipulate the precessional frequency of spins based upon their position. This technique relied on a back-projection method similar to that used in computerized axial tomography (CAT) scans, and was termed "zeugmatography". Sir Peter Mansfield further developed the framework for mathematically analyzing such gradients to produce a two-dimensional picture, and in 1977, was able to produce the first *in vivo* image of human anatomy, a cross-section of a finger (15). While both of these men shared the Nobel Prize in 2003 for their accomplishments, it was Richard Ernst, in 1974, who introduced the concept of using pulsed magnetic field gradients for frequency and phase encoding, which combined with Fourier analysis, would become the most instrumental, and widely implemented, technique for acquiring NMR images (10).

The ability to spatially label a spin's position relies on the use of linear magnetic field gradients superimposed upon the static magnetic field $\vec{B}_0$:

$$\vec{B}(r,t) = \vec{B}_0 + \vec{G}(r,t)\cdot\vec{r}\,, \tag{1.37}$$

where the inclusion of a time dependence reflects the transient nature of such fields. Since we are only interested in changing the precessional frequency of the component of the net magnetization in the xy-plane, the imposed magnetic field gradient has z-component only, such that:

$$\vec{G}(r,t) = \frac{d\vec{B}_z(r,t)}{dr} = \frac{dB_z}{dx}\hat{x} + \frac{dB_z}{dy}\hat{y} + \frac{dB_z}{dz}\hat{z}\,, \tag{1.38}$$

It then follows from the Larmor relationship, equation (1.7), that the precessional frequency of a spin at position $\vec{r}$ is:

$$\omega(r,t) = \omega_0 + \gamma\vec{G}\cdot\vec{r} \tag{1.39}$$

and the accumulated phase, after time t, assuming a magnetic field gradient of constant amplitude, will be:

$$\phi(r,t) = -\int_0^t dt'\omega(r,t') = \omega_0 t + \omega_G t\,. \tag{1.40}$$

where ω_G is the precessional frequency of a spin at position $\vec{r}$, resulting from the gradient only. In other words, this precessional frequency, ω_G, is the precessional frequency that would be observed in the reference frame rotating at ω_0.

In order to illustrate how the application of magnetic field gradients may be used in producing an NMR image, let's consider a one-dimensional case.

Suppose a tube filled with pure water is placed with its long axis parallel to $B_0\hat{z}$, as illustrated in Figure 1.4.

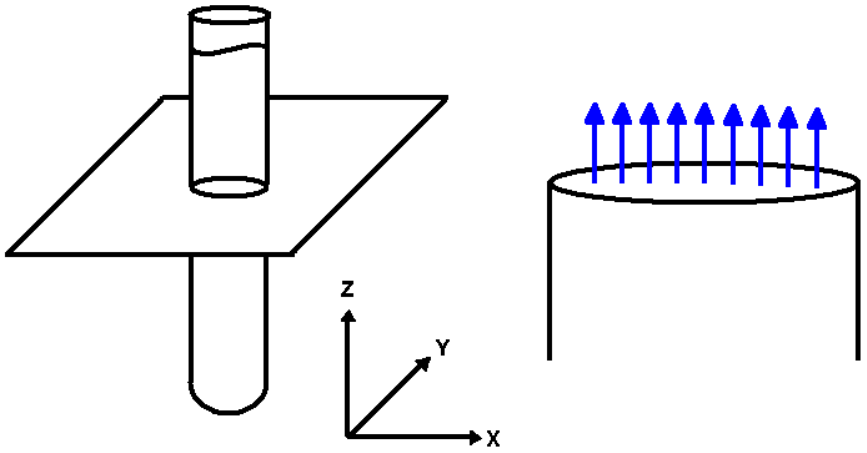

Figure 1.4. Net magnetization along the z-axis

If we then apply a 90 degree RF pulse along the x' axis as described earlier, all of the spins in the imaging slice will be rotated to align themselves along y'. In the rotating reference frame, these spins will remain aligned along y', for all times $t < t_1$, until we apply a pulsed gradient along x (in the laboratory frame) such that:

$$\omega_G(x, t_1 < t < t_1 + \tau) = \gamma x G_z(x) \tag{1.41}$$

and the accumulated phase of a spin at position x at time t is:

$$\phi'(x,t) = \gamma x G_z(x) \int_{t_1}^{t_1+t} dt' = \gamma x G_z(x) t \tag{1.42}$$

After a pulse of duration τ, the accumulated phase will thus be $\gamma x G_z(x)\tau$. Figure 1.5 shows the relative dispersion of these spins along the x-axis.

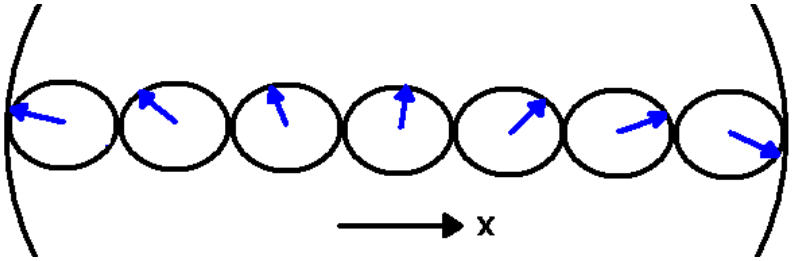

Figure 1.5. Dispersion of spin phase along the x-axis following a gradient pulse.

Those spins that experience a stronger portion of the gradient magnetic field (right hand side of the image) acquire a larger phase than those that experience a smaller field (left hand side). If we then apply a 180 degree RF pulse along x' (the spins rotate 180 degrees around x'), the phase of the spins with respect to the x-axis is reversed:

$$\phi'\left(x, t_2 < t < t_3\right) = -\gamma x G_z(x)\tau \tag{1.43}$$

If we then apply another gradient in the same direction, with equal magnitude at time t_3, the total accumulated phase will be:

$$\phi'(x,t) = -\gamma x G_z(x)\tau + \gamma x G_z(x)\int_{t_3}^{t_3+t} dt' . \tag{1.44}$$

It is clear from equation (1.44) that when the second applied gradient has been on for duration τ, the total accumulated phase at *all* positions *x* will be zero. At this moment, the spins create what is known as a "spin echo", which is detectable with a radiofrequency receiver coil tuned to the Larmor frequency.

In general, the total signal, in the one dimensional example above, will be the superposition of all spins precessing in the xy plane:

$$s(t) = \int dx \rho(x) e^{i\phi(x,t)} \ , \tag{1.45}$$

where:

$$\rho(x) \equiv \int\int dy dz \rho(\vec{r}). \tag{1.46}$$

Using equations (1.39) and (1.40), we may rewrite equation (1.45) as:

$$s(k) = \int dx \rho(x) e^{-i2\pi kx} \tag{1.47}$$

where:

$$k(t) = \frac{\gamma}{2\pi} \int_0^t dt' G(x,t'). \tag{1.48}$$

Equation (1.48) refers to an inverse space known as "*k-space*", and has units of inverse length. It is typically denoted by the variable '*k*', as it is similar to the wave-number formalism of quantum physics, representing here the spatial frequency of spin phase along the applied gradient axis.

From equation (1.47), we see that the signal *s(k)* is simply the Fourier transform of the spin density of the sample. The spin density is therefore considered to be *Fourier encoded* along the *x*-axis. Given the inverse property of Fourier transforms, we can see that the spin density is therefore the *inverse* Fourier transform of the signal:

$$\rho(x) = \int s(k) e^{+i2\pi kx} dk \tag{1.49}$$

By applying a gradient of amplitude $G_z(x,t)$, over time we are incrementing the value of *k(t)* according to equation (1.48). Thus, by sampling the signal over a

range of k-values, we may apply the Fourier analysis of equation (1.49) to obtain the spin density of the sample.

While this one dimensional example only provides insight into the projection of the spin density along one axis, the same methodology applies to collecting signals in a second dimension as well. In two dimensions, this additional spatial labelling is typically referred to as phase-encoding, as the gradient along the second dimension is incremented over the course of an experiment in order to spatially label spins with phase along this dimension. The field-of-view (FOV) in this dimension is related to the k-space increment such that

$$FOV = \frac{1}{\Delta k_{PE}} \tag{1.50}$$

with:

$$\Delta k_{PE} = \gamma G_{PE} t_{PE} \tag{1.51}$$

where G_{PE} and t_{PE} are the strength and duration of the phase-encoding gradient blip. The signal is then a two-dimensional extension of equation (1.47):

$$s\left(k_x, k_y\right) = \int dx dy \rho\left(x, y\right) e^{-i2\pi\left(k_x x + k_y y\right)} \tag{1.52}$$

This phase-encoding may be applied along the third laboratory dimension as well in order to produce three-dimensional volume images.

In addition to frequency- and phase-encoding, linear magnetic field gradients are also used to select specific imaging slices within a sample. Since the application of a linear magnetic field gradient produces a range of precessional frequencies, and these frequencies are spatially dependent, a bandwidth selective radiofrequency pulse may be used to select the range of

frequencies corresponding to a particular slice. For example, if a linear magnetic field gradient is placed along the z-axis, then the frequency of a spin at position *z* will be:

$$f(z) = f_0 + \frac{\gamma}{2\pi} G_z z \tag{1.53}$$

where $f_0 = \frac{\gamma}{2\pi} B_0$ is the Larmor precessional frequency at *z = 0*. If we wish to excite only a finite slice of thickness Δz, extending from $z_0 - \frac{\Delta z}{2}$ to $z_0 + \frac{\Delta z}{2}$, then the range of frequencies must extend from $\left(\gamma G_z z_0 - \gamma G_z \frac{\Delta z}{2}\right)$ to $\left(\gamma G_z z_0 + \gamma G_z \frac{\Delta z}{2}\right)$. Therefore, the total width of the frequency range is:

$$\Delta f = \left(\gamma G_z z_0 + \gamma G_z \frac{\Delta z}{2}\right) - \left(\gamma G_z z_0 - \gamma G_z \frac{\Delta z}{2}\right), \tag{1.54}$$

which simplifies to:

$$\Delta f = \gamma G_z \Delta z \tag{1.55}.$$

This relationship, equation (1.55), is defined as the *bandwidth* of the slice-selective radiofrequency pulse, $\Delta f \equiv BW_{RF}$.

By implementing a gradient of amplitude G_z, and an appropriate radiofrequency pulse $\vec{B}_1(t)$ of bandwidth BW_{RF}, we may therefore excite a range of frequencies Δf in order to exite the slice Δz. Since we typically wish to excite a 'flat' slice with well defined edges, it is intuitive to use a boxcar function of the

form $rect(f/\Delta f)$, which has a Fourier inverse in the time domain proportional to a sinc function:

$$B_1(t) \propto sinc(\pi \Delta f\, t). \tag{1.56}$$

This means that, in the time domain, the RF excitation has an amplitude modulated by a sinc envelope. An illustrative example is shown in Figure 1.6, along with its Fourier inverse in the frequency domain, corresponding to a slice of thickness Δz.

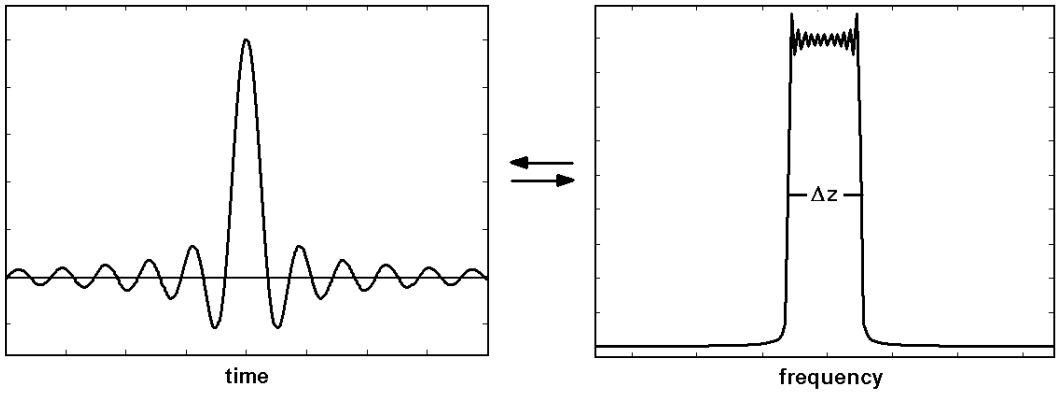

Figure 1.6. Time-frequency relationship of slice selective sinc RF pulse

While the above example demonstrates the selection of a slice orthogonal to the z-axis, one may similarly apply the same logic to slices orthogonal to the x- or y-axis as well. It is the choice of this gradient orientation that determines whether the imaging slice is considered to be coronal, sagittal, or axial.

Finally, it must be noted that, while a magnetic field gradient applied along $\hat{z}$ allows for excitation of spins within a slice Δz, this same gradient also induces a dephasing of spins along $\hat{z}$ due to the spatially varying precessional

frequencies they experience between their initial excitation and the end of the gradient pulse. However, this dephasing may be recovered by the addition of another gradient. To a first approximation, if we assume that the magnetization is excited instantaneously at time *t* = *0*, in the exact center of the slice select gradient $G_z(z,t=0)$, then the spins will experience a phase along $\hat{z}$ of:

$$\phi(z,t) = -\gamma G_z z t . \tag{1.57}$$

Since the total signal (assuming a constant spin density, ρ_0) is proprtional to $e^{-i\phi(z,t)}$, thicker slices and/or higher gradient amplitudes will result in more signal decay due to increased dephasing along $\hat{z}$. However, in this simple approximation of instantaneous excitation, the spins only experience dephasing during the second half of the gradient pulse, and therefore, may be refocused with a gradient whose area equals the area of this slice select gradient after *t* = *0*.

References

1. Gerlach W., Stern O. Das magnetische Moment des Silberatoms. Zeitschrift für Physik 1922;9:353–5.

2. Uhlenbeck GE, Goudsmit S. Spinning electrons and the structure of spectra. Nature 1926;117:264-5.

3. Frisch, Stern. Magnetic deviation of hydrogen molecules and the magnetic moment of the proton. I. Z. Phys 1933;85:4

4. Rabi, II. Space quantization in a gyrating magnetic field. Phys. Rev. 1937;51:652-4.

5. Purcell EM, Torrey HC, Pound RV. Resonance absorption by nuclear magnetic moments in a solid. Phys Rev. 1946;69:37.

6. Bloch F. Nuclear induction. Phys Rev. 1946;70:460-74.

7. Hahn EL. Spin Echoes. Phys Rev. 1950;80:580-94.

8. Lauterbur PC. Image formation by induced local interactions: examples employing nuclear magnetic resonance. Nature 1973;242:190-91.

9. Damadian, RV. Tumor detection by nuclear magnetic resonance. Science 1971;171:1151-53.

10. Kumar A, Welti D, Ernst RR. NMR Fourier Zeugmatography. J Magn Reson 1975;18:69-83.

11. Mansfield P, Grannell PK. NMR “diffraction” in solids? J Phys C: Solid State Phys 1973;6:422-26.

12. Mansfield P. Mulit-planar imaging using NMR spin echoes. J Phys C: Solid State Phys 1977;10:55-58.

13. Bernstein MA, King KF, Zhou XJ. Handbook of MRI Pulse Sequences. Academic Press 2004 (book).

14. Haacke EM, Brown RW, Thompson MR. Magnetic Resonance Imaging: Physical Principles and Sequence Design. Wiley-Liss 1999 (book).

15. Mansfield P, Maudsley AA. Medical imaging by NMR. Br J Radiol 1977;50:188-94.

CHAPTER II

PHYSICAL PRINCIPLES OF DIFFUSION MRI

In the following pages, the concepts of diffusion MRI will be reviewed. The basic physical principles of molecular diffusion will be discussed, along with the effect that biological structures have on this process. The methodology for quantifying the rate of water diffusion with MRI will be explained, along with the information that may be gleaned from such experiments. The current directions of the research field will be described, along with current problems and limitations. Finally, this review will conclude with a brief outline of the particular applications of diffusion-weighted MRI contained in this thesis.

Overview of Diffusion MRI Research

Besides paving the way for the spin-echo imaging experiment that would later become a staple of modern NMR imaging and research, the seminal paper describing “Spin Echoes” by Erwin Hahn first described the effects that self-diffusing spins would have on the NMR signal. Because the NMR signal produced by a spin echo requires that precessing spins experience the same B_0-field during all RF pulses, Hahn noted, the thermal agitation and subsequent self-diffusion of spin-bearing molecules through inhomogenous regions of the field would produce a variance in the phase of the motile spins, resulting in an attenuation of the measured signal. The effects of this self-diffusion on the

measured signal would soon become a topic of concern among researchers, and so diffusion NMR was born. In the years to follow, researchers sought to quantify this molecular self-diffusion, through both theory and experiment. In 1954, Herman Carr and Edward Purcell published an article outlining the first NMR method for quantifying the rate of molecular self-diffusion through the use of a static magnetic field gradient (1). Two years later, H.C. Torrey amended the standard Bloch equations, describing the time dependence of precessing magnetic moments, by adding terms dependent upon the flux of diffusing magnetic moments, thus establishing the oft-cited Bloch-Torrey equations (2). Perhaps one of the most significant experimental leaps occurred in 1965, when Stejskal and Tanner developed the theory and methodology of the pulsed-gradient spin-echo (PGSE) experiment (3). This technique allowed researchers to quantify a discrete 'diffusion time' over which molecular diffusion was measured, thereby allowing for calculation of the spatial scale of moleculer displacement. They also outlined the Fourier relationship between the NMR signal attenuation and the diffusion displacement probability, a theory that would lead the development of "q-space" MRI. Tanner, in 1978, was also first to coin the term "apparent diffusion coefficent" (ADC) to reflect the effects that complex media, such as biological tissues, would have on the effective diffusion rate (4).

Since these seminal works, a number of other theoretical and experimental frameworks have been developed for the quantization of molecular diffusion in biological samples. For example, the realization of diffusion anisotropy, or the directional dependence of the diffusion rate, has led to the

implementation of diffusion tensor imaging (DTI), and more recently, high angular resolution diffusion imaging (HARDI) in an attempt to map neural fiber pathways in brain white matter (5-8). Paul Callaghan has developed an elegant theoretical framework for describing restricted diffusion based upon so-called q-space diffusion-diffraction (9-10). Others, such as Woessner (11), Cory (12), Mitra (13), and Latour (14) have developed theories and methods for describing diffusion in compartmentalized geometries, biological cells in particular, extracting such relevant parameters as pore surface-to-volume ratio, extracellular tortuosity, and membrane permeability. Finally, work by Stepisnik (15-16), as well as by Parsons, et al (17), Does, et al (18), Schachter, et al (19), and Colvin, et al (20), has focused on methods for drastically decreasing the effective diffusion time of DW-MRI measurements, thereby probing biological structures nearly an order of magnitude smaller than those described in nearly all previous studies.

The Physics of Molecular Diffusion

In 1855, Adolf Fick derived an equation describing the steady-state, non-equilibrium diffusive flux, ***J***, of molecules across a molecular concentration gradient, ∇C (21):

$$\vec{J} = -D\nabla C \tag{2.1}$$

Known as *Fick's first law*, this relationship simply states that molecules will migrate at a diffusion rate *D* towards regions of lower molecular concentration. Combining this with the continuity equation (conservation of mass):

$$\frac{\partial C}{\partial t} = -\nabla \cdot J \tag{2.2}$$

we get *Fick's second law*, often termed the *law of diffusion*:

$$\frac{\partial C}{\partial t} = \nabla \cdot D\nabla C \tag{2.3}.$$

In the most simple case of isotropic diffusion, this reduces to:

$$\frac{\partial C}{\partial t} = D\nabla^2 C\,, \tag{2.4}$$

whose solution, in three dimensions, with initial condition $C(r,0) = \delta(r)$, is a Gaussian function centered at $r = 0$:

$$C(\vec{r},t) = \frac{1}{(4\pi Dt)^{3/2}} exp\left(\frac{-\vec{r}\cdot\vec{r}}{4Dt}\right). \tag{2.5}$$

Following upon this work, Albert Einstein developed a kinetic theory of diffusion in 1905 based upon the physical properties of the diffusing molecules, concluding that the mean squared displacement of a molecule diffusing at rate D over time t is:

$$\left\langle r^2 \right\rangle = 2nDt \tag{2.6}$$

where n is the dimensionality of the system (22). Known simply as the Einstein relation, it shows that the diffusion coefficient is proportional to the variance of the Gaussian diffusion model, i.e. $\sigma^2 = 2Dt$. This relationship, as will be shown below, will prove highly beneficial for relating the measured diffusivity of water molecules within a biological sample to the spatial dimensions of their local cellular environment.

In order to understand how an NMR experiment may be used to quantify the rate of water diffusion within a medium, we examine the effect a single diffusing spin has on the NMR signal, using the simple bipolar pulsed gradient technique developed by Stejskal and Tanner (3). Let us consider a single magnetic moment, or spin, with gyromagnetic ratio γ, precessing in the transverse (*xy*) plane about the static, uniform magnetic field B_0. If the spin's position is labeled by imposing a magnetic field gradient $G_x = dB_z/dx$, for a time δ, the acquired phase, ϕ, of that spin will be:

$$\phi_1 = \gamma \int_0^{\delta} G_x x_1 dt = \gamma G_x x_1 \delta \tag{2.7}$$

where x_1 is the spatial coordinate of the spin along the gradient direction. (Note that we can arbitrarily set $\phi(0) = 0$ without loss of generality.) Following this spin labeling, a radiofrequency pulse, tuned to the Larmor frequency of the precessing spin, reverses the spin phase, resulting in $-\phi_1$. At a later time, $t = \Delta$, another δ-pulse of equal magnitude is applied, imparting a phase shift:

$$\phi_2 = \gamma \int_{\Delta}^{\Delta+\delta} G_x x_2 dt = \gamma G_x x_2 \delta \tag{2.8}$$

where x_2 is the spin's position along the x-axis during the second pulse. If we assume that δ is sufficiently short as to not allow spin displacement during application of the gradient pulses, the net phase accumulation from both pulses will be:

$$\delta(\phi) = -\phi_1 + \phi_2 = \gamma G_x \delta(x_2 - x_1). \tag{2.9}$$

Clearly, if $x_1 = x_2$, the spin has no effective displacement, and the net phase is zero. However, if $x_1 \neq x_2$, the result is a net dephasing, or loss of phase coherence, with respect to those spins that are static. Extending this concept to an ensemble of *N* spins, the total transverse NMR signal will simply be the vector sum of all *N* resonant magnetic moments, and may be written:

$$M = M_0 \sum_{j=1}^{N} exp(i\delta(\phi_j)) \tag{2.10}$$

where M_0 is the initial transverse magnetization at $t = 0$.

Since we do not have knowledge of all *N* individual spin displacements and their corresponding phase shifts, we must take a statistical approach for evaluating this sum. If $P(x_2|x_1, \Delta)$ is the conditional probability of a spin, initially at position x_1, being found at position $x_2 + dx_2$ after a time Δ, then the attenuation equation (2.10) may be cast in the form:

$$\frac{M}{M_0} = \int_{-\infty}^{\infty}\int_{-\infty}^{\infty} P(x_2 \mid x_1, \Delta)\, exp(i\gamma G_x \delta(x_2 - x_1))dx_1 dx_2. \tag{2.11}$$

If we assume a Gaussian solution to the Fickian diffusion equation described earlier, the one-dimensional conditional probability density takes the form:

$$P(x_2 \mid x_1, \Delta) = \frac{1}{(4\pi D t)^{1/2}} exp\left(\frac{-(x_2 - x_1)^2}{4Dt}\right) \tag{2.12}$$

and, inserting (2.12) into (2.11), we get:

$$\frac{M}{M_0} = exp\left(-(\gamma G_x \delta)^2 D\Delta\right). \tag{2.13}$$

Therefore, using this approach, we may determine the diffusion coefficient by measuring the NMR signal attenuation at several values of Δ or G (while typically keeping δ fixed). However, it must be noted that this simplified description is confounded by several problems in practice. First, given hardware limitations and/or choice of experimental parameters, δ may not always be considered negligible compared to Δ. In this case, diffusion during the δ-pulses will obscure the precise location, and thus phase, of the spin's initial and final positions, resulting in an unclear determination of its net phase loss. Second, the application of additional gradient pulses for the purpose of imaging may alter the spin's phase structure as well, causing additional attenuating effects on the magnetization. Therefore, we must develop a more robust framework for characterizing the phase loss due to diffusion, applicable to any generalized sequence of magnetic field pulses.

Published in 1956, Torrey's modification of the Bloch equations, subsequently known as the Bloch-Torrey equations, describe both the rotational and translational dynamics of a spin precessing within an applied magnetic field, along with the relaxation effects occurring as a result of interaction with its environment (2). In the absence of magnetic field gradients, a simple time dependent solution to these equations may be found in terms of the Larmor precession frequency and relaxation decay constants. However, in the presence of an applied magnetic field, the evolution of the magnetization vector will depend upon both its position within the gradient field, as well as by the random thermal

motion of any diffusing spins as described by *Fick's second law,* equation (2.13), resulting in:

$$\frac{\partial \Psi(r,t)}{\partial t} = -i\gamma \vec{r} \cdot \vec{G}(t)\Psi + \nabla \cdot \vec{\vec{D}} \nabla \Psi \tag{2.14}$$

where Ψ is the magnetization vector at time *t*. Assuming a solution of the form:

$$\psi(r,t) = M(t)\, exp\left(-i\vec{r} \cdot \vec{k}(t)\right) \tag{2.15}$$

where *M(t)* represents the attenuation due to diffusion, and

$$\vec{k}(t) = \gamma \int_0^t \vec{G}(t)dt', \tag{2.16}$$

then (2.15) may be substituted into (2.14), resulting in

$$\frac{dM(t)}{dt} = -M(t)\vec{k}(t)^T \vec{\vec{D}}\vec{k}(t). \tag{2.17}$$

The solution to (2.17) is then

$$M(t) = M_0\, exp\left(-\int_0^t k(t')^T \cdot \vec{\vec{D}} \cdot k(t')dt' \right) \tag{2.18}$$

where, in the case of anisotropic diffusion, $\vec{\vec{D}}$ is a symmetric, positive-definite, rank two tensor. For simplicity, equation (2.18) is often written as:

$$\frac{M}{M_0} = exp\left(-\sum_{i=1}^{3}\sum_{j=1}^{3} b_{ij} D_{ij} \right) \tag{2.19}$$

where

$$b_{ij} = \int_0^t \vec{k}(t') \cdot \vec{k}(t')dt' \tag{2.20}$$

is termed the "*b-value*" and represents the diffusion weighting imparted upon the spin ensemble by both the imaging and diffusion sensitizing gradients. Integrating equation (2.20) for the sequence of bipolar pulsed gradients described earlier, we arrive at:

$$b = \gamma^2 \delta^2 G_D^2 \left(\Delta - \frac{\delta}{3} \right) \tag{2.21}$$

where G_D is the amplitude of the motion sensitizing diffusion gradient. This expression differs from that obtained in equation (2.13) by the subtraction of $\frac{\delta}{3}$ from Δ, thereby accounting for the finite width of the gradient pulses used to label the spin's position.

Advanced Diffusion MRI Methods

While a full mathematical description of the diffusion tensor, mentioned above, is too lengthy for this review, it will suffice to note that this type of analysis is well-suited for measuring diffusion in systems with anisotropic structure, such as myelinated white matter nerve bundles, or striated heart and skeletal muscle. In these cases, the diffusion sensitizing gradients are placed along six non-collinear axes in a series of six images, and the elements of the tensor for each voxel are calculated via equations (2.19) and (2.20). The resulting tensor may then be rotated into an eigenbasis, diagonalizing the tensor and establishing the principle axes of diffusion. The diffusion in each voxel is then modeled as an ellipsoid, with the principle axes corresponding to the eigenvalues and eigenvectors of the rotated tensor. Consequently, this ellipsoid represents the

three-dimensional Gaussian probability distribution of diffusion displacements within each voxel, with the major eigenvector corresponding to the primary alignment of fibers within that voxel.

While the assumption of Gaussian diffusion used in experimental analysis is sufficient for describing a wide variety of diffusion processes, it does not accurately predict the displacement of spins diffusing within a restricted environment. In particular, in biological cells where cellular and nuclear membranes and intracellular organelles hinder the mobility of diffusing water molecules, molecular diffusion within biological tissues may not be assumed to be Gaussian, as restrictive barriers to motion render the Gaussian displacement probability inaccurate. Nevertheless, the majority of NMR diffusion studies frequently evaluate the diffusion coefficient using this methodology, typically replacing D with an apparent diffusion coefficient, or ADC. The ADC, which is a macroscopic measurement of water mobility, will thus differ from the true diffusion coefficient D_0 in a manner that depends on the effects of local restrictive barriers to diffusion. Consequently, by examining the variation in ADC over a range of diffusion times, one can obtain information about the range of spatial displacements in the local cellular environment via the Einstein relation, equation (2.6).

Alternative methods: q-space and q-balls

Considering that the assumption of Gaussian diffusion may break down in the presence of restrictive barriers, many researchers attempt to address the

problem by noting the Fourier relationship between the probability density and the signal attenuation, equation (2.11). Instead of assuming an explicit form for the probability density, one may invert the problem, obtaining information about the probability of spin displacement, at fixed diffusion time Δ, by Fourier transforming the signal attenuation with respect to the spatial frequency vector, $\gamma\vec{G}_D\delta$. This may be written succinctly as:

$$P(R,\Delta) = \int_{-\infty}^{\infty} exp(i2\pi\vec{q}\cdot\vec{R})\frac{M(q,\Delta)}{M_0}, \tag{2.22}$$

where

$$\vec{q} = (2\pi)^{-1}\gamma\vec{G}\delta \tag{2.23}$$

is the reciprocal variable to displacement $\vec{R}$, and $P(\vec{R},\Delta)$ is typically referred to as the diffusion propagator. While this model circumvents the assumption of Gaussian diffusion, and has been shown by several groups (9-10, 23) to be an appropriate description for a variety of geometries, this type of analysis has its limitations as well. First, this approach assumes that the phase labeling δ-pulses are negligible with respect to the diffusion time, Δ, between them. While this assumption may hold true in the limit of large diffusion times, the relevant scale of diffusion displacement in biological tissues is very small, on the order of microns or less. Consequently, in order to measure these microscopic displacements, increasingly large values of $\vec{q}$ must be used. However, since $\vec{q}$ is the product of gradient amplitude and duration, this may be limited by the maximum gradient amplitude available, or by the narrow δ-pulse requirement at

short diffusion times. Nevertheless, this type of analysis still provides important information pertaining to biological systems without assuming Gaussian diffusion. One particularly useful application of this methodology is in the case of anisotropic diffusion mentioned earlier. In white matter, where bundled, myelinated nerve cells channel the diffusion preferentially along their primary axis, one can map the directionality of such structures within each voxel (volume pixel) by evaluating the directional dependence of diffusion displacement within that voxel. While the diffusion tensor model was the first logical approach to such a task, it was immediately realized that given the microscopic dimensions of nerve cells, a single imaging voxel may contain a population of nerves with very different directional properties. More specifically, nerves may cross, branch, or curve, all within one voxel, a problem known as partial volume averaging. Therefore, the diffusion tensor and associated ellipsoid may be insufficient for describing such complicated geometries.

However, by employing the q-space methodology described above, over a large number of gradient directions, it is possible to obtain a three-dimensional displacement probability that is independent of any underlying model for the diffusion process. In doing so, voxels with diffusion along multiples axes will exhibit diffusion signals with multiple maxima and minima corresponding to a heterogeneity of underlying fiber orientations. One approach to this, called q-ball imaging, measures the signal at multiple values of $\vec{q}$ evenly spaced on the surface of a sphere in q-space. While the details of the subsequent analysis will not be described here, the significance of this approach is that an orientation

distribution function (ODF) is obtained. While the ODF differs from the probability distribution function (PDF) in that it does not provide specific information regarding the magnitude of spatial displacements, it nevertheless reveals important information regarding the underlying morphology of the tissue within each voxel by resolving fibers with a range of angular distributions. This technique is particularly beneficial for resolving voxels with crossing or splaying fibers.

A similar approach, called diffusion spectrum imaging (DSI), measures the signal at multiple values of $\vec{q}$ spaced evenly upon a three-dimensional Cartesian grid, thereby providing additional information about the magnitude of displacement in addition to the angular dependence. While this latter technique provides some indication of the size of the restrictive compartments as well, it suffers from the same limitations described above at short diffusion times and is thus incapable of evaluating decreasingly smaller microscopic displacements via the propagator formalism. In addition, given the large number of q-values needed to resolve such distributions, these imaging modalities are generally very time intensive as well.

References

1. Carr HY, Purcell EM. Effects of diffusion on free precession in nuclear magnetic resonance experiments. Phys Rev 1954;94:630-8.

2. Torrey HC. Bloch equations with diffusion terms. Phys Rev 1956;104: 563–65.

3. Stejskal EO, Tanner JE. Spin diffusion measurements: spin echoes in the presence of a time-dependent field gradient. J Chem Phys 1965;42:288-92.

4. Tanner JE. Transient diffusion in system partitioned by permeable barriers. Application to NMR measurements with a pulsed field gradient. J Chemi Phys 1978;69(4):1748-54.

5. Basser PJ, Mattielo J, Le Bihan D. Estimation of the effective self-diffusion tensor from NMR spin echo. J Magn Reson 1993;104:247-54.

6. Le Bihan D, Mangin JF, Poupon C, et al. Diffusion tensor imaging: concepts and applications. J Magn Reson Imag 2001;13:534-46.

7. Tuch DS, Reese TG, Wiegell MR, Makris N, Belliveua J, Wedeen VJ. High angular resolution diffusion imaging reveals intravoxel white matter heterogeneity. Magn Reson Med 2002;48:577-82.

8. Tuch DS. Q-ball imaging. Magn Reson Med 2004;52:1358-72.

9. Callaghan PT, Macgowan D, Packer KJ, Zelaya FO. High resolution q-space imaging in porous structures. J Magn Reson 1990;90:177–82.

10. Callaghan PT. NMR imaging, NMR diffraction, and applications of pulsed gradient spin echoes in porous media. Magn Res Imag 1996;14:701-09.

11. Woesnner DE. NMR spin-echo self-diffusion measurements on fluids undergoing restricted diffusion. J Phys Chem 1963;67:1365-67.

12. Cory DG, Garroway AN. Measurement of translational displacement probabilities by NMR: an indicator of compartmentation. Magn Reson Med 1990;14(3):435-444.

13. Mitra PP, Sen PN, Schwartz LM. Short-time behavior of the diffusion-coefficient as a geometrical probe of porous media. Phys Rev B 1993; 47(14): 8565-74.

14. Latour LL, Svoboda K, Mitra PP, Sotak CH. Time dependent diffusion of water in a biological model system. Proc Natl Acad Sci USA. 1994;91**:**1229–33.

15. Stepisnik, J. Analysis of NMR self-diffusion measurements by density matrix calculation. Physica 1982;104B:350-61.

16. Stepisnik J, Callaghan PT. Low-frequency velocity correlation spectrum of fluid in a porous media by modulated gradient spin echo. Magn Reson Imag 2001;19(3-4):469 –72.

17. Parsons EC, Does MD, Gore JC. Modified oscillating gradient pulses for direct sampling of the diffusion spectrum suitable for imaging sequences. Magn Reson Imag. 2003; 21: 279-285.

18. Does MD, Parsons EC, Gore JC. Oscillating gradient measurements of water diffusion normal and globally ischemic rat brain. Magn Reson Med 2003;49:206-15.

19. Schachter M, Does MD, Anderson AW, Gore JC. Measurements of restricted diffusion using an oscillating gradient spin echo sequence. J Magn Reson 2000;147:232-37.

20. Colvin DC, Yankeelov TE, Does MD, Yue Z, Quarles C, Gore JC. New insights into tumor microstructure using temporal diffusion spectroscopy. Cancer Res 2008 July;68:5941-5947.

21. Fick A. Uber diffusion. Annalen der Physik 1855;94:59.

22. Einstein A. On the movement of small particles suspended in stationary liquids required by the molecular-kinetic theory of heat. Annalen der Physik 1905;17:549-60.

23. Assaf Y, Mayk A, Cohen Y. Displacement imaging of spinal cord using q-space diffusion weighted MRI. Magn Res Med 2000;44:713-22.

CHAPTER III

OSCILLATING GRADIENT DIFFUSION MRI METHODS

Introduction to OGSE Techniques

It was mentioned earlier that the presence of restrictive structures in biological tissues gives rise to a time dependence of the diffusion coefficient. Therefore, by varying the diffusion time in an NMR experiment, variations in the spatial scale of molecular displacements may be gauged by variations in the ADC. In general, the shorter the diffusion time, the higher the ADC, as less restrictions are encountered, and vice versa. However, as an alternative to measuring the effects of diffusion time on ADC, the correlation between a molecule's velocity at two different time points may be used to quantify the spatial scale of restrictive barriers in the intracellular environment. While the memory of a spin's velocity in unrestricted media is erased on the order of picoseconds due to intermolecular thermal collisions, the presence of restrictive barriers provides a correlation that may persist over a timescale amenable to NMR measurement, and may be measured by appropriate choice of spin phase modulation.

It is has been shown that the diffusion tensor is related to the molecular velocity autocorrelation function, $\langle v(t)v(0)\rangle$, by a Fourier transform (1):

$$D_{i,j}(\omega) = \frac{1}{2}\int_0^{\infty} \langle v_i(t')v_j(0)\rangle e^{-i\omega t'} dt' . \qquad (3.1)$$

As mentioned, freely diffusing water molecules have effectively zero correlation on the timescales accessible to measurement, while coherently flowing molecules have a positive correlation, and restricted molecules reflecting off of cellular boundaries will have a persistent negative correlation that is dependent upon the spacing of the restrictions. See Figure 3.1.

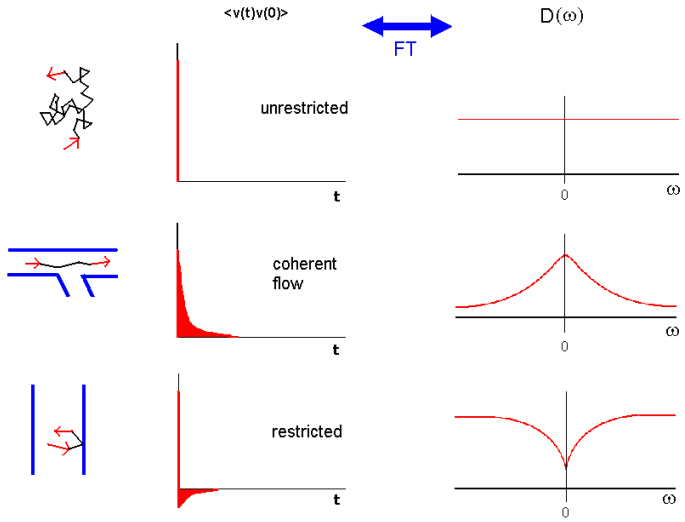

Figure 3.1. Relationship between the velocity autocorrelation function and the diffusion spectrum.

As a result, $D(\omega)$ will reflect the degree of restriction at long t (low ω), and will approach the tissue's intrinsic D_0 at short t (high ω). Therefore, by measuring the spectral density of $D(\omega)$ over a broad range of frequencies, one may be able to obtain information about the range of restrictions within biological tissues.

Utilizing a density matrix formalism that will not be outlined here, Stepisnik (1) found that the diffusion attenuated signal from an NMR experiment may be written in terms of the product of the spectral density *D(ω)* of the spin velocity auto-correlation and the dephasing due to the gradient pulses *F(ω):*

$$S = S_0 \exp\left(-\beta(t)\right) = S_0 \exp\left(-\frac{1}{\pi}\int_0^\infty \vec{F}(\omega)\vec{D}(\omega)\vec{F}(\omega)d\omega\right) \qquad (3.2)$$

where $\beta(t)$ is the attenuation factor, and

$$\vec{F}(\omega) = \int_0^\infty dt \exp(i\omega t)\vec{F}(t) = \int_0^\infty dt \exp(i\omega t)\int_0^t dt' \gamma\vec{G}(t'). \qquad (3.3)$$

Note that $\vec{F}(t) = \vec{k}(t)$, which is just the time-dependent gradient induced spin modulation described earlier. Succinctly, equation (3.3) shows that $\vec{F}(\omega)$ is the spectral density (Fourier transform) of the time-dependent gradient waveform. As a result, we may isolate and probe specific frequencies of the diffusion spectrum with appropriate choice of phase modulation. While Callaghan and Stepisnik (2-4) have used sequences of RF pulses interspersed with gradient pulses to achieve such an effect, the method employed throughout the remainder of this thesis makes use of a sinusoidally varying gradient of frequency ω_m (where the subscript *m* denotes the modulation frequency). Figure 3.2 outlines two of the possible gradient waveforms that may be used, namely the cosine (C) and sine (S) modulated waveforms, along with the conventionally implemented bipolar

pulsed gradients. The corresponding Fourier transforms, or spectral densities, are also shown.

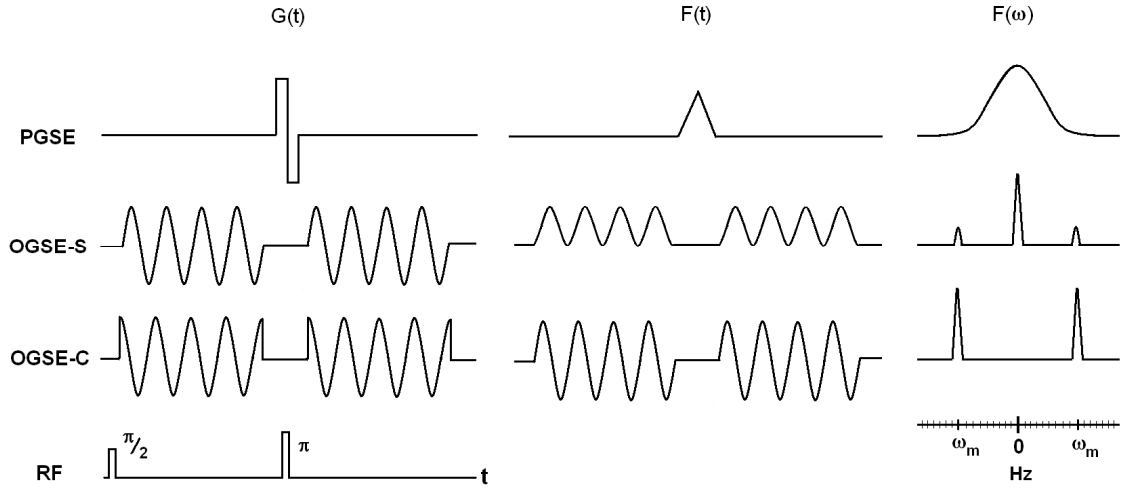

Figure 3.2. Examples of gradient waveforms and their corresponding spectral densities.

The sine-modulated gradient waveform has, in the case of infinite pulse duration, a spectral density of dephasing:

$$F(\omega) \propto \Im\left[\int_0^t sin(\omega_m t')dt'\right] \propto$$
$$\Im[1 - cos(\omega_m t)] \propto \delta(\omega) + \sqrt{\frac{1}{2}}\delta(\omega \pm \omega_m). \quad (3.4)$$

The cosine-modulated waveform has spectral density:

$$F(\omega) \propto \Im\left[\int_0^t cos(\omega_m t')dt'\right] \propto$$
$$\Im[sin(\omega_m t)] \propto \sqrt{\frac{1}{2}}\delta(\omega \pm \omega_m). \quad (3.5)$$

As is clear from Figure 3.2, the bipolar pulsed gradients do not sample the frequency spectrum discretely, and are therefore inappropriate for this type of

analysis. However, both the cosine- and sine-modulated waveforms do provide the discrete sampling of $\vec{F}(\omega)$ necessary to extract $\vec{D}(\omega)$. Furthermore, while the sine-modulated waveform samples the spectrum at ± ω_m, it is clear from equation (3.4), as well as Figure 3.2, that there is a significant zero frequency component associated with this waveform. The cosine modulated waveform, on the other hand, does not contain this component and is therefore a more appropriate choice for our studies. Because of nonzero gradient rise times, however, the initial rise to maximum amplitude confounds the issue, requiring slight modification of the modulation. In this case, the first lobe of the cosine waveform is replaced with a sine waveform of twice the base frequency. Although this modifies the corresponding diffusion weighting, the result is still tractable and serves only to widen the peaks slightly, though insignificantly (5).

Similar to the pulsed-gradient spin-echo method, the amount of diffusion-weighting, or b-value, is calculated via equation (2.20). For the sine-modulated waveform this results in:

$$b_{sine} = \frac{3}{8}\left(\frac{\gamma G_D}{\pi N}\right)^2 T^3 \ , \tag{3.6}$$

where *N* is the number of oscillations implemented per waveform duration, *T*. For the apodized cosine-modulated waveform described above, this integrates to:

$$b_{cos} = \frac{1}{8}\left(\frac{\gamma G_D}{\pi N}\right)^2 T^3 \left(1 - \frac{1}{8N}\right). \tag{3.7}$$

Using these techniques, specific frequencies of the diffusion spectrum may be sampled by utilizing gradients of the appropriate modulation frequency ω_m within a spin-echo imaging sequence. Such methods are therefore termed 'diffusion spectroscopy', or sometimes 'temporal diffusion spectroscopy', to indicate the use of *time-dependent* gradient waveforms for sampling discrete *frequencies* of the diffusion spectrum. While the term 'diffusion spectroscopy' has been employed by other groups implementing q-space diffraction methods (6-7), such studies would be more appropriately labelled as 'displacement spectroscopy', as these methods make use of the Fourier relationship between the *spatial-dependence* of the gradient waveforms and the *displacement* probability function (as briefly described in Chapter II).

Since the phase modulation of spins, using temporal diffusion spectroscopy, occurs on the order of an oscillation period, the resulting effective diffusion time is on this order as well. Using currently available hardware in the Center for Small Animal Imaging (CSAI) at Vanderbilt University, modulation frequencies of several kilohertz (kHz) may be obtained, resulting in diffusion times far below one millisecond, an order of magnitude smaller than those cited in any of the current literature using pulsed-gradient imaging techniques.

However, it must be noted, that while it may seem obvious that the effective diffusion times obtained with this technique are proportional to the period of gradient oscillation, the concept of a discrete diffusion time is not explicitly defined for continuous gradient waveforms. Nevertheless, this thesis, as well as several published articles implementing these techniques (5, 8-11),

often refer to an effective diffusion time for illustrative purposes, in order to describe the spatial range of molecular displacements. This effective diffusion time is typically quoted in accordance with the concepts presented by Gross and Kosfeld, et al. (12). In an article by Does and colleagues, (10), an analogy with the diffusion times of pulsed-gradient diffusion methods is made, resulting in effective diffusion times of 1/4 and 3/8 of an oscillation period for cosine- and sine-modulated waveforms, respectively. However, a more thorough description, as outlined by Fordham, et al. (13), and adapted to sine- and cosine-modulated gradients by Parsons, et al. (5), derives the effective diffusion terms using a cumulant expansion of the signal attenuation created by motion sensitizing gradients. While a complete description of these derivations will not be presented here, it will suffice to note that the effective diffusion times quoted above, and throughout this thesis, represent the zeroth order terms of these expansions, although higher order corrections may be more appropriate for subsequent analysis and data modeling. However, the applications outlined in this thesis will focus primarily on the spectral decomposition of the diffusion attenuated signal, defining the diffusion coefficient as a function of modulation frequency, as opposed to diffusion time, and zeroth order effective diffusion times will only be quoted briefly in reference to effective molecular displacements.

Experimental goals

Several previous studies implementing oscillating gradient techniques in model, as well as biological, systems have demonstrated the efficacy of these

methods for probing diffusion processes over very short diffusion times (5,8-11). In this thesis, these techniques have been extended to explore diffusion in biological systems at even shorter diffusion times than previously recorded, as well as assess the efficacy of these methods in evaluating tumor microstructure, and the response of tumors to chemotherapeutic treatment. In the paragraphs that follow, the salient features of each study will be briefly described, with an emphasis on the experimental goals of each experiment and the questions they aim to answer. The following chapters will then provide specific details of each experiment, along with scientific results and discussion.

The studies outlined in the subsequent chapters of this thesis are described briefly below:

(a) Chapter IV - The Effects Of Intracellular Organelles On The ADC Of Water Molecules In Cultured Human Embryonic Kidney Cells

While the scientific literature devoted to diffusion MRI methods has demonstrated a clear connection between variations in ADC and diseased tissue states such as stroke and cancer, the underlying pathophysiological mechanisms underlying these changes remain to be elucidated. For example, 20-50% decreases in ADC following ischemic stroke have been reported, with this variation attributed to any one, or some combination, of several possible factors including cellular swelling (14-15), reduced cytoplasmic streaming associated with decreased ATP levels (15-16), and changes in membrane permeability (17-18). However, there is little to no consensus about the degree to which each of

these factors may influence the drop in ADC. Even less is understood about the pathophysiological facts that influence ADC in cancer, where the heterogeneity of cellular architecture and vascularity greatly confound the issue. Therefore, in an effort to elucidate the intracellular mechanisms that influence variations in ADC, we have performed several studies on cultured cell samples manipulated with one of several drugs designed to target specific components of the intracellular milieu. These studies demonstrate the effects that Brefeldin A (Golgi-disrupting agent), Cytochalasin D (actin disrupting agent), and Nocodazole (microtubule disrupting agent) have on the ADC of packed 293-EBNA (human embryonic kidney) cells.

(b) CHAPTER V – New Insights Into Tumor Microstructure Using Temporal Diffusion Spectroscopy.

The use of diffusion MRI has gained increasing popularity in the cancer community for its sensitivity to changes in cellularity associated with tumor proliferation and/or treatment response. Several studies have demonstrated a clear increase in ADC associated with tumor response, as well as a decrease in ADC due to increases in cellularity (19-22). However, the majority of these studies continue to employ conventional PGSE techniques, measuring ADC over relatively long diffusion times (tens of milliseconds), thereby rendering their information incomplete. These types of experiments obscure information about tissue heterogeneity on an intracellular scale and ignore the effects that subcellular reorganization may have on tissue ADC. The studies described in

this thesis have aimed to address this shortcoming by measuring diffusion times approaching one millisecond in a C6 glioma model in rats *in vivo*, thereby demonstrating the increased contrast and details of tissue microstructure obtainable with OGSE methods.

(c) CHAPTER VI – Earlier Detection Of Tumor Treatment Response Using Magnetic Resonance Diffusion Imaging With Oscillating Gradients.

Since OGSE techniques are capable of resolving details of tumor microstructure obscured by conventional pulsed-gradient methods, these methods may provide greater insight into tumor treatment response as well. While several studies employing conventional techniques have demonstrated an increase in ADC following positive treatment effects, the aggressive nature of malignant tumors, particularly in the brain, has highlighted the need for assessing changes in tumor microstructure at their earliest onset. Most of the studies to date have shown that ADC increases with decreasing cellularity following therapeutic treatments; however, these studies have been unable to attribute these changes to any variations in tissue microstructure that precede changes in cellularity. In a 9L glioma model in rats *in vivo*, OGSE techniques have been shown to reveal changes in ADC prior to changes in cellularity, suggesting that these techniques are sensitive to microstructural changes occurring on an intracellular scale, thereby providing an earlier and/or more sensitive biomarker of treatment response.

Preliminary results in phantoms

The use of oscillating gradient diffusion NMR methods for the measurement of ADC in biological tissues is predicated upon the validation of these techniques in samples with known diffusivity. In order for these methods to be reliable, ADC values obtained in samples of pure distilled water and dimethyl sulfoxide (DMSO) at room temperature should match those values established in the literature. Furthermore, values obtained with PGSE and OGSE methods should also be equivalent in free (unrestricted) samples, within signal-to-noise (SNR) considerations.

A sample of pure distilled water in a sealed 8 mm outer diameter NMR tube, at room temperature, was placed in a 38 mm quadrature Litz birdcage coil for imaging at 4.7T. Pulsed gradient diffusion NMR images were collected at a field of view of 12 mm x 12 mm, slice thickness = 2 mm, matrix = 128 x 128, TR/TE = 3000/75.4 ms, number of acquisitions = 4, with δ = 5 ms, Δ = 30 ms, and b-values of 0 and 500 s/mm^2. Measurements were collected with both positive and negative gradient polarities, and geometrically averaged to eliminate gradient diffusion cross-terms associated with PGSE measurements (23). These cross-terms arise when imaging gradients add additional phase structure, and thus additional diffusion weighting, to that imparted by the initial diffusion gradient pulse. OGSE images were also collected using the same imaging parameters, at the same b-values, with the duration of gradient waveforms T = 33.33 ms, with the number of oscillations varying between N = 1 and N = 8, resulting in frequencies between 30 Hz and 240 Hz. Since no phase structure exists

following the implementation of oscillating gradient pulses (their zeroth order moment is zero), OGSE methods do not suffer the problem of cross-terms.

Whole sample regions of interest were drawn and average ADC values were calculated using equations (2.19) and (2.20), along with standard deviations of the mean. Mean ADC values (+/- standard deviation) were consistent across all OGSE frequencies, as well with PGSE methods; all ADC values were also consistent with the value for free water at room temperature cited in the literature, approximately ~2.3 $\mu m^2/ms$.

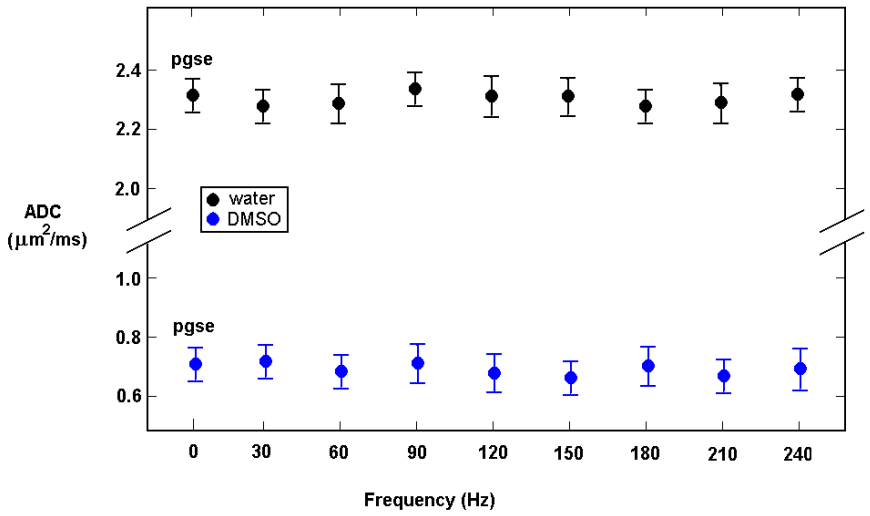

Figure 3.3. ADC vs oscillation frequency for room temperature samples of pure water and DMSO

In a separate experiment, an equal sized sample of DMSO was placed in the same RF coil as described above, and imaged using the same protocol for both OGSE and PGSE techniques. Again, whole sample regions of interest were drawn and mean ADC (+/- standard deviation) were calculated. Again, calculated values were all approximately equal to the value of the ADC for DMSO at room

temperature found in the literature, 0.73 μm^2/ms. Numerical values are not listed here, but values for both OGSE and PGSE experiments, for both water and DMSO, are shown graphically in Figure 3.3. For the convenience of displaying all values in a single plot, the PGSE value is plotted at $\omega = 0$. It is clear that ADC values across frequencies, as well as for PGSE, is approximately constant.

In addition to the previously described experiments, additional experiments were performed in order to validate the performance of specialized gradient hardware for use on the Varian 7T imaging system in the CSAI. Designed by Doty Scientific, Inc. (Columbia, SC, USA), this self-contained gradient coil and probe is capable of achieving linear gradients up to 3500 G/cm along a single axis (z-only).

A spin-echo spectroscopic pulse sequence was used to measure the whole sample ADC of pure water. The samples were maintained at approximately 18° C due to their proximity to the water cooling lines of the gradient hardware, which are also set at 18° C. Oscillation frequencies were measured in two hundred Hertz increments, ranging from 200 Hz to 2000 Hz, at b-values of 0 and 500 s/mm^2, with two oscillating gradient waveforms of 20 ms each, with TR/TE = 3000/48.2 ms, and number of acquisitions = 4. Pulsed-gradient spin-echo measurements were also collected with δ = 5 ms and Δ = 30 ms, with all other sequence parameters unchanged. Mean ADC values +/- standard deviation were calculated from peak spectroscopic amplitudes. Measurements were then repeated, with the same sample, four additional times over the course of one month, and mean values (+/- standard deviation of the

mean) were calculated. The values obtained for all frequencies, as well as for PGSE methods, are not listed here, but are presented graphically in figure 3.4; PGSE values are again plotted at $\omega = 0$. It is clear that mean values remain constant, independent of oscillation frequency or diffusion time.

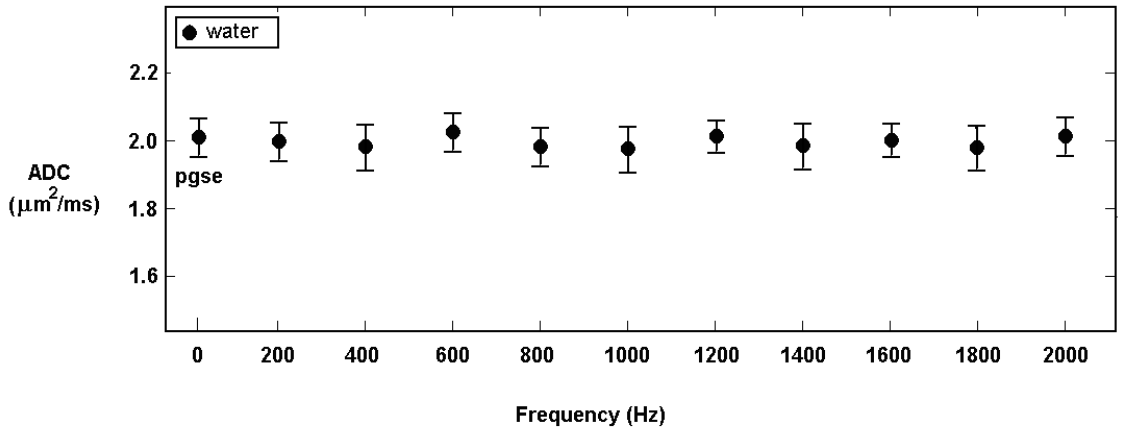

Figure 3.4. ADC vs oscillation frequency for samples of pure water at 18° C.

References

1. Stepisnik, J. Analysis of NMR self-diffusion measurements by density matrix calculation. Physica 1982;104B:350-61.

2. Callaghan PT, Stepisnik J. Frequency-domain analysis of spin motion using modulated-gradient NMR. J Magn Reson 1995;117:118-22.

3. Stepisnik J, Callaghan PT. Low-frequency velocity correlation spectrum of fluid in a porous media by modulated gradient spin echo. Magn Reson Imag 2001;19(3-4):469 –72.

4. Stepisnik J, Callaghan PT. The long time tail of molecular velocity correlation in a confined fluid: observation by modulated gradient spin-echo NMR. Physica B 2000;292:296-301.

5. Parsons EC, Does MD, Gore JC. Temporal diffusion spectroscopy: theory and implementation in restricted systems using oscillating gradients. Magn Reson Med 2006;55:75-84.

6. Callaghan PT, Macgowan D, Packer KJ, Zelaya FO. High resolution q-space imaging in porous structures. J Magn Reson 1990;90:177–82.

7. Callaghan PT. NMR imaging, NMR diffraction, and applications of pulsed gradient spin echoes in porous media. Magn Res Imag 1996;14:701-09.

8. Schachter M, Does MD, Anderson AW, Gore JC. Measurements of restricted diffusion using an oscillating gradient spin echo sequence. J Magn Reson 2000;147:232-37.

9. Parsons EC, Does MD, Gore JC. Modified oscillating gradient pulses for direct sampling of the diffusion spectrum suitable for imaging sequences. Magn Reson Imag 2003;21:279-85.

10. Does MD, Parsons EC, Gore JC. Oscillating gradient measurements of water diffusion in normal and globally ischemic rat brain. Magn Reson Med 2003;49:206-15.

11. Colvin DC, Yankeelov TE, Does MD, Yue Z, Quarles C, Gore JC. New insights into tumor microstructure using temporal diffusion spectroscopy. Cancer Res 2008 July;68:5941-5947.

12. Gross B, Kosfeld R. Anwendung der spin-echo-methode der messung der selbstdiffusion. Messtechnik 1969;77:171–7.

13. Fordham EJ, Mitra PP, Latour LL. Effective diffusion times in multiple pulse PFG diffusion measurements in porous media. J Magn Reson A 1996;121:187–192.

14. Verheul HB, Balazs R, Berkelbach van der Sprenkel JW, Tulleken CA, Nicolay K, Tamminga KS, van Lookeren C. Comparison of diffusion weighted MRI with changes in cell volume in a rat model of brain injury. NMR Biomed 1994;7:96–100.

15. van der Toorn A, Sykova E, Dijkhuizen RM, Vorisek I, Vargova L, Skobisova E, van Lookeren Campagne M, Reese T, Nicolay K. Dynamic changes in water ADC, energy metabolism, extracellular space volume, and tortuosity in neonatal rat brain during global ischemia. Magn Reson Med 1996;36:52–60.

16. Sehy JV, Zhao L, Xu J, Rayala HJ, Ackerman JH, Neil JJ. Effects of physiologic challenge on the ADC of intracellular water in the Xenopus oocyte. Magn Reson Med; 2004;52:239-47.

17. Szafer A, Zhong J, Gore JC. Theoretical model for water diffusion in tissues. Magn Reson Med 1995;33:697–712.

18. Pfeuffer J, Flogel U, Leibfritz D. Monitoring of cell volume and water exchange time in perfused cells by diffusion-weighted 1H NMR spectroscopy. NMR Biomed 1998;11:11–18.

19. Zhao M, Pipe JG, Bonnett J, Evelhoch JL. Early detection of treatment response by diffusion-weighted 1H-NMR spectroscopy in a murine tumour in vivo. Br J Cancer 1996;73:61-4.

20. McConville P, Hambardzumyan D, Moody JB, et al. Magnetic resonance imaging determination of tumor grade and early response to temozolomide in a genetically engineered mouse model of glioma. Clin Cancer Res 2007 May 15;13:2897-904.

21. Morse DL, Galons JP, Payne CM, et al. MRI-measured water mobility increases in response to chemotherapy via multiple cell-death mechanisms. NMR Biomed 2007 Jan 30;20:602-14.

22. Theilmann RJ, Borders R, Trouard TP, et al. Changes in water mobility measured by diffusion MRI predict response of metastatic breast cancer to chemotherapy. Neoplasia 2004 Nov-Dec;6:831-7.

23. Neeman M, Freyer JP, Sillerud LO. A simple method for obtaining cross-term-free images for diffusion anisotropy studies in NMR microimaging. Magn Reson Med 1991;21:138-43.

CHAPTER IV

THE EFFECTS OF INTRACELLULAR ORGANELLES ON THE ADC OF WATER MOLECULES IN CULTURED HUMAN EMBRYONIC KIDNEY CELLS

Abstract

The rate of self diffusion of water molecules in biological tissues is reduced from that in a purely aqueous medium due to the compartmentation of water by nuclear and cellular membranes, as well as by the presence of intracellular organelles. These cellular structures serve as barriers to molecular displacement and restrict the distance available for individual water molecules to diffuse. The effective rate of diffusion through a tissue is thus dependent upon the size and spacing of structures in the local cellular environment, and may be quantified in terms of an apparent diffusion coefficient (ADC), as measured with diffusion-weighted magnetic resonance imaging (DW-MRI). Diffusion-weighted MRI measurements of ADC may therefore be sensitive to pathologically induced variations in cellular morphology, and are commonly used to characterize tissue changes in pathologies such as stroke and cancer. However, while these pathologies are known to produce significant changes in ADC from that measured in healthy tissue, the underlying biophysical mechanisms influencing these variations remain poorly understood. Furthermore, the majority of DW-MRI experiments continue to examine these processes over relatively long diffusion times, such that variations in ADC reflect changes in cellular architecture over a

broad range of spatial scales. In order to provide further insight into the pathophysiological factors influencing tissue ADC, we have studied a model system of packed cultured human embryonic kidney cells at very short effective diffusion times (below one millesecond) following microtubule depolymerization, actin/cytoskeleton depolymerization, and disassembly of the Golgi complex. While the effects of Golgi disruption showed no change in ADC from that measured in control cells, depolymerization of the microtubule and actin filament networks showed decreases in ADC of approximately 2% and 4.2%, respectively, the latter of which was found to be statistically significant ($p < 0.05$).

Introduction

Tissue pathologies such as cancer and stroke, which are well known to alter tissue water diffusion rates, are routinely studied with diffusion-weighted MRI techniques. Increases in cellularity resulting from tumor proliferation, for example, have been shown to cause decreases in ADC (1-3), while the positive effects of therapeutic intervention, which typically decrease cellularity through apoptosis and necrosis, have been correlated with increases in ADC (4-9). The most notable application of DW-MRI, however, is in the diagnosis and evaluation of stroke, where decreases in ADC ranging from 20%-50% have been reported in the brain within minutes of ischemic insult, and often persisting for several hours to several days (10-13). However, despite the increasing utility and application of these techniques in both clinical and research settings, the specific biophysical mechanisms underlying these variations in ADC remain unclear.

Several theories regarding the decrease in ADC following ischemic stroke have been presented. An increase in cell volume resulting from swelling, for example, may result in a larger fraction of water in the highly restricted intracellular space, as well as increased extracellular tortuosity, thereby lowering ADC (14-16). However, changes in the intracellular ADC due to other mechanisms, such as reduced cytoplasmic streaming through ATP depletion, or increased viscosity due to microtubule disruption, have also been proposed (17-18), along with possible influences from variations in cellular membrane permeability (19-20). A confounding factor in all of these studies, however, is the consistent use of relatively long experimental diffusion times (tens of milliseconds), such that the effects of cellular structures on the order of 2-3 microns in size are indistinguishable from those on a whole cell scale. It is therefore of interest to explore the variations in ADC, which accompany cellular reorganization, at very short diffusion times in order to glean information about the pathophysiological factors influencing such changes.

In this study, we have implemented a previously described Oscillating Gradient Spin-Echo (OGSE) technique for measuring diffusion processes on a submillisecond scale in a model tissue system (21-24). By measuring the ADC in packed, cultured human embryonic kidney cells (293-EBNA), following manipulation of the intracellular milieu with various pharmaceuticals, we aim to provide insights into the influence that various intracellular organelles have on the effective rate of water diffusion in tissue. The effects of Golgi apparatus disruption (with brefeldin A), actin depolymerization (with cytochalasin D), and

microtubule depolymerization (with nocodazole) on ADC were measured using both OGSE and conventional, pulsed gradient spin echo (PGSE) techniques. Several OGSE measurements over a range of oscillation frequences up to two kilohertz (kHz), corresponding to effective diffusion times below one millisecond, were performed in order to establish the spatial scale over which structural restrictions have an effect on ADC. In addition, several representative cell samples, each treated with one of the prescribed drugs, were stained with antibody markers and imaged using laser scanning confocal microscopy in order to verify the alteration of intracellular structure compared with control cells. Finally, samples of bovine serum albumin (BSA) were measured at increasing concentration, using both methods, in order to assess the effects of protein content on ADC.

Materials and Methods

The 293-EBNA cell line was derived from primary embryonal human kidney cells transformed with sheared human adenovirus type 5 DNA and Epstein-Barr virus nuclear antigen (EBNA) 1. These cells can episomally amplify plasmids containing the viral EBV origin of replication, making them highly suitable for transfection.

Cells were cultured in suspension with F17 (Invitrogen, #0050092DK) supplemented with 0.1% Pluronic F68, 4 mM glutamine, and 50 mg/ml of G418. The culture was split every four days. The day of sample preparation, cell viability was measured using the trypan blue dye exclusion method. Cells were then

transferred to 250 μL sample tubes, with each sample containing approximately 2.5 x 10^7 cells in media. When indicated, the following drugs were applied at the following concentrations: brefeldin A at 350 μM (Sigma-Aldrich, #B7450), nocodazole at 100 nM (Sigma-Aldrich, #M1404), and cytochalasin D at 5 μM (Invitrogen, #PHZ1063). Control cell samples (N = 18) received an equal volume of phosphate buffered saline (PBS) only.

Treatment protocol

Brefeldin A is a lactone antibiotic that interferes with protein secretion, as well as protein transport between the Golgi apparatus and the endoplasmic reticulum, resulting in an accumulation of proteins in the endoplasmic reticulum (25-28). This drug has also been shown to collapse and redistribute Golgi stacks into tubular formations within minutes of exposure (26-28). Samples (N = 18) were treated with concentrations of 350 μM Brefeldin A and incubated at 37° for thirty minutes prior to data collection.

Cytochalasin D is a cellular membrane permeable, fungal metabolite well known to affect the morphological and motile properties of eukaryotic cells through its interaction with actin filaments. This treatment has been reported to severely disrupt actin network organization, increasing the number of actin filament ends and leading to aggregates, or foci, of filamentous fragments (29-32). Furthermore, given the role of actin filaments in the motility of intracellular organelles, metabolites, and nutrients, this drug is commonly used to significantly reduce or eliminate the effects of cytoplasmic streaming (31-32). All 293-EBNA

samples exposed to Cytochalasin D (N = 18) received doses of 5 μM concentration and were further incubated at 37° for approximately one hour prior to data collection.

Nocodazole is a synthetic, antimitotic agent commonly used to inhibit microtubule self-assembly, as well as depolymerize existing microtubules. Exposure to this drug has been reported to inhibit cytokinesis by altering the mitotic spindles, composed largely of microtubules, that align and separate chromosomes during cell division, arresting the cell cycle in the G2- or M-phase (33-35). This drug has also been reported to disrupt Golgi traffic, resulting in the formation of Golgi ministacks throughout the intracellular space (36-37). Samples (N = 18) were treated with 100 nM concentrations of Nocodazole and allowed to incubate at 37° for ninety minutes.

Approximately twenty minutes prior to each experiment, cell samples were removed from incubation and allowed to reach thermal equilibrium with room temperature. Samples were then centrifuged at 6000 rpm for five minutes, and identical volumes of supernatant fluid were removed with a micropipet. Sample tubes were then placed in the specialized gradient coil described earlier, and maintained at a temperature of approximately 19° C due to their proximity to the water cooling lines of the gradient hardware.

Phantom experiments in albumin

Bovine serum albumin samples of 5%, 10%, 15%, and 20% (w/w) were prepared by dissolving BSA powder (Sigma-Aldrich, St. Louis, MO) in pure

distilled water at room temperature. Solutions were then transferred to 250 μL sample tubes for data collection.

Data collection and analysis

Whole sample ^{1}H spectroscopic measurements of NMR water signal were acquired with a spin echo pulse sequence using a Varian 7T scanner implemented with a single axis (Z-only) gradient coil fitted with a 300 MHz transmit/receive radiofrequency (RF) probe designed by Doty Scientific, Inc. (Columbia, SC, USA). Diffusion-weighted spectra, consisting of 2048 complex data points, were acquired with the conventional pulsed-gradient spin echo method using diffusion-sensitizing gradient pulses of duration δ = 5 ms and separation Δ = 30 ms. Spectra were also collected implementing two cosine-apodized oscillating gradient waveforms, as described in Chapter III, each of duration T = 20ms, per sequence repetition, at oscillation frequencies between 200 Hertz (Hz) and 2 kiloHertz (kHz), in 200 Hz increments. Peak echo amplitudes, averaged from eight acquisitions (NEX = 8), were fit to the standard Stejskal-Tanner diffusion attenuation equation (2.19), with b-values calculate via equation (2.20). For all samples, and both imaging methods, b-values of 0, 300, and 600 s/mm^2 were used, along with TR = 3000 ms and TE = 54.5 ms.

Data analysis was performed using Matlab 2009a (The Mathworks, etc). All results are reported as mean $\pm$ standard deviation (SD). The statistical significance of differences in ADC values between treated and control groups, for

both imaging methods, was determined using student t-tests, with significance set at the $\alpha = 0.05$ level.

Results

A plot of mean ADC vs oscillation frequency is plotted in Figure 1 for cells treated with Brefeldin A, as well as for untreated control cells. Values for treated cells ranged from 1.12 ± 0.05 $\mu m^2/ms$ at 200 Hz, to 1.45 ± 0.08 $\mu m^2/ms$ at 2 kHz, while values for control cells ranged from approximately 1.12 ± 0.06 $\mu m^2/ms$ at 200 Hz to 1.46 ± 0.08 $\mu m^2 ms$ at 2 kHz. Values as measured with PGSE techniques were 0.43 ± 0.04 $\mu m^2/ms$ and 0.44 ± 0.05 $\mu m^2/ms$, for treated and controls, respectively. This difference was statistically insignificant ($p = 0.83$). The maximum difference in ADC across all frequencies was found to be 1.4% at 400 Hz, with an average difference across all frequencies of only $0.1 \pm 0.7\%$. Student t-tests showed no significant difference between treated and control ADC values, for all measured frequencies ($p >> 0.05$).

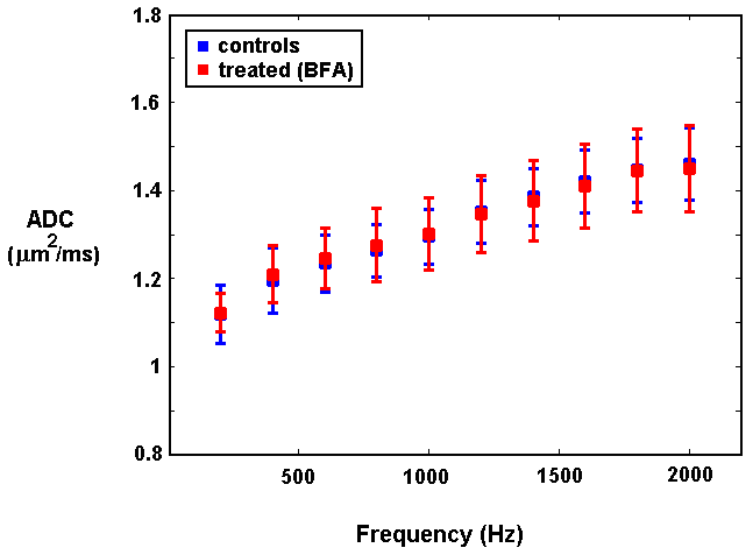

Figure 4.1. Mean ADC vs oscillation frequency for samples treated with Brefeldin A. Values for controls are also shown.

Mean ADC values vs oscillation frequency for cells treated with Cytochalasin D are shown in Figure 2, along with values for controls. It is clear from this figure

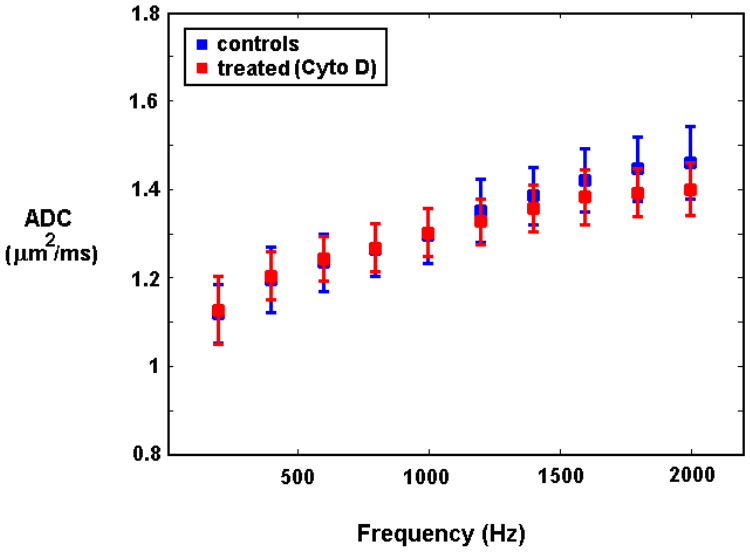

Figure 4.2. Mean ADC vs oscillation frequency for samples treated with Cytochalasin D. Values for controls are also shown.

that ADC values in treated and control samples are approximately equal at frequencies below 1 kHz, but begin to diverge at higher oscillation frequencies (decreasing 'effective' diffusion times). However, these differences are only statistically significant for the 1.8 kHz and 2.0 kHz oscillation frequencies (corresponding to 'effective' zeroth order diffusion times of approximately 139 μs and 125 μs, respectively). Table 1 shows the mean ADC values in treated cells, as well as controls, across all measured frequencies. The student t-test values for *p* are also shown. The mean ADC value measured in treated samples with PGSE techniques was 0.45 ± 0.05 μm^2/ms, compared to 0.44 ± 0.05 μm^2/ms for controls, as quoted earlier. A student t-test comparison found this difference to be insignificant (p = 0.77).

kHz	ADC (TX)	ADC (C)	p
0.2	1.13 (0.07)	1.12 (0.06)	0.82
0.4	1.20 (0.05)	1.20 (0.07)	0.76
0.6	1.24 (0.05)	1.23 (0.06)	0.73
0.8	1.27 (0.05)	1.26 (0.05)	0.85
1	1.30 (0.05)	1.30 (0.06)	0.78
1.2	1.33 (0.05)	1.35 (0.05)	0.35
1.4	1.36 (0.06)	1.38 (0.06)	0.26
1.6	1.38 (0.06)	1.42 (0.07)	0.16
1.8	1.39 (0.05)	1.45 (0.07)	0.049
2	1.40 (0.05)	1.46 (0.06)	0.048

Table 4.1. Mean ADC in cells treated (TX) with Cytochalasin D and control (C) cells as a function of oscillation frequency. Student t-test p-values are also shown.

Results for samples treated with Nocodazole are illustrated in Figure 3. While there appears to be a divergence in ADC values with increasing oscillation

frequency, student t-tests found these differences to be insignificant. At 2 kHz, the mean ADC value of treated samples was 1.43 ± 0.06 μm^2/ms, compared to 1.46 ± 0.08 μm^2/ms for controls, a decrease of just over 2%, although differences at lower frequencies are clearly much smaller. The mean value measured with PGSE was 0.45 ± 0.06 μm^2/ms; compared with the mean value for PGSE in controls quoted earlier, this difference was insignificant (p = 0.84). The approximate 2% difference in ADC at the highest oscillation frequency is similar to that reported by Sehy, et al (18), who measured ADC differences in Xenopus oocytes following treatment with Nocodazole at an effective diffusion time of 4.7 ms.

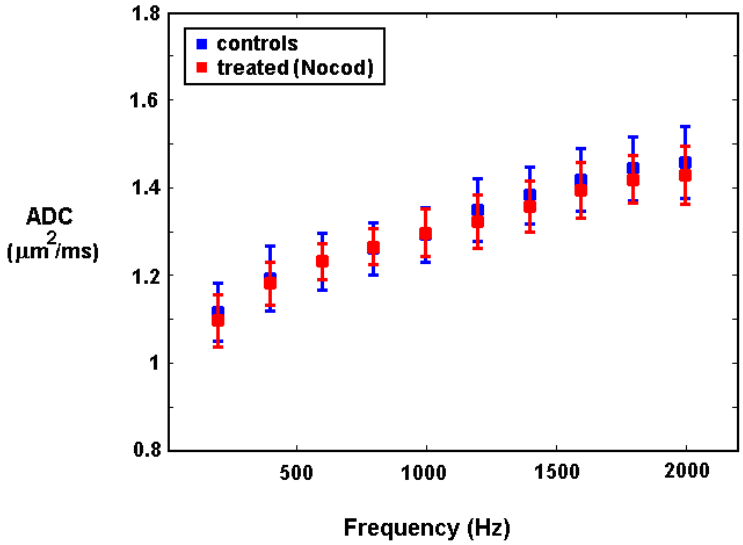

Figure 4.3. Mean ADC vs oscillation frequency for samples treated with Nocodazole. Values for controls are also shown.

A plot of the percentage difference in mean ADC values, between treated samples and controls, is shown in figure 4.4 for all three treatments. The percentage difference was defined as:

$$\%\ difference = \frac{mADC_C - mADC_{TX}}{mADC_C} \times 100\%, \qquad (4.5)$$

where $mADC_C$ and $mADC_{TX}$ correspond to the mean ADC values across all N = 18 samples for control and treated samples, respectively. While student t-tests did not indicate a significant difference in ADC values, at any frequency, for the Brefeldin A or Nocodazole treatments, it is clear from this figure that ADC values above 1000 Hz begin to decrease from those values below 1000 Hz for all treatments. At this oscillation frequency, the effective zeroth order diffusion time is approximately 0.25 ms, corresponding to a diffusion length of approximately one micron (assuming an unrestricted ADC of ~2 μm^2/ms). This indicates that restriction effects on the order of 1-2 microns may have an effect on ADC values; however, these effects would be obscured using the long diffusion times implemented in most PGSE studies.

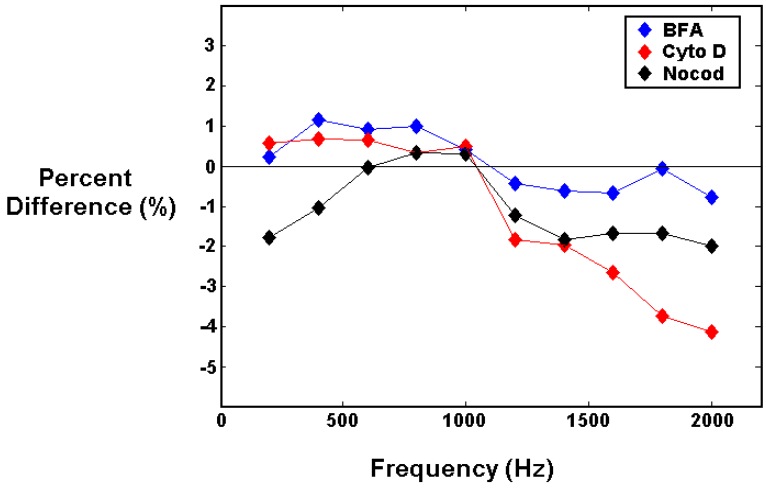

Figure 4.4. Mean percentage difference in ADC between all treated samples and controls for all oscillation frequencies.

Results from experiments in BSA phantoms are shown in Figure 4.5. On the left, ADC is plotted against oscillation frequency for OGSE methods, at all four concentrations. Standard deviation error bars have been omitted to avoid cluttering the image, but were smaller than ±1% for all data. On the right, ADC is plotted against BSA concentration for PGSE experiments, as well as for four of the oscillation frequencies used. Standard deviation error bars have again been omitted to maintain image clarity. With both imaging techniques, there appears to be a linear relationship between ADC and albumin content, and lines of best fit have been drawn.

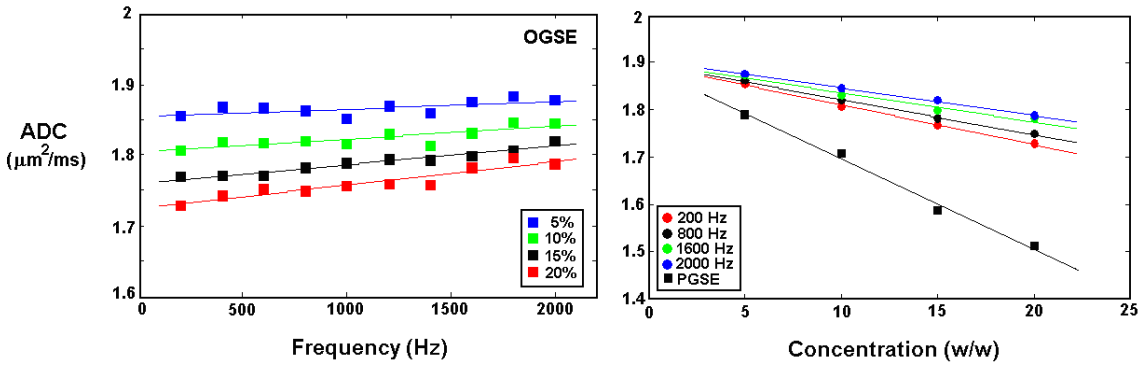

Figure 4.5. ADC vs oscillation frequency for all four BSA concentrations is shown on the left. ADC vs BSA concentration for PGSE experiments, as well as four oscillation frequencies, is shown on the right.

Discussion

The studies outlined in this chapter are aimed at providing a better understanding of the biophysical mechanisms underlying variations in ADC resulting from pathology. While several studies (as described in the Introduction) have approached this problem by examining ADC variations that result from changes in cell volume, the experiments in this work seek to illustrate the effects that specific components of the intracellular milieu have on tissue ADC, independent of cell volume effects. Furthermore, the studies outlined here aim to provide additional information about the spatial scale over which intracellular organelles influence ADC by measuring these values over a range of spatial scales using oscillating gradient spin-echo MRI techniques, in addition to conventional pulsed-gradient methods.

While it was described earlier that such continuous waveforms do not lend themselves to the definition of a discrete diffusion time, as typically quoted in conventional PGSE studies, there is a clear inverse relationship between

oscillation frequency and effective diffusion time. This relationship has been validated in previous studies (21-22). Therefore, by measuring ADC values with oscillating gradient techniques up to 2 kHz in frequency, effective diffusion times well below one millisecond may be achieved. These effective diffusion times may then be used to infer information about the approximate path lengths travelled by diffusing water molecules in restricted media.

At a diffusion time of 30 ms, an unrestricted water molecule, diffusing at the free water rate of 2.0 μm^2/ms, would travel approximately 11 microns, a distance equivalent to a typical cell diameter. The ADC of biological water, as measured with PGSE techniques, is therefore greatly reduced from the free water value due to the numerous restrictions each molecule experiences over the course of this relatively long diffusion time. On the other hand, the ADC as measured with OGSE methods is much higher, due to less interaction with restrictive structures at shorter diffusion times. For example, at the lowest frequency of oscillation used here, 200 Hz, the period of one oscillation is 5 ms, corresponding to a zeroth order effective diffusion time of 1.25 ms, and a one-dimensional path length of just over 2 microns. At the highest oscillation frequency of 2 kHz, the zeroth order effective diffusion time is ten times smaller than at 200 Hz, or approximately 125 μs. This corresponds to a one-dimensional path length of ~0.7 microns, thus explaining the large difference in ADC between PGSE and OGSE measurements.

The approximate 25-30% increase in ADC between 200 Hz and 2 kHz, for both treated samples and controls, suggests that the correlation time for

significant changes to occur in the autocorrelation of molecular velocities is on the order of a millisecond. Furthermore, given that the mean ADC values at 2 kHz, for all samples in this study, remain approximately 25-30% below the free water value of ~2.0 μm^2/ms, it is reasonable to infer that a significant fraction of water molecules in these cells, on average, do not diffuse more than approximately one micron before experiencing restrictive effects. However, the reduction in ADC from free water values at these short diffusion times may also reflect such factors as the intrinsic viscosity of the cytosol, or other unknown effects. Furthermore, the increasing divergence in ADC from control values with increasing frequency, particularly in cells treated with Cytochalasin, and to a lesser degree with Nocodazole, suggest that such differences may become significant at even higher frequencies.

Several studies have proposed that decreases in ADC following ischemic insult may result in increased intracellular viscosity due to the redistribution of the cytosolic proteins created by the disassociation and fragmentation of microtubules and other organelles. Such effects would presumably be more pronounced at shorter diffusion times, since the ADC at long diffusion times would be dominated by the effects of restrictive barriers. A study by Kao, et al. (38) has promoted the idea of an “apparent viscosity” to reflect the combined influences of fluid viscosity, added collisions with fragmented proteins, and the possible addition of binding sites associated with those proteins. Work by Sehy and colleagues (39-40) has demonstrated similar findings, showing decreasing ADC with increasing protein content, and several other groups have shown that

water existing in the hydration layer of proteins may contribute to significant reductions in ADC as well (41-46).

As protein concentration in aqueous solution increases, the ADC decreases, particularly at long diffusion times. Other groups have reported similar results in BSA (41-44). However, at very short diffusion times, such as those implemented here with OGSE techniques, there is only a slight increase in ADC with increasing frequency. For example, at a BSA concentration of 5%, the ADC value increases by only ~1% from 200 Hz to 2000Hz, compared to approximately 3.5% at 20% BSA concentration. On the other hand, there is a clear decrease in ADC with increasing albumin concentration at each frequency, as highlighted by the four frequencies plotted against concentration in the right panel of Figure 4.5. The mechanisms underlying these variations are not clear. Although the presence of large proteins do provide obstructions to free diffusion, thereby lowering ADC, it is not conclusive whether such decreases may be attributed to restriction effects alone, or if other mechanisms, such as protein hydration or increased viscosity, may play a role.

References

1. Gauvain KM, McKinstry RC, Mukherjee P, et al. Evaluating pediatric brain tumor cellularity with diffusion-tensor imaging. Amer J Roent 2001;177:449-54.

2. Wang XZ, Wang B, Gao, ZQ, et al. Diffusion-weighted imaging of prostate cancer: correlation between apparent diffusion coefficient values and tumor poliferation. J Magn Reson Imag 2009;29:1360-66.

3. Guo AC, Cummings TJ, Dash RC, Provenzale JM. Lymphomas and high-grade astrocytomas: comparison of water diffusibility and histologic characteristics. Radiol 2002;224:177-83.

4. Zhao M, Pipe JG, Bonnett J, Evelhoch JL. Early detection of treatment response by diffusion-weighted 1H-NMR spectroscopy in a murine tumour in vivo. Br J Cancer 1996;73:61-4.

5. Seierstad T, Folkvord S, Røe K, Flatmark K, Skretting A, Olsen DR. Early changes in apparent diffusion coefficient predict the quantitative antitumoral activity of capecitabine, oxaliplatin, and irradiation in HT29 xenografts in athymic nude mice. Neoplasia 2007 May;9:392-400.

6. McConville P, Hambardzumyan D, Moody JB, et al. Magnetic resonance imaging determination of tumor grade and early response to temozolomide in a genetically engineered mouse model of glioma. Clin Cancer Res 2007 May 15;13:2897-904.

7. Morse DL, Galons JP, Payne CM, et al. MRI-measured water mobility increases in response to chemotherapy via multiple cell-death mechanisms. NMR Biomed 2007 Jan 30;20:602-14.

8. Theilmann RJ, Borders R, Trouard TP, et al. Changes in water mobility measured by diffusion MRI predict response of metastatic breast cancer to chemotherapy. Neoplasia 2004 Nov-Dec;6:831-7.

9. Schepkin VD, Chenevert TL, Kuszpit K, et al. Sodium and proton diffusion MRI as biomarkers for early therapeutic response in subcutaneous tumors. Magn Reson Imag 2006 Apr;24:273-8.

10. Moseley ME, Cohen Y, Mintorovitch J, et al. Early detection of regional cerebral-ischemia in cats – Comparison of diffusion-weighted and T_2-weighted MRI and spectroscopy. Magn Reson Med 1990;14:330-46.

11. Mintorovitch J, Mosely ME, Chileuitt L, Shimizu H, Cohen Y, Weinstein PR. Comparison of diffusion-weighted and T_2-weighted MRI for the early detection of cerebral-ischemia and reperfusion in rats. Magn Reson Med 1991;18:39–50.

12. Warach S, Chien D, Li W, Ronthal M, Edelman RR. Fast magnetic resonance diffusion-weighted imaging of acute human stroke. Neurology 1992;42:1717–1723.

13. Schlaug G, Siewert B, Benfield A, Edelman RR, Warach S. Time course of the apparent diffusion coefficient (ADC) abnormality in human stroke. Neurorad 1997;49:113-19.

14. van der Toorn A, Sykova E, Dijkhuizen RM, Vorisek I, Vargova L, Skobisova E, van Lookeren Campagne M, Reese T, Nicolay K. Dynamic changes in water ADC, energy metabolism, extracellular space volume, and tortuosity in neonatal rat brain during global ischemia. Magn Reson Med 1996;36:52–60.

15. Verheul HB, Balazs R, Berkelbach van der Sprenkel JW, Tulleken CA, Nicolay K, Tamminga KS, van Lookeren C. Comparison of diffusion weighted MRI with changes in cell volume in a rat model of brain injury. NMR Biomed 1994;7:96–100.

16. Niendorf T, Dijkhuizen RM, Norris DG, van Lookeren C, Nicolay K. Biexponential diffusion attenuation in various states of brain tissue: implications for diffusion-weighted imaging. Magn Reson Med 1996;36:847–857.

17. Duong TQ, Ackerman JJ, Ying HS, Neil JJ. Evaluation of extra- and intracellular apparent diffusion in normal and globally ischemic ratbrain via 19F NMR. Magn Reson Med 1998;40:1–13.

18. Sehy JV, Zhao L, Xu J, Rayala HJ, Ackerman JH, Neil JJ. Effects of physiologic challenge on the ADC of intracellular water in the Xenopus oocyte. Magn Reson Med; 2004;52:239-47.

19. Szafer A, Zhong J, Gore JC. Theoretical model for water diffusion in tissues. Magn Reson Med 1995;33:697–712.

20. Pfeuffer J, Flogel U, Leibfritz D. Monitoring of cell volume and water exchange time in perfused cells by diffusion-weighted 1H NMR spectroscopy. NMR Biomed 1998;11:11–18.

21. Parsons EC, Does MD, Gore JC. Modified oscillating gradient pulses for direct sampling of the diffusion spectrum suitable for imaging sequences. Magn Reson Imag 2003;21:279-85.

22. Parsons EC, Does MD, Gore JC. Temporal diffusion spectroscopy: theory and implementation in restricted systems using oscillating gradients. Magn Reson Med 2006;55:75-84.

23. Does MD, Parsons EC, Gore JC. Oscillating gradient measurements of water diffusion in normal and globally ischemic rat brain. Magn Reson Med 2003;49:206-15.

24. Colvin DC, Yankeelov TE, Does MD, Yue Z, Quarles C, Gore JC. New insights into tumor microstructure using temporal diffusion spectroscopy. Cancer Res 2008 July;68:5941-5947.

25. Fujiwara T, Oda K , Yokota S, Takatsukig A, Ikeharan Y. Brefeldin A causes disassembly of the Golgi complex and accumulation of secretory proteins in the endoplasmic reticulum. J Biol Chem 1988;263:18545-52.

26. Lippincott-Schwartz J, Yuan LC, Bonifacino JS, Klausner RD. Rapid redistribution of Golgi proteins into the ER in cells treated with brefeldin A: Evidence for membrane cycling from Golgi to ER. Cell 1989;56:801-13.

27. Klausner RD, Donaldson JG, Lippincott-Schwartz J. Brefeldin A: Insights into the control of membrane traffic and organelle structure. J Cell Biol 1992;116:1071-80.

28. Reaves B, Banting G. Perturbation of the morphology of the trans-Golgi network following Brefeldin A treatment: redistribution of a TGN-specific integral membrane protein, TGN38. J Cell Biol 1992;116:85-94.

29. Bradley MO. Microfilaments and cytoplasmic streaming: inhibition of streaming with cytochalasin D. J Cell Sci 1973:12:327-43.

30. Miranda AF, Godman GC, Deitch AD, Tanenbaum SW. Action of cytochalasin D on cells of established lines. I. Early events. J Cell Biol 1974;61:481-500

31. Schliwa M. Action of Cytochalasin D on cytoskeletal networks. J Cell Biol 1982;92:79-91.

32. Wakatsuki T, Schwab B, Thompson NC, Elson EL. Effects of cytochalasin D and latrunculin B on mechanical properties of cells. J Cell Sci 2001;114:1025-36.

33. Samson F, Donoso JA, Heller-Bettinger I, Watson D, Himes RH. Nocodazole action on tubulin assembly, axonal ultrastructure and fast axoplasmic transport. J. Pharmacoi Exp Ther 1979;208:411-17.

34. Vasquez RJ, Howell B, Yvon AM, Wadsworth P, and Cassimeris L. Nanomolar concentrations of nocodazole alter microtubule dynamic instability in vivo and in vitro. Mol Biol Cell 1997;8:973-85.

35. Dubel S, Little M. Microtubule-dependent cell cycle regulation is implicated in the G2 phase of Hydra cells. J Cell Sci 1988;91:347-59.

36. Minin AA. Dispersal of Golgi apparatus in nocodazole-treated fibroblasts is a kinesin-driven process. J Cell Sci 1997;110:2495-505.

37. Storrie B, White J, Röttger S, Stelzer EHK, Suganuma T, Nilsson T. Recycling of Golgi-resident Glycosyltransferases through the ER Reveals a Novel Pathway and Provides an Explanation for Nocodazole-induced Golgi Scattering. J Cell Biol 1998;143:1505-21.

38. Kaoj HP, Abney JR, Verkman AS. Determinants of the translational mobility of a small solute in cell cytoplasm. J Cell Biol 1993:120:175-84.

39. Sehy JV, Ackerman JH, Neil JJ. Water and lipid MRI of the Xenopus oocyte. Magn Reson Med2001;46:900-6

40. Sehy JV, Ackerman JH, Neil JJ. Apparent diffusion of water, ions, and small molecules in the Xenopus oocyte is consistent with Brownian motion. Magn Reson Med 2002;48:42-51.

41. Baranowska HM, Olszewski KJ. The hydration of proteins in solutions by self-diffusion coefficients NMR study. Biochim Biophys Acta 1996;1289:312-14.

42. Kimmich R, Klammler F, Skirda VD, Serebrennikova IA, Maklakov AI, Fatkullin N. Geometrical restrictions of water diffusion in aqueous protein systems. A study using NMR field-gradient techniques. Appl Magn Reson 1993;4:425-40.

43. Kotitschke K, Kimmich R, Rommel E, Parak F. NMR study of diffusion in protein hydration shells. Prog Colloid Polym Sci 1990:83:211-15.

44. Marchi M, Sterpone F, Ceccarelli M. Water rotational relaxation and diffusion in hydrated lysozome. J Am Chem Soc 2002;124:6787-91.

CHAPTER V

[1]NEW INSIGHTS INTO TUMOR MICROSTRUCTURE USING TEMPORAL DIFFUSION SPECTROSCOPY[1]

Abstract

Magnetic resonance images that depict rates of water diffusion in tissues can be used to characterize the cellularity of tumors, and are valuable in assessing their early response to treatment. Water diffusion rates are sensitive to the cellular and molecular content of tissues and are affected by local micro-structural changes associated with tumor development. However, conventional maps of water diffusion reflect the integrated effects of restrictions to free diffusion at multiple scales up to a specific limiting spatial dimension, typically several microns. Such measurements cannot distinguish effects caused by structural variations at a smaller scale. Variations in diffusion rates then largely reflect variations in the density of cells, and no information is available about changes on a sub-cellular scale. We report here our experiences using a new approach based on Oscillating Gradient Spin-Echo MRI methods which can differentiate the influence on water diffusion of structural changes on scales much smaller than the diameter of a single cell. MR images of glioblastomas in rat brain in vivo demonstrate an increased contrast and spatial heterogeneity when diffusion measurements are selectively sensitized to shorter distance scales. These

[1] Published in *Cancer Research* 68; 5941, July 15, 2008.

results demonstrate the benefit of OGSE methods for revealing microscopic variations in tumors in vivo and confirm that diffusion measurements depend on factors other than cellularity.

Introduction

Magnetic resonance imaging (MRI) can be adapted to provide noninvasive measurements of water mobility in biological tissues, and diffusion-weighted MRI has been widely adopted for clinical and research applications. The rate of water diffusion within tissues measured by conventional MR methods is found to be significantly lower than for free solutions, and measurements are often summarized in terms of an apparent diffusion coefficient (ADC), which is a measure of the effective distance over which water can migrate within tissue within a specified time. The ADC differs from the intrinsic diffusion coefficient D_0 in a manner that is dependent upon the tissue's microstructure and composition. A number of pathological conditions, such as ischemic stroke (1-2) and prolonged seizures (3-4), produce significant changes in the ADC compared to healthy tissues. The ADCs of several tumors have been shown to be significantly different from those of surrounding healthy tissues, a finding that has led to interest in using diffusion-sensitive MRI not only as a diagnostic tool, but also to assess tumor cellularity and changes in ADC that may reflect the response to treatments (5-6).

The increasing use of diffusion MRI in clinical oncology has highlighted the need for a more quantitative understanding of the pathophysiological factors

affecting water diffusion rates in tissues. The rate of water diffusion in tissues is reduced whenever there are physical obstructions or hindrances to free Brownian motion and free exchange between different compartments, giving rise to restricted diffusion. Currently employed measuring techniques are sensitive to the integrated effects of restrictions on water displacements at all spatial scales up to the order of several microns. The specific contributions of interactions with sub-cellular structures and macromolecules that occur on much smaller scales cannot then be distinguished from effects at larger dimensions. In particular, while it is well documented that an increase in tumor cellularity is marked by a decrease in ADC, and that an increase in ADC is often indicative of positive treatment response (7-14), the roles that changes at the sub-cellular level play in affecting such measurements are not clear. Changes in membrane permeabilities, the relative sizes of various intracellular and extracellular water fractions, active transport mechanisms, and the precise nature of intracellular structures and their organization, may all have significant influences on the aggregate ADC of tissue (15-18). Because conventional measurements are unable to distinguish restrictions to diffusion that occur on scales smaller than several microns, we have explored a modified imaging technique that can selectively examine water mobility over much shorter spatial scales, much less than the diameter of a single cell. In this paper we report how information may be gleaned about structural changes that occur on a sub-cellular scale rather than merely reflecting cell density.

A more complete description of the physics of diffusion MRI may be found elsewhere (19-21), but here we briefly illustrate the conceptual difference between our method and currently employed techniques. Figure 5.1 depicts the pulsed gradient spin-echo (PGSE) pulse sequence, the most commonly used method for measurements of ADC with MRI.

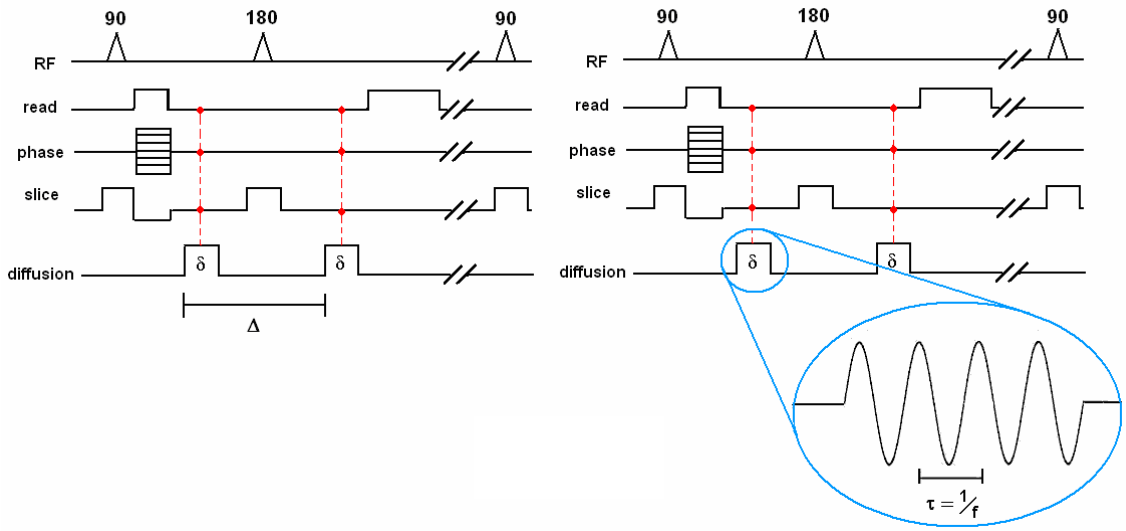

Figure 5.1. Pulse sequence diagram illustrating PGSE and OGSE techniques.

The significant feature of this sequence is that it employs a pair of diffusion sensitizing magnetic field gradients, each of equal time length δ and magnitude G_D, separated by a time Δ, the "diffusion interval." The initial gradient pulse serves to label the phase of the transverse magnetization from water molecules spatially along the applied gradient direction, and the subsequent pulse exactly reverses this phase if they do not move. Water molecules which undergo displacements along that particular direction in the diffusion time Δ will retain a net phase shift, and the mixing of different phases from random movements

within the sample causes the net signal to be reduced. Thus the MR signal is attenuated to a degree that depends on the variance of the displacements of water molecules during the interval Δ and the gradient G_D. A more quantitative description of this attenuation is presented in the Methods section.

A practical consideration for making measurements of diffusion is the gradient strength available to induce significant signal attenuation. As shown below, the interval Δ must be increased to achieve reasonable reductions in signal strength when the gradients are weak. Given the practical limits on the strengths of gradients available on current scanners, this interval is usually at least on the order of tens of milliseconds, and is often set to several tens of milliseconds to achieve bigger effects (22-30). The Einstein equation relates the mean molecular displacement due to diffusion *D* over a time Δ: for a one dimensional random walk along the direction of the gradient the mean square displacement of the water molecules is,

$$\left\langle L^2 \right\rangle = 2D\Delta \,, \tag{5.1}$$

For example, a molecule diffusing at the rate of 2.5 μm^2/ms (≈ D_0 for free water at 37 degrees C) for an interval of 35 ms should on average undergo a net displacement of just over 13 microns, a distance comparable to the diameter of a typical cell. If water molecules encounter a restrictive barrier to diffusion on or below this scale, $\langle L \rangle$ will be smaller and the diffusion rate (ADC) will appear to be lower. But if restrictions also occur on even smaller scales, these effects will not be distinct at this diffusion interval. No information can be obtained about effects below the scale of $\langle L \rangle$. In order to overcome this limitation, we have implemented

an oscillating gradient spin-echo (OGSE) technique to be able to probe tumor microstructure at smaller dimensions. In this method, the pulsed gradients of the PGSE technique are replaced with sinusoidally varying gradients of frequency *f* (Figure 5.1b). This approach reduces the effective diffusion interval below the period of one oscillation, yet the achieved signal attenuation is still significant (see Methods). By oscillating gradients at several hundred Hertz (Hz), effective diffusion times approaching one millisecond may be achieved, allowing spatial displacements nearly an order of magnitude smaller than those obtainable with current PGSE techniques to be probed (31-32). Furthermore, by varying the frequency *f* it is possible to characterize the various scales over which restrictions to diffusion occur in a complex system.

In this study, we have applied OGSE methods to map the ADC in rats bearing glioblastoma tumors *in vivo* and *ex vivo* to illustrate the increased contrast and structural information that is achievable using such techniques. By demonstrating an increased contrast in calculated ADC maps, as well as quantitatively different ADCs measured in pathological regions, we demonstrate the potential benefit of OGSE techniques over currently employed techniques for evaluating microscopic variations in tumor microstructure.

Materials and Methods

Animal Model

All procedures were approved by our Institution's Animal Care and Usage Committee. Ten male Wistar rats (approximately 250g) were immobilized and anesthetized with a 2%/98% isoflurane/oxygen mixture. The rats were inoculated with 1×10^5 C6 glioblastoma cells using a 10-mL gastight syringe approximately one mm anterior and two mm lateral to the bregma on the right side of the head, at a depth of three millimeters relative to the dural surface. The C6 is a common brain tumor model that is widely used in experimental neuro-oncology to evaluate tumor growth, invasion, migration, and blood-brain-barrier disruptions, and has been used extensively to investigate the efficacy of various therapies including chemotherapy and radiation therapy (33). Complete and acceptable data were obtained from only 7 rats.

In vivo imaging

Fourteen days following tumor inoculation, MRI studies were performed on a Varian 4.7T horizontal bore imaging system (Palo Alto, CA, USA). Anesthesia was induced and maintained with a 2%/98% isoflurane/oxygen mixture, and a constant body temperature of 37° C was maintained using heated air flow. Animals were placed in a prone position and imaged using a quadrature 63mm inner diameter RF coil.

A multi-slice gradient echo imaging sequence (TR = 150 ms, TE = 3.5 ms, 128x128 matrix, 36x36mm^2 FOV, 2mm slice thickness) was used to acquire seven slices in each imaging plane for proper positioning and slice selection. A subsequent T_2-weighted, single slice fast spin-echo scan with 8 echoes (TR= 2000, 13ms echo spacing, 128x128 matrix, 36x36mm^2 FOV, 2mm slice thickness) was used for anatomical clarification of the tumor region. The same slice was then imaged using our oscillating gradient spin-echo technique, with oscillation frequencies ranging from 30 to 240 Hz, in 30 Hz increments. Diffusion-weighted scans were respiratory-gated, with TR/TE = 2000/76ms, 64x64 matrix size, 2 mm slice thickness, 36x36mm^2 FOV. Two acquisitions were averaged for each image, each with b-values of 0 and 401 s/mm^2. Each gradient pulse was 33.33 msec duration, so that the number of cycles varied from 1 to 8 and the gradient amplitude varied from 4.77 gauss/cm to 36.0 gauss/cm. Following the OGSE imaging, conventional PGSE images were obtained with δ = 3 ms, Δ = 15 ms, and the diffusion sensitizing gradient set to 12.18 gauss/cm to obtain a b-value of 401 s/mm^2, equal to that in the OGSE scans. Also, all PGSE scans were collected twice, each with opposite gradient polarity, and geometrically averaged to eliminate the presence of gradient cross-terms that may influence ADC measurements (34). These cross-terms are absent in our version of OGSE images. All other imaging parameters were identical to the OGSE acquisitions. Diffusion gradients were placed simultaneously along all three imaging coordinate axes to obtain the maximum diffusion weighting with the available gradient amplitudes.

In addition, a single animal was imaged at higher resolution in order to more finely probe intra-tumor heterogeneity and facilitate comparison to *ex vivo* images acquired after perfusion fixation of the brain with formalin. For this animal, both PGSE and OGSE images were collected *in vivo* using a single 1 mm axial slice, with TR/TE = 2000/76 ms, 128x128 matrix, 36x36mm^2 FOV, with NEX = 6. Only the 240 Hz OGSE data were collected.

Perfusion fixation

Four days following the imaging experiment, the rat was anesthetized, and then anti-coagulated with 80 mg/kg pentobarbital i.p., with 0.01 ml/100 g heparin added to the syringe. Once deep anesthesia was accomplished, surgery was performed to allow a blunt 16 gauge perfusion needle to be inserted into the left cardiac ventricle toward the left ventricular outflow tract, and just into the aorta. A saline wash solution was then perfused, with the right atrial appendage cut immediately to allow the rapid outflow of blood and wash solution. At this time, the perfusate was switched to 10% formalin in 0.1 M phosphate buffer. Fixation began at a high flow rate (50 cc/min) for 2-5 minutes, then continued at a slow drip for 12-15 minutes until adequate fixation was achieved. The whole brain tissue was then dissected and placed in fixative solution. Approximately 24 hours later, the fixative was removed and the brain was placed in phosphate buffered saline (PBS, 1X) for imaging.

Ex vivo imaging

Ex vivo images were performed on a single axial slice with TR/TE = 2000/76, 96x96 matrix, 18x18mm^2 FOV, 1 mm slice thickness, and NEX = 60. As with the *in vivo* data, all PGSE diffusion parameters were kept the same (including reversed polarity of the gradient amplitudes), and only the 240 Hz OGSE data were obtained. Although we cannot be certain that the single imaging slice acquired in the *ex vivo* experiment was exactly the same as that recorded *in vivo*, several multi-slice scout images were used to choose the slice that most closely resembled the *in vivo* data.

Calculation of ADC maps

Using the formalism of Stejskal and Tanner (19), the diffusion attenuated signal magnitude, *S*, is related to the unweighted signal, S_0, such that:

$$S = S_0 e^{-b \cdot ADC} \tag{5.2}$$

where *b* represents the diffusion-weighting imparted upon the sample by the time-dependent magnetic field gradients $G_D(t)$ and is equal to:

$$b = \gamma^2 \int_0^T dt \left[\int_o^t G_D(t')dt' \right]^2 , \tag{5.3}$$

where γ is the gyromagnetic ratio of hydrogen protons, and is equal to 42.58 Mhz/Tesla. Integration of this equation for the pulsed-gradient spin-echo experiment yields:

$$b = \gamma^2 G_D^2 \delta^2 (\Delta - \frac{\delta}{3}) , \tag{5.4}$$

while the integration for the cosine-modulated gradients used in this study yields:

$$b = \frac{1}{8}\left(\frac{\gamma G_D}{\pi N}\right)^2 T^3\left(1-\frac{1}{8N}\right), \tag{5.5}$$

where N is the number of gradient oscillations per diffusion-weighting duration T. The period, P, of one oscillation is equal to

$$P = \frac{T}{N} = \frac{1}{f}, \tag{5.6}$$

where f is the frequency of oscillation (in Hz). The effective diffusion time for the oscillating gradient waveform is then:

$$\Delta_{eff} = \frac{P}{4} = \frac{1}{4f}. \tag{5.7}$$

(For a more complete description of these calculations, see reference 32). Note that the effective diffusion time in OGSE depends on the oscillation period only, and is no longer related to the time between gradient pulses.

All data were analyzed using Matlab 2007a (The Mathworks, Natick, MA, USA). Diffusion weighted images were registered to non-diffusion weighted (b = 0) images using a rigid registration algorithm. Regions of interest in sub-cortical grey matter, tumor, and whole brain were manually drawn and segmented with reference to high resolution anatomical images.

Results

Figure 5.2 shows the maps of ADC, calculated using equation (5.2) above, obtained in one representative animal for different gradient frequencies. The ADC map obtained at the lowest frequency, 30 Hz, is similar to that obtained by the PGSE method, as expected. However, as the oscillation frequency is

increased, there is increased contrast between the tumor and surrounding tissues, and new features appear within the heterogeneous tumor volume. These features correspond to regions in which the degree of restriction to diffusion varies more at shorter time and distance scales than at longer times.

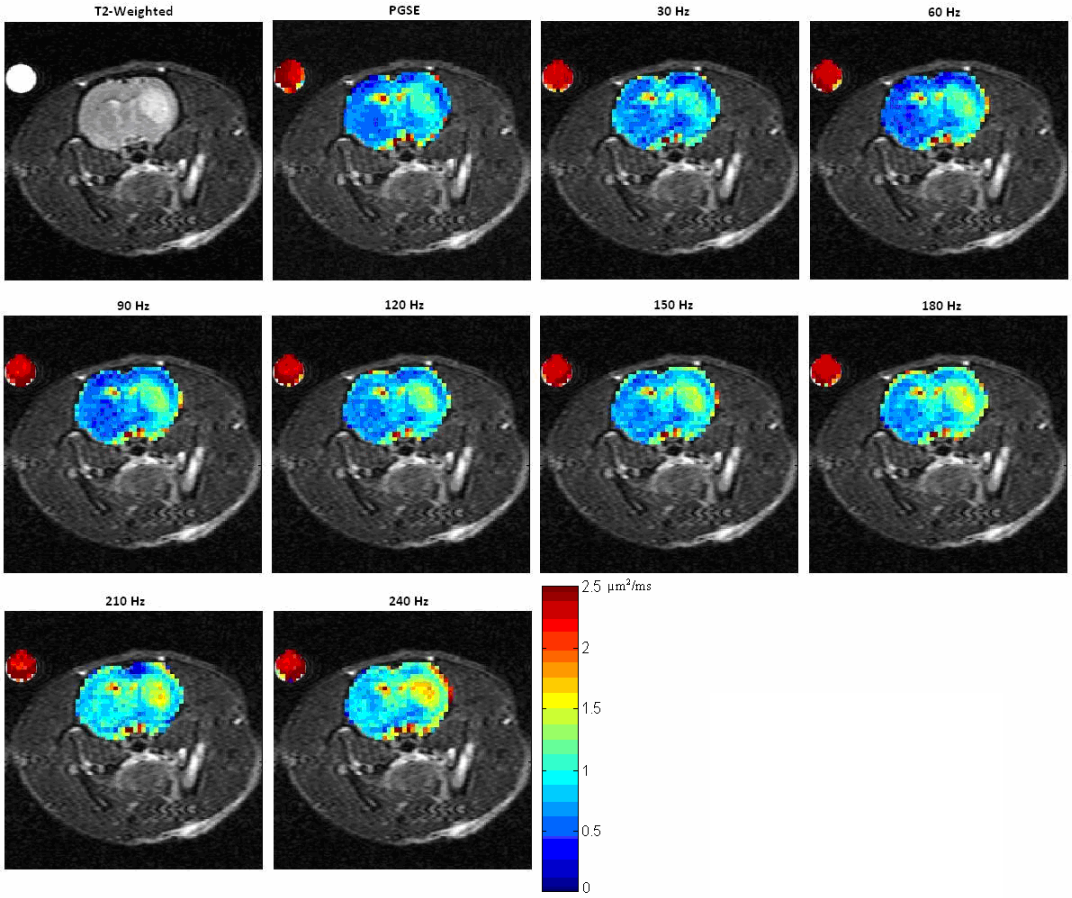

Figure 5.2. ADC maps of C6 tumors in rat brain using PGSE and OGSE methods at several frequencies.

Plots of ADC versus oscillation frequency for two regions of interest (within tumor and normal brain) from one representative animal are shown in Figure 5.3. For each frequency, the corresponding mean displacement for free diffusion predicted by Equation (5.1) is also displayed. At the lowest frequency of 30 Hz, the effective diffusion time is approximately 8.3ms (32), and the ADC is similar to

that measured by PGSE methods over an interval of 15 ms. However, as the oscillation frequency increases, and the effective diffusion time decreases, there is a clear departure in ADC from that measured with PGSE methods. For example, at an oscillation frequency of 150 Hz ($\Delta_{eff} \approx 1.7$ ms) the ADC calculated using OGSE is approximately 20% larger than that calculated using PGSE, and becomes 48% larger at 240 Hz ($\Delta_{eff} \approx 1.0$ ms).

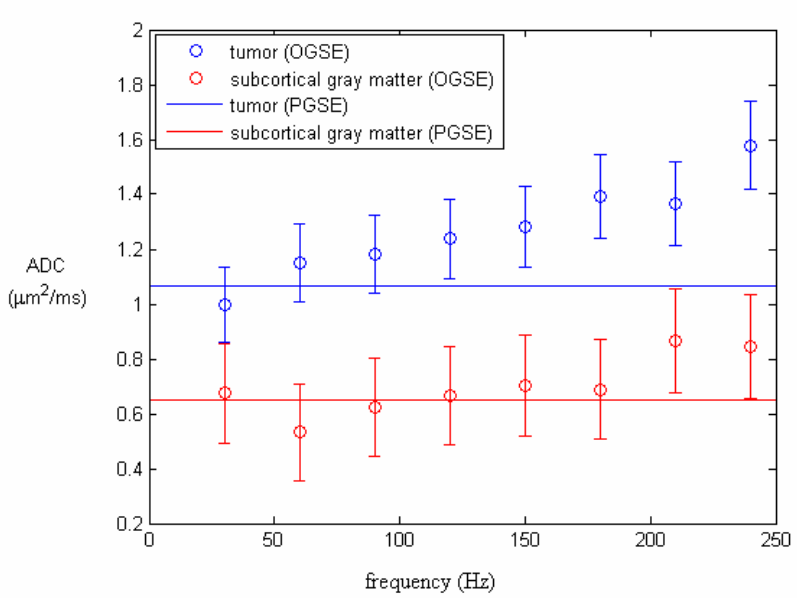

									PGSE
estimated length scale (microns)	4.1	3.1	2.6	2.3	2.1	2.0	1.8	1.8	5.5
maximum length scale (microns)	6.5	4.6	3.7	3.2	2.9	2.6	2.5	2.3	8.4

Figure 5.3. Plot of ADC vs frequency for C6 tumor and contralateral gray matter in rat brain *in vivo*

The ADC in contra-lateral grey matter was found, in general, to be smaller than that in tumor, and to increase less with frequency, with the mean value for

gray matter varying from 0.60 ± 0.06 μm^2/ms at 30 Hz to 0.79 ± 0.06 μm^2/ms at 240 Hz (errors for values averaged across all animals are reported as standard error of the mean). These values are consistent with previous reports of both human and animal brain (35-40). Although sub-cortical regions of the brain showed some increase in ADC with increasing frequency, this variation was less significant than that seen in tumor, indicating that in normal grey matter restrictions occur on even smaller scales. These differences are likely due to the densely packed layers of nerve cell bodies (neurons and glial cells) comprising the cerebral cortex compared to the morphologically multiform structure of the C6 model. The C6 glioma model is known to exhibit intra-tumor regions of necrosis and hemorrage, as well as nuclear pleomorphism, resulting in a broader range of structural components in contrast to the finely packed, granular structure of the cerebral cortex (41).

Figure 5.4 presents a further analysis of the data shown in Figure 5.2. For voxels within the tumor region of Figure 2, the ADC obtained by the PGSE

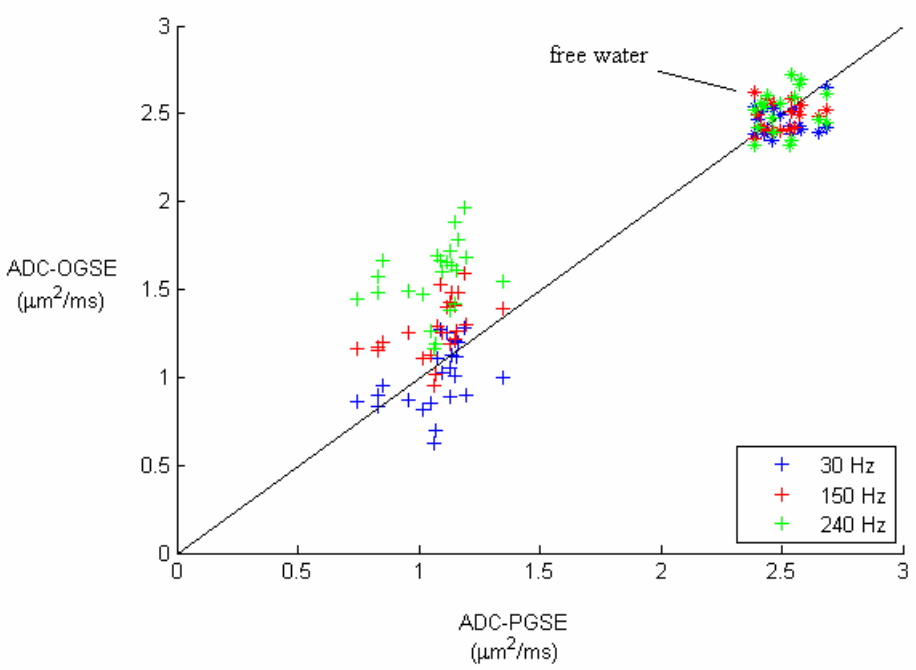

Figure 5.4. Scatter plot of ADC values obtained with OGSE and PGSE methods.

method was plotted against the values obtained by OGSE for three frequencies (30 Hz, 150 Hz, and 240 Hz). The ADC's obtained by OGSE methods are quantitatively larger than those acquired by PGSE methods, thus creating the larger contrast between tumor and healthy tissue as revealed in Figure 5.2. The results for ADCs obtained by both methods in distilled water are also shown, with the expected clustering near the line of equality.

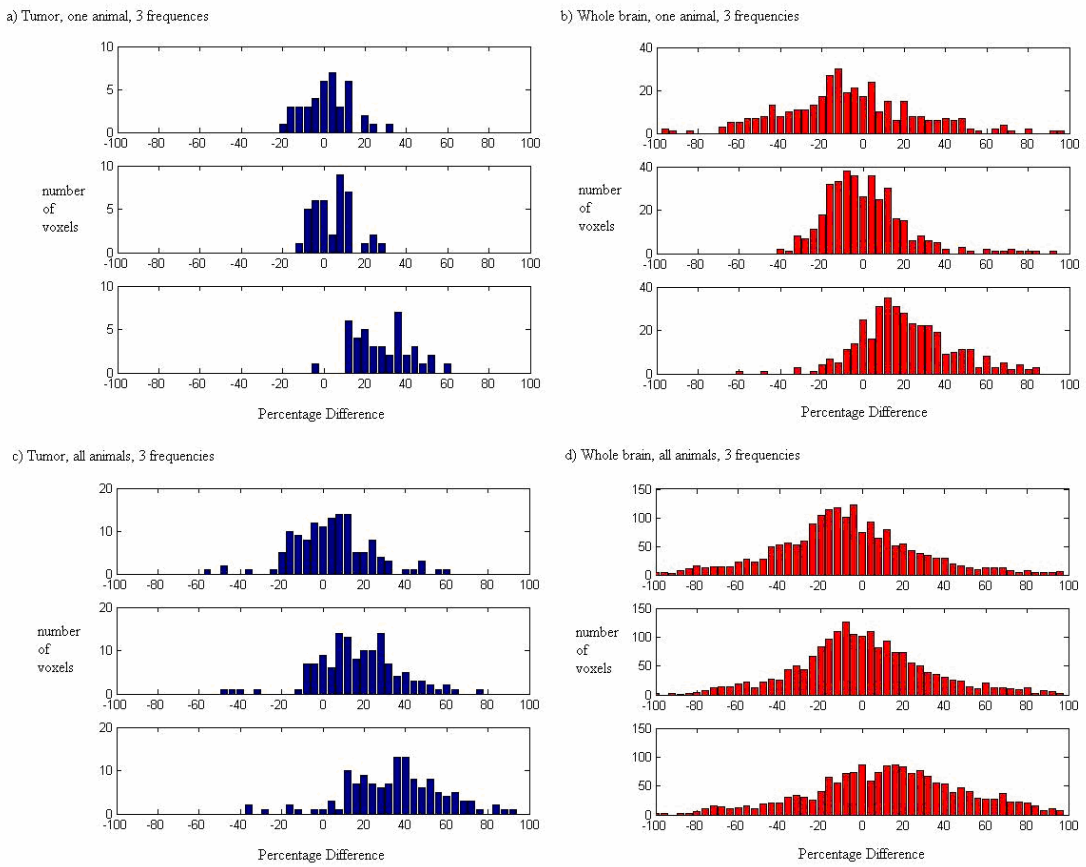

Figure 5.5. Histogram of ADC values obtained in whole tumor and whole brain regions of interest for three OGSE frequencies.

Figure 5.5 shows a histogram of the percentage difference between ADC's calculated using OGSE versus PGSE methods at the same three frequencies for voxels in both tumor and whole brain in the same animal. The percentage difference is defined as:

$$\frac{ADC_{OGSE} - ADC_{PGSE}}{ADC_{PGSE}} \times 100\%, \qquad (5.8)$$

where ADC_{PGSE} and ADC_{OGSE} are ADC values measured *via* PGSE and OGSE, respectively. Shown in these plots are the results for tumor in one animal (panel a), as well as across all 6 animals (b), and for whole brain in one animal (c), and

whole brain (d) across all 6 animals. The percentage differences are larger at higher frequencies in both tumor and whole brain.

In order to test the statistical significance of this departure, a paired Student's t-test was performed. For each animal at each oscillation frequency, the mean ADCs obtained via PGSE and OGSE for all voxels within a manually drawn region of interest, were compared. The means were statistically different ($p<0.05$) at all frequencies above 120 Hz (and $p<0.01$ at 150, 210 and 240 Hz).

An additional study was performed to examine the results at higher resolution *in vivo,* and *ex vivo* following perfusion and fixation. These results are shown in Figure 5.6. Figure 5.6 depicts a single T_2-weighted axial slice *in vivo* showing the tumor in panel (a), and the resulting ADC maps measured using PGSE and OGSE methods in panels (b) and (c) respectively. The mean ADC found in the whole tumor region of interest was 1.12 ± 0.07 $\mu m^2/ms$ using the OGSE method and 0.92 ± 0.07 $\mu m^2/ms$ for the PGSE method. For comparison, values in contra-lateral healthy sub-cortical gray matter were found to be 0.64 ± 0.09 $\mu m^2/ms$ (OGSE) and 0.54 ± 0.09 $\mu m^2/ms$ (PGSE).

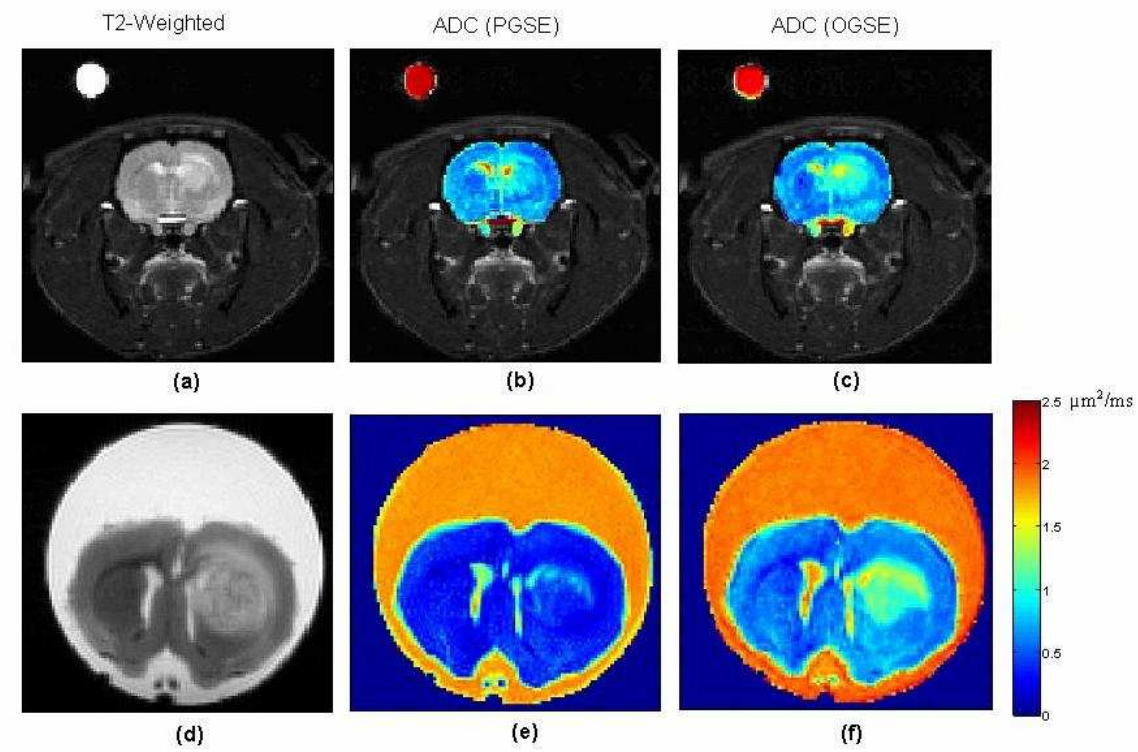

Figure 5.6. ADC maps of C6 tumor in rat brain, both *in vivo* and *ex vivo*

Four days after imaging, the brain was fixed as described in the Methods section, and imaged *ex vivo* the following day. These results are also shown in Figure 5.6, with the T_2-weighted image in panel (d), the ADC map obtained using the PGSE method in panel (e), and the ADC map obtained using the OGSE technique in panel (f). In this case, the mean ADC in tumor was found to be 1.18 ± 0.06 $\mu m^2/ms$ using the OGSE method, and 0.52 ± 0.05 $\mu m^2/ms$ using the PGSE technique, compared with sub-cortical gray matter ADCs of 0.64 ± 0.09 $\mu m^2/ms$ (OGSE) and 0.38 ± 0.08 $\mu m^2/ms$ (PGSE). Not only does the OGSE method provide quantitatively different ADCs, but also the corresponding ADC maps reveal more pronounced contrast in the tumor. Moreover, the OGSE data for both normal brain and tumor change less between the *in vivo* and *ex vivo*

conditions, possibly because the PGSE data are dominated by changes in the sizes and tortuosities of intra- and extra-cellular spaces.

Discussion

Our measurements and analysis show there were statistically significant differences in ADC obtained by OGSE methods at moderate to high frequencies (equivalent to short diffusion intervals) compared to conventional PGSE methods, and these differences varied for different tissues. The broader range of ADC values at higher frequencies produces greater contrast in the corresponding parametric ADC maps, and provides details within the tumor that would otherwise be obscured by conventional techniques. This may be of particular value for assessing the efficacy of therapeutic agents at their earliest stage, and in a noninvasive manner. While conventional imaging methods have been shown to be effective in assessing tumor cellularity and therapeutic response, their inability to identify changes in diffusion processes over intracellular spatial scales renders the information from these methods incomplete. It is reasonable to postulate that changes in the organization and integrity of intracellular spaces occur before cells undergo apoptosis or lysis. The ability to measure microscopic structural changes over previously unachievable spatial scales should therefore provide a more complete and potentially more sensitive assessment of tumor growth and response to treatment.

Using the OGSE technique, we have been able to assess water displacements over only a few microns within a tumor environment. It should be

noted that our selection of a 15 ms diffusion time for comparative PGSE experiments was very modest in comparison to those typically used in a clinical setting. In the majority of clinical studies to date, investigators routinely measure over much longer diffusion times, corresponding to displacements of tens of microns or more (22-30). Our results indicate a significant benefit in measuring water displacement over much shorter times, and thus spatial scales, as evident in the increased contrast of ADC maps..

It is widely accepted in the literature that the ADC within biological tissue is diminished from the intrinsic value of tissue water, D_0 due to the presence of barriers that restrict diffusion, such as nuclear and cellular membranes and intracellular organelles. However, while several studies have provided evidence of modest reductions in ADC at increasing diffusion times (42-45), we have shown a significant increase in ADC at decreasing diffusion times, before many of the larger scale barriers have been encountered. In several of the tumors, we were able to measure ADC values over 50% of that of free water, and with the use of even higher gradient frequencies, can expect to push this towards the limiting true intrinsic value.

In principle, shorter diffusion times can be achieved using PGSE methods, but reducing the diffusion interval Δ to values of 1 msec or below while still maintaining a large *b* value would require extremely strong gradients and power supplies that are prohibitively expensive and cumbersome. For the OGSE method in pre-clinical studies, gradients of appropriate strength are readily available for small animal MRI scanners that can achieve high gradient oscillation

frequencies over 1 kHz, with effective diffusion times down to a fraction of a millisecond. At such frequencies, OGSE methods will be capable of examining tissue microstructure over spatial scales less than a single micron, when changes in intra-cellular structure and, for example, nuclear size should become apparent. We have previously reported similar measurements in globally ischemic rat brain (40). We believe these studies will further support the claim that OGSE measurements are not only a more precise indicator of variations in tissue microstructure, but that measurements of ADC over an appropriate range of spatial scales may predict treatment response earlier than those measurements over a single length scale.

Acknowledgements

We thank the National Institutes of Health for financial support through grants RO1CA109106, RO1NS034834, U24 CA 126588, and 1K25 EB005936. We thank Mr. Jarrod True for expert animal care assistance and Mr. Richard Baheza for expert technical MRI assistance.

References

1. Moseley ME, Cohen Y, Mintorovitch J, et al. Early detection of regional cerebral-ischemia in cats – Comparison of diffusion-weighted and T_2-weighted MRI and spectroscopy. Magn Reson Med 1990;14:330-46.

2. Mintorovitch J, Mosely ME, Chileuitt L, Shimizu H, Cohen Y, Weinstein PR. Comparison of diffusion-weighted and T_2-weighted MRI for the early

detection of cerebral-ischemia and reperfusion in rats. Magn Reson Med 1991;18:39–50.

3. Righini A, Pierpaoli C, Alger JR, Di Chiro G. Brain parenchyma apparent diffusion coefficient alterations associated with experimental complex partial status epilepticus. Magn Reson Imag 1994;12:865-71.

4. Farina L, Bergqvist C, Zimmerman RA, Haselgrove J, Hunter JV, Bilaniuk LT. Acute diffusion abnormalities in the hippocampus of children with new-onset seizures: the development of mesial temporal sclerosis. Neuroradiology 2004 Apr;46:251-7.

5. Tsuruda JS, Chew WM, Moseley ME, Norman D. Diffusion-weighted MR imaging of extraaxial tumors. Magn Reson Med 1991;19:316-20.

6. Zhao M, Pipe JG, Bonnett J, Evelhoch JL. Early detection of treatment response by diffusion-weighted 1H-NMR spectroscopy in a murine tumour in vivo. Br J Cancer 1996;73:61-4.

7. Seierstad T, Folkvord S, Røe K, Flatmark K, Skretting A, Olsen DR. Early changes in apparent diffusion coefficient predict the quantitative antitumoral activity of capecitabine, oxaliplatin, and irradiation in HT29 xenografts in athymic nude mice. Neoplasia 2007 May;9:392-400.

8. McConville P, Hambardzumyan D, Moody JB, et al. Magnetic resonance imaging determination of tumor grade and early response to temozolomide in a genetically engineered mouse model of glioma. Clin Cancer Res 2007 May 15;13:2897-904.

9. Morse DL, Galons JP, Payne CM, et al. MRI-measured water mobility increases in response to chemotherapy via multiple cell-death mechanisms. NMR Biomed 2007 Jan 30;20:602-14.

10. Hayashida Y., Yakushiji T, Awai K, et al. Monitoring therapeutic responses of primary bone tumors by diffusion-weighted image: Initial results. Eur Radiol 2006 Dec;16:2637-43.

11. Theilmann RJ, Borders R, Trouard TP, et al. Changes in water mobility measured by diffusion MRI predict response of metastatic breast cancer to chemotherapy. Neoplasia 2004 Nov-Dec;6:831-7.

12. Yankeelov TE, Lepage M, Chakravarthy A, et al. Integration of quantitative DCE-MRI and ADC mapping to monitor treatment response in human breast cancer initial results. Magn Reson Imag 2007 Jan;25:1-13.

13. Dzik-Jurasz A, Domenig C, George M, et al. Diffusion MRI for prediction of response of rectal cancer to chemoradiation. Lancet 2002 Jul 27;360: 307-8.

14. Schepkin VD, Chenevert TL, Kuszpit K, et al. Sodium and proton diffusion MRI as biomarkers for early therapeutic response in subcutaneous tumors. Magn Reson Imag 2006 Apr;24:273-8.

15. Helpern JA, Ordidge RJ, Knight RA. The effect of cell membrane permeability on the apparent diffusion coefficient of water. Proceedings of the 11th Annual Meeting SMRM; 1992 Aug 8-14; Berlin, Germany. p. 1201.

16. Norris DG, Niendorf T, Leibfritz D. Health and infarcted brain tissues studied at short diffusion times: the origins of apparent restriction and the reduction in apparent diffusion coefficient. NMR Biomed 1994;7:304–10.

17. Sykova E, Svoboda J, Polak J, Chvatal A. Extracellular volume fraction and diffusion characteristics during progressive ischemia and terminalanoxia in the spinal cord of the rat. J Cereb Blood Flow Metab 1994;14: 301–11.

18. Wick M, Nagatomo Y, Prielmeier F, Frahm J. Alteration of intracellular metabolite diffusion in rat brain in vivo during ischemia and reperfusion. Stroke 1995;26:1930-3.

19. Stejskal EO, Tanner JE. Spin diffusion measurements: Spin echoes in the presence of a time-dependent field gradient. J Chem Phys 1965;42:288-92.

20. Stejskal EO. Use of spin echoes in a pulsed magnetic-field gradient to study anisotropic restricted diffusion and flow. J Chem Phys 1965;43:3597-603.

21. Callaghan PT. Principles of nuclear magnetic resonance microscopy. Oxford: Oxford University Press; 1991.

22. Ulug AM, Beauchamp N, Bryan RN, van Zijl PCM. Absolute quantitation of diffusion constants in human stroke. Stroke 1997;28:483-90.

23. Tsuruda JS, Chew WM, Moseley ME, Norman D. Diffusion-weighted MR imaging of the brain: value of differentiating between extraaxial cysts and epidermoid tumors. AJNR Am J Neuroradiol 1990 Sep-Oct;11:925-31.

24. Mardor Y, Roth Y, Lidar Z, et al. Monitoring response to convection-enhanced Taxol delivery in brain tumor patients using diffusion-weighted magnetic resonance imaging. Cancer Res 2001 July;61:4971-73.

25. Partridge SC, McKinnon GC, Henry RG, Hylton NM. Menstrual cycle variation of apparent diffusion coefficients measured in the normal breast using MRI. J Magn Reson Imag 2001;14:433-38.

26. Sinha S, Lucas-Quesada FA, Sinha U, DeBruhl N, Bassett LW. In vivo Diffusion-weighted MRI of the breast: potential for lesion characterization. J Magn Reson Imag 2002;15:693-704.

27. Mardor Y, Pfeffer R, Speigelmann R, et al. Early detection of response to radiation therapy in patients with brain malignancies using conventional and high b-value dffusion-weighted magnetic resonance imaging. Journal of Clinical Oncology 2003 March;21:1094-100.

28. Oh J, Henry RG, Pirzkall A, et al. Survival analysis in patients with glioblastoma multiforme: predictive value of choline-to-nacetylaspartate index, apparent diffusion coefficient, and relative cerebral blood volume. J Magn Reson Imag 2004;19:546-54.

29. Mardor Y, Roth Y, Ocherashvilli A, et al. Pretreatment prediction of brain tumors' response to radiation therapy using high b-value diffusion-weighted MRI. Neoplasia 2004 Mar-Apr;6:136-42.

30. Tozer DJ, Jager HR, Danchaivijitr N, et al. Apparent diffusion coefficient histograms may predict low-grade glioma subtype. NMR Biomed 2007 Feb;20:49-57.

31. Parsons EC, Does MD, Gore JC. Modified oscillating gradient pulses for direct sampling of the diffusion spectrum suitable for imaging sequences. Magn Reson Imag 2003;21:279-85.

32. Parsons EC, Does MD, Gore JC. Temporal diffusion spectroscopy: theory and implementation in restricted systems using oscillating gradients. Magn Reson Med 2006;55:75-84.

33. Barth, RF. Rat brain tumor models in experimental neuro-oncology: the 9L, C6, T9, F98, RG2 (D74), RT-2 and CNS-1 gliomas. Journal of Neuro-oncology 1998 Jan;36:91-102.

34. Neeman M, Freyer JP, Sillerud LO. A simple method for obtaining cross-term-free images for diffusion anisotropy studies in NMR microimaging. Magn Reson Med 1991 Sep;21:138-43.

35. Moseley ME, Cohen Y, Kucharczyk J, et al. Diffusion-weighted MR imaging of anisotropic water diffusion in cat central nervous system. Radiology 1990;176:439-46.

36. Tien RD, Felsberg GJ, Friedman H, Brown M, MacFall J. MR imaging of high-grade cerebral gliomas: value of diffusion-weighted echoplanar pulse sequences. Am J Roent 1994;162:671-77.

37. Le Bihan D, Turner R, Patronas N. Diffusion MR imaging in normal brain and in brain tumors. In: D. Le Bihan, editor. Diffusion and Perfusion Magnetic Resonance Imaging. New York: Raven Press; 1995. p. 134-40.

38. Bennett KM, Hyde JS, Rand SD, et al. Intravoxel distribution of DWI decay rates reveals C6 glioma invasion in rat brain. Magn Reson Med 2004;52:994-1004.

39. Ebisu T, Tanaka C, Umeda M, et al. Discrimination of brain abscess from necrotic or cystic tumors by diffusion-weighted echo planar imaging. Magn Reson Imag 1996;14:1113-16.

40. Does MD, Parsons EC, Gore JC. Oscillating gradient measurements of water diffusion in normal and globally ischemic rat brain. Magn Reson Med 2003;49:206-15.

41. Grobben B, De Deyn PP, Slegers H. Rat C6 glioma as experimental model system for the study of glioblastoma growth and invasion. Cell Tissue Res 2002;310:257-70.

42. Pfeuffer J, Flogel U, Dreher W, Leibfritz D. Restricted diffusion and exchange of intracellular water: theoretical modelling and diffusion time dependence of 1H NMR measurements on perfused glial cells. NMR Biomed 1998;11:19-31.

43. Neeman M, Jarrett KA, Sillerud LO, Freyer JP. Self-diffusion of water in multicellular spheroids measured by magnetic resonance microimaging. Cancer Res 1991;51:4072–79.

44. Latour LL, Svoboda K, Mitra PP, Sotak CH. Time dependent diffusion of water in a biological model system. Proc Natl Acad Sci USA. 1994;91**:**1229–33.

45. Helmer KG, Dardzinski BJ, Sotak CH. The application of porous-media theory to the investigation of time-dependent diffusion in *in vivo* systems. NMR Biomed 1995;8**:**297–306.

CHAPTER VI

EARLIER DETECTION OF TUMOR TREATMENT RESPONSE USING DIFFUSION WEIGHTED MAGNETIC RESONANCE IMAGING WITH OSCILLATING GRADIENTS[2]

Abstract

An improved method for detecting early changes in tumors in response to treatment, based on a modification of diffusion-weighted magnetic resonance imaging, has been demonstrated in an animal model. Early detection of therapeutic response in tumors is important both clinically and in pre-clinical assessments of novel treatments. Non-invasive imaging methods that can detect and assess tumor res[2]ponse early in the course of treatment, and before frank changes in tumor morphology are evident, are of considerable interest as potential biomarkers of treatment efficacy. Diffusion-weighted magnetic resonance imaging is sensitive to changes in water diffusion rates in tissues that result from structural variations in the local cellular environment, but conventional methods mainly reflect changes in tissue cellularity and do not convey information specific to micro-structural variations at sub-cellular scales. We implemented a modified imaging technique using oscillating gradients of the magnetic field for evaluating water diffusion rates over very short spatial scales that are more specific for detecting changes in intracellular structure that may precede changes in cellularity. Results from a study of orthotopic 9L gliomas in

[2] Submitted to *Clinical Cancer Research*, October 2009.

rat brains indicate that this method can detect changes as early as 24 hours following treatment with 1,3-bis(2-chloroethyl)-1-nitrosourea (BCNU), when conventional approaches do not find significant effects. These studies suggest that diffusion imaging using oscillating gradients may be used to obtain an earlier indication of treatment efficacy than previous magnetic resonance imaging methods.

Introduction

The early detection of the response of tumors to therapy is important both clinically and in pre-clinical assessments of novel treatments. In clinical practice, the early recognition of failure to respond to a specific treatment may allow alternative regimens to be explored and avoid unnecessary patient exposure to harmful side effects. In the evaluation of novel pharmacological therapies in pre-clinical studies, sensitive assessments of changes in tumor state, and of the time course of tumor response, are important indices of therapeutic efficacy that may affect decisions in drug development. Non-invasive imaging methods that can detect and assess tumor response early in the course of treatment, and before frank changes in tumor morphology are evident, are therefore of considerable interest as potential biomarkers of treatment efficacy. To this end, a variety of approaches using magnetic resonance imaging (MRI) have been explored, including dynamic contrast enhanced MRI (DCE-MRI) (1-4), which has proven especially useful for assessing tumor vascular properties and angiogenesis, and diffusion weighted MRI (DW-MRI) (5-8), which has been shown to be able to

monitor changes in tissue cellularity. These specialized methods complement the more standard uses of MRI as a valuable tool in cancer diagnosis and for measuring tumor size in clinical trials.

Several clinical and animal studies have confirmed the ability of conventional DW-MRI to report on changes in tumors at some time after treatment (9-14). DW-MRI relies on the phenomenon that water molecules in tissues constantly undergo random Brownian motion and diffuse from place to place at a rate that is temperature dependent. In MRI, in the presence of applied gradients of the magnetic field, this spatial migration gives rise to small changes (decreases) in the acquired MRI signals, which thus provides the basis of the contrast depicted in DW-MRI. The experimentally measured or *apparent* rate of self-diffusion of tissue water is lower in organized tissues than in free solution because various structures restrict or hinder the free movement of water. For example, cell membranes and intracellular organelles may confine and redirect the paths followed by water molecules diffusing through biological tissue, so DW-MRI methods indirectly provide information about the density of restrictive structures in the local cellular environment. The apparent diffusion coefficient (ADC) thus provides information about tissue microstructure and composition, and is reduced from the intrinsic diffusion coefficient D_0 of free water to a degree that is dependent upon the density and spacing of these restricting structures.

Cancerous tissues often show significantly different ADC values from healthy tissues, providing motivation for the use of DW-MRI techniques to study tumor proliferation and response to therapy. As tumor cells proliferate, the ADC

of water within the tumor often decreases as cell density rises, whereas after treatment the ADC often increases, presumably because of decreases in cell density consequent to apoptosis and cell death, perhaps with concomitant disruption of cell membranes. Such changes occur only after a critical time has elapsed and thus are not ideal for assessing early responses. While this increase in ADC following treatment can often be linked to a decrease in cellularity (9-14), the aggressive nature of malignant tumors necessitates a more sensitive approach for evaluating the response of cancer cells prior to such macroscopic changes. In particular, it would be of considerable interest to possess non-invasive imaging biomarkers of treatment response that are specifically sensitive to variations in *intracellular* structure that likely occur earlier in time.

Conventional MRI methods used to measure diffusion actually reflect the integrated effects of a variety of structural features including those arising at a relatively large spatial scale, on the order of a cell diameter, such as cell membranes. Many other factors may influence the free movement of water, including changes in intracellular organization and the presence of smaller scale hindrances, but their effects will be indistinguishable in the presence of restrictions occurring over larger dimensions if the measurement is made with conventional methods. This lack of specificity arises from the fact that practical diffusion measurements incorporate a particular chosen time scale, during which water diffusion effects over multiple distance scales are averaged. When this time is long, as in conventional DW-MRI, these are dominated by larger scale structures in tissues. We have therefore implemented an oscillating gradient

spin-echo (OGSE) MRI technique capable of detecting restrictions to diffusion displacements over much smaller and specific spatial scales, which can be "tuned" by choice. These may be selected to be much less than the diameter of a single cell, which results in a greater sensitivity specifically to the contributions of structures at sub-cellular scale to the measured ADC. In a previous report we illustrated the use of this method for providing greater image contrast and detecting increased structural heterogeneity in an intracranial tumor model in rats *in vivo* (15). The current study extends these techniques to the evaluation of tumor state following treatment with the commonly used chemotherapeutic drug 1,3-bis(2-chloroethyl)-1-nitrosourea (BCNU or Carmustine), in order to demonstrate the increased sensitivity for detecting early treatment responses.

Malignant gliomas are the most prevalent and lethal primary tumors of the central nervous system. Despite significant advances in surgical intervention and radio- and chemotherapeutic treatments, median survival times following diagnosis of this disease are reported to be less than one year (16-17). We chose to test the sensitivity of DW-MRI for detecting treatment effects in vivo in an animal model, a 9L glioblastoma tumor in rats. The effects of BCNU on tumor ADC values after treatment were measured using our modified and conventional DW-MRI techniques, and the potential for the new approach to serve as an earlier indicator of treatment response is demonstrated.

Materials and Methods

Animal Model

All procedures in this study were approved by Vanderbilt University's Institutional Animal Care and Usage Committee. Eighteen male Fischer 344 rats, weighing approximately 250g, were immobilized and anesthetized with a 2%/98% isoflurane/oxygen mixture and inoculated intracranially with ~10^5 9L glioblastoma cells. Eleven (N_{TX} = 11) rats were treated with BCNU as described below, and seven (N_{CON} = 7) were used as untreated, tumor-bearing controls. The tumors were allowed to develop untreated for 11-12 days. All animals were imaged immediately before and 24 hours after treatment. Five animals (3 treated, 2 controls), were sacrificed following the 24 hour post-treatment imaging session in order to obtain histology for this time point. All surviving animals (N_{TX} = 8 and N_{CON} = 5) were also imaged 72 hours post-treatment, after which they were euthanized and tissues examined histologically as described below.

Treatment protocol

BCNU, also known as Carmustine (1,3-bis(2-chloroethyl)-1-nitrosourea) is an antineoplastic chemotherapy drug used primarily in the treatment of brain tumors (18-22), as well as melanoma, Hodgkin's disease, and lung cancer (23-27). BCNU is a cell cycle-nonspecific alkylating agent which cross-links nuclear DNA, inhibiting DNA synthesis and promoting cell death.

Treatment solutions were prepared by dissolving a 13.3 mg/kg powdered dose in ethanol, and diluting with saline to achieve a 10/90% ethanol/saline solution totalling approximately 1 mL in total volume. The dose of 13.3 mg/kg has been shown in previous studies to produce an approximate 0.2 log cell kill in 9L tumors, and is equal to a 10% lethal dose (28-31). Control animals received vehicle only (1mL of 10/90% ethanol/saline). The treatment protocol consisted of a single intraperitoneal injection of BCNU (or sham) immediately following the initial imaging session (Day 0).

In vivo imaging

Approximately eleven days following tumor inoculation, MR images were obtained using a Varian 4.7T Inova imaging system (Palo Alto, CA, USA). Animals were anesthetized with a 2%/98% isoflurane/oxygen mixture, and kept at a constant body temperature of 37° C with heated air flow. A rigid bite-bar and head restraint were used to ensure proper positioning, as well as to reduce motion-induced artifacts in the image data.

Images were acquired using a quadrature 63mm inner diameter radiofrequency coil. On the initial day of imaging for each animal, a multi-slice, T2-weighted fast spin echo scan with 4 echoes (TR= 2000, 16ms echo spacing, 256x128 matrix, 48x32mm^2 FOV, 1mm slice thickness) was acquired in the coronal plane for locating the tumor region. A subsequent 2mm single axial slice (same timing parameters, but FOV = 32x32mm^2) through the central portion of the tumor was then acquired for anatomical clarification of the tumor boundary in

subsequent region-of-interest (ROI) analysis. The same slice was then imaged using our oscillating gradient spin-echo technique. For this, the pulsed linear field gradients used to induce diffusion-dependent signal losses in conventional DW-MRI are simply replaced with cosinusoidally oscillating gradients of a well defined frequency, applied in bursts of duration 33.33 ms, as described previously (15). We chose oscillation frequencies of 120 Hz and 240 Hz which are readily achievable using the standard Varian gradient coils. Diffusion-weighted scans were collected with *b*-values of 0 and 400 s/mm^2 with TR/TE = 2300/75.4ms, 64x64 matrix size, 2 mm slice thickness, 32x32mm^2 FOV. and NEX = 10. Following the OGSE imaging, conventional pulsed gradient spin echo (PGSE) diffusion-weighted images were also obtained, with the same *b*-values, with gradient duration ™ = 3 ms and diffusion interval Δ = 30 ms. An additional PGSE scan at the non-zero *b*-value was also obtained with reversed gradient polarity, and averaged with the first to eliminate the presence of gradient cross-terms in the ADC measurements (32). These cross-terms are absent in our version of the OGSE technique. In all cases, diffusion gradients were placed along all three imaging coordinate axes simultaneously to maximize the diffusion weighting with the available gradient amplitudes.

Consistent selection of the single slice imaging planes from pre- to post-treatment time points was achieved using a mutual information based rigid registration algorithm. On each day of scanning, a 3D gradient echo image dataset (TR/TE = 25/2.2 ms, FOV = 48 x 32 x 32 mm^3, matrix = 128 x 96 x 96, NEX = 8) encompassing the whole brain was collected. On Days 1 and 3

following treatment, these 3D images were co-registered to the initial 3D image collected on Day 0 in order to derive the translation and rotation matrices of the animal's position with respect to it's pre-treatment position in the laboratory reference frame. These translations and rotations were then applied to the coordinates of the single pre-treatment slice in order to obtain the same section during post-treatment imaging. Given the rigid construction of the imaging cradle and animal bite-bar, the translation and rotation of each rat brain between imaging sessions was minimal. The single slice images for each animal at all time points were then co-registered (via mutual information) following data reconstruction as well.

Perfusion fixation

Immediately following the imaging sessions at 24 or 72 hours post-treatment, several rats remained anesthetized and were anti-coagulated with 80 mg/kg pentobarbital i.p. mixed with 0.01 ml/100 g heparin. A surgical incision was then performed to allow a blunt 16 gauge perfusion needle to be inserted into the left cardiac ventricle toward the left ventricular outflow tract, and just into the aorta. A saline wash solution was then perfused, with the right atrial appendage cut immediately to allow the rapid outflow of blood and wash solution. At this time, the perfusate was switched to 10% formalin. Fixation began at a high flow rate (50 cc/min) for 2-5 minutes, then decreased to a slower rate (20 cc/min) for several minutes. The whole brain tissue was then dissected and

placed in fixative solution. Approximately 48 hours later, the fixative was removed and the brain was placed in 70% ethanol until sectioned.

Histological sectioning, staining, and analysis

Seven fixed rat brain samples treated with BCNU (five sacrificed 72 hours after treatment, two sacrificed 24 hours after treatment), as well as five fixed brain samples from controls (three from the 72 hour group, two from the 24 hour group) were prepared by the Vanderbilt University Immunohistochemistry Core for sectioning and staining. Each brain was embedded in paraffin wax and sectioned in 10 micron thick axial slices across the whole brain and through the central portion of the tumor congruent with the imaging slice. Fifteen serial slices were obtained, treated with one of three stains (H&E, Ki-67, or Casp-3) in an interleaved manner, and then mounted on glass slides for a total of five slides for each stain.

Digital images of each stained histology slide were then collected with a Zeiss Mirax Scan Digital microscope slide scanner at 40x magnification, and exported using Mirax Viewer software (Mirax, Budapest, Hungary). ImageJ software (33) was used to segment positively stained cells in the Ki-67 and Casp-3 slides by the k-means clustering algorithm (34-36), and the area fraction of positively stained cells was recorded. The Ki-67 antigen is expressed during all phases of cellular mitosis except the resting phase (G0), and thus serves as a useful marker of cell proliferation. Conversely, Casp-3 is a stain typically used to detect caspases within cells, which are essential for programmed cell death, or

apoptosis. Thus, the fraction of positively stained Ki-67 and Casp-3 cells is an indicator of the percentage of cells within a tumor that are proliferating, or dying, respectively. A comparison of the number of positively stained Ki-67 cells and Casp-3 cells between treated and untreated animals also provides information about the antineoplastic, apoptotic, and necrotic effects of the BCNU treatment.

In addition to the previously described stains, hemotoxylin and eosin (H&E) stains were also obtained to depict gross cellular morphology. This stain is particularly valuable for illustrating the boundaries between intra-nuclear, intra-cellular, and extracellular space. Hemotoxylin is a basic dye which colors basophilic structures bluish-purple, and therefore highlights regions of tissue high in nucleic acids, particularly the cell nucleus and any cytoplasmic regions dense in RNA. Eosin Y binds to eosinophilic structures, namely the intracellular proteins of the cytoplasm. We were therefore able to use the ImageJ software to calculate the relative area fractions of each space by counting the number of pixels whose data values fell into one of three data clusters using the k-means algorithm. The results of this analysis are outlined in the Results section below.

Calculation of ADC maps

ADC values were obtained by fitting the attenuated signal in each voxel, *S*, to the equation:

$$S = S_0 e^{-b \cdot ADC} \tag{6.1}$$

where S_0 is the signal in the absence of diffusion weighting, and *b* represents the amount of diffusion-weighting imparted to the sample (37). This magnitude of

this *b-value* depends on the precise nature of the applied gradients and is given by:

$$b = \gamma^2 \int_0^T dt \left[\int_0^t G_D(t')dt' \right]^2 , \qquad (6.2)$$

where $G_D(t)$ is the amplitude of the time-dependent magnetic field gradients and γ is the gyromagnetic ratio of hydrogen protons (γ = 42.58 Mhz/Tesla). Using Equation (6.2), *b-values* were calculated for the different gradient waveforms and gradient amplitudes were adjusted to match the diffusion weighting between different acquisitions as described previously (15, 38). The effective diffusion time for OGSE methods depends on the oscillation frequency. For diffusion in an unbounded medium (no restrictions), at a frequency of 240 Hz, the effective diffusion time ≈ 1 millisecond, 30 times smaller than for the PGSE measurements. (For a more complete description of these calculations, see reference 38). Note that the effective diffusion time in OGSE depends on the oscillation period only, and is no longer determined by the time between gradient pulses.

All data were analyzed using Matlab 2009a (The Mathworks, Natick, MA, USA). Whole tumor regions of interest were drawn and segmented with reference to high-resolution T_2-weighted scans, and may have included additional voxels on Day 1 and Day 3 following treatment (or sham) due to increased tumor volume at these imaging time points. Statistical analyses (t-tests) comparing the ADC measurements, as well as histological data, were used to determine the significance of the results reported below.

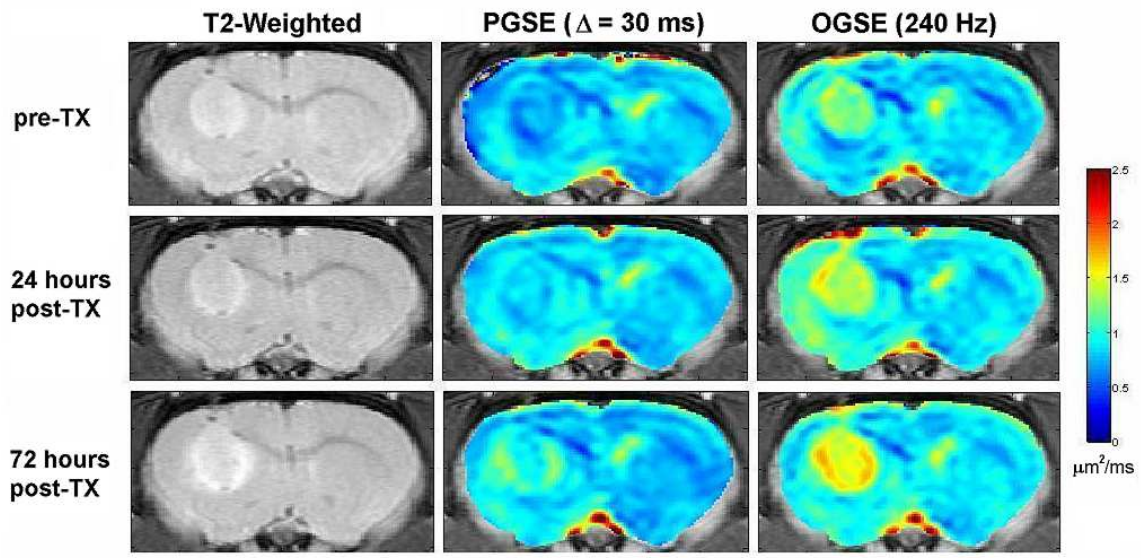

Figure 6.1. Representative ADC maps of 9L tumor in rat brain in vivo with PGSE and OGSE methods, 24 and 72 hours after treatment with BCNU.

Figure 6.1 shows representative ADC maps obtained with OGSE and PGSE methods for one animal treated with BCNU. These images demonstrate the broader range of ADC values and heterogeneous tissue details obtainable with OGSE methods. They also indicate that OGSE methods are more sensitive for depicting the structural variations that accompany chemotherapeutic treatment. While the conventional (PGSE) images show a slight increase in ADC following treatment, the OGSE techniques show larger changes at early time points. This is consistent with our prediction that OGSE methods may detect changes in tissue structure occurring on an intracellular scale, before gross changes in cell density.

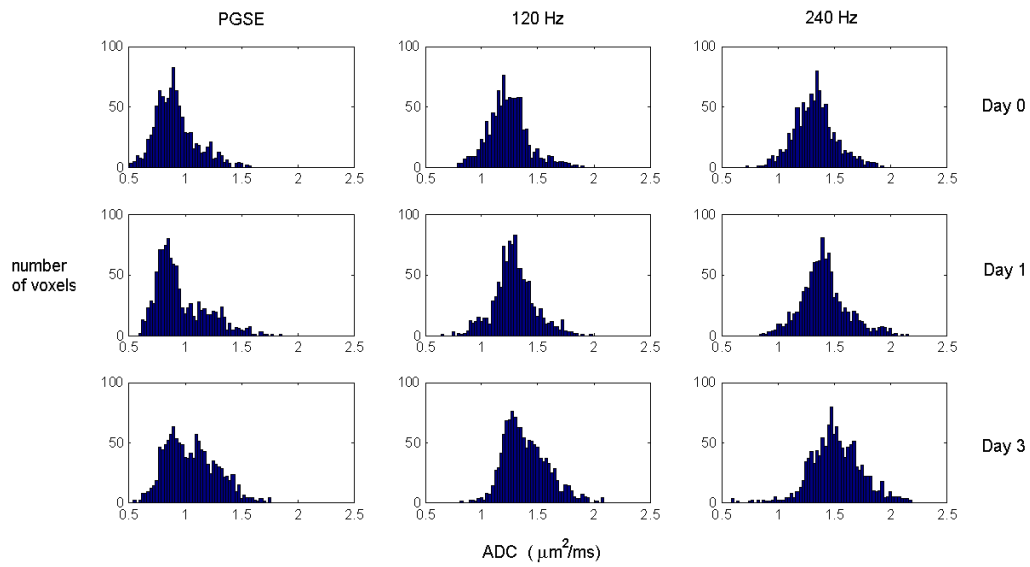

Figure 6.2. Histogram of ADC values obtained in whole tumor region of interest in one representative animal following treatment with BCNU.

Histograms of ADC values within a whole tumor region of interest (for the animal shown in Fig 1) are plotted in Figure 6.2. These plots reveal the range of ADCs measured with each technique, as well as the increase in mean ADC as a function of treatment. Note that the maximum ADC values measured by PGSE are still much lower than the value for free water, suggesting all the water is still hindered at a long distance (time) scale, whereas the OGSE data at 240 Hz after treatment show a number of voxels have ADC values approaching that of free water, suggesting a reduction in structures that hinder diffusion at this shorter time scale. These results are further illustrated in Figure 6.3, which shows the relationship between pre- vs post-treatment ADCs for all voxels within the tumor. There is clearly an increase in ADC measured with both techniques 24 hours following treatment. The range of ADC values broadens after 72 hours,

indicating a greater range in the size of restrictive structures present in the cellular environment.

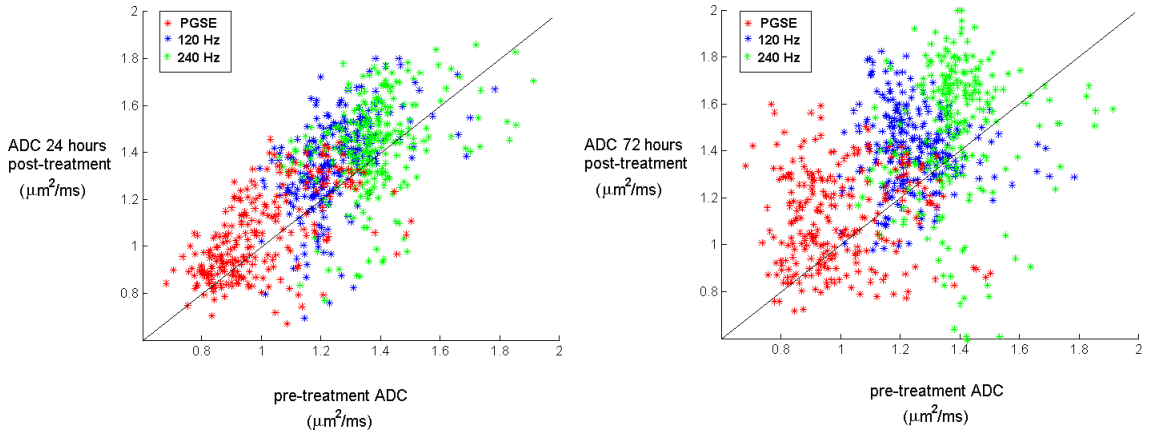

Figure 6.3. Scatter plot of ADC values obtained with PGSE and OGSE methods in whole tumor region of interest for one animals treated with BCNU.

Figure 6.4 shows the mean ADC across all animals at all three imaging time points, using OGSE and PGSE methods. Note that ADC values shown here are the mean values across the entire tumor, and greater differences in OGSE ADCs pre- and post-treatment are present in many voxels (as indicated in Figure 6.1). The control group showed no significant changes in ADC at all imaging time points, for all methods. The ADC of the treated animals, however, clearly increases with time after treatment. After 24 hours, the ADC increased from 1.16 $\pm$ 0.10 μm^2/ms to 1.19 $\pm$ 0.12 μm^2/ms at 120 Hz, an approximately 2.5% change, while it increased by approximately 4% at 240 Hz, from 1.27 $\pm$ 0.11 μm^2/ms to 1.33 $\pm$ 0.12 μm^2/ms. At the same time point, there was an approximate 1.5% increase with PGSE methods, from 0.855 $\pm$ 0.12 μm^2/ms to 0.869 $\pm$ 0.13 μm^2/ms. At 24 hours, paired student t-tests showed the changes measured by OGSE

techniques to be significant at the α = 0.05 level, with p = 0.04 and p = 0.024, at 120 Hz and 240 Hz respectively, but not significant for PGSE (p = 0.13).

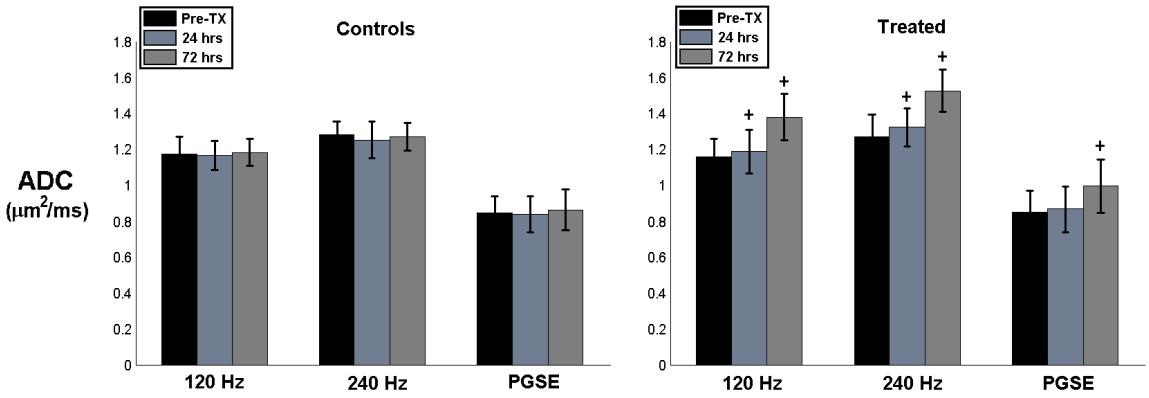

Figure 6.4. Plot of mean ADC values for all animals, both treated and controls, at both oscillation frequencies and with PGSE methods. A '+' above data points indicates statistical significance.

After 72 hours, both imaging methods revealed statistically significant increases in ADC, increasing by approximately 18% (120 Hz) and 20% (240 Hz) from their pre-treatment values, as measured with OGSE, and by approximately 16% with PGSE. Statistical measures of significance gave p-values, at 72 hours, of p = 0.009 (120 Hz), p = 0.003 (240 Hz), and p = 0.018 (PGSE). Statistical analyses of the control animals gave p-values greater than p > 0.05 in all cases.

Histological Results

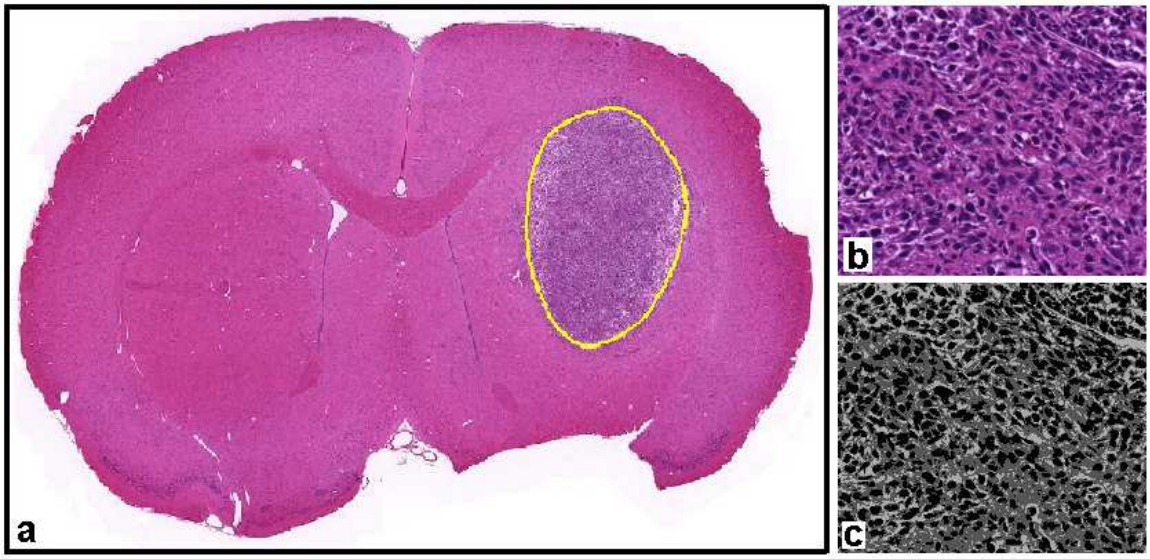

Figure 6.5. Example of H&E stained histological section of rat brain bearing a 9L tumor, along with a close-up of the tumor region and the results of k-means clustering segmentation.

As previously described, a k-means clustering algorithm (ImageJ) was used for segmentation of whole tumor regions of interest from histological image data. Mean area fractions of positively stained cells in Ki-67 and Casp-3 marked slides were recorded for both treated and control animals. Area fractions of hemotoxylin-stained, eosin-stained, and unstained portions of the H&E slides, for both groups, were also recorded. An example is shown in Figure 6.5. Statistical measures of significance were performed in Matlab 2009a using unpaired student t-tests at a significance level of $\alpha = 0.05$.

Twenty-four hours after treatment or sham, there was no significant difference in the area fraction of positively stained Casp-3 (apoptic) cells between groups ($p = 0.54$). Mean area fraction for the control group was $2.13 \pm 0.65\%$,

compared to 2.42 ± 0.84% for the treated group. However, 72 hours after treatment, the mean area fraction of apoptotic cells in the treated group rose to 2.89 ± 1.37%, while the control group stayed nearly the same at 2.17 ± 1.45%. However, again this increase was not statistically significant at the α = 0.05 level (p = 0.09).

The area fraction of positively stained Ki-67 (proliferating) cells 24 hours after treatment was not significantly different among groups (p = 0.20), with mean values for treated and controls, respectively, of 19.75 ± 1.36% and 17.95 ± 2.43%. Seventy-two hours after treatment, however, the percentage for the treated group fell to 16.09 ± 1.6%, while the control group rose to 19.05 ± 1.71% (p = 0.004). These results indicate that the antineoplastic effects of BCNU decreased the number of proliferating cells in treated animals, while the control animals experienced increasing tumor growth.

There was also a significant increase in extracellular space for both treated and untreated animals from the 24 hour to 72 hour timepoint. At 24 hours, the mean area fraction of the extracellular space for the treated group was 9.74 ± 1.57%, compared to 9.20 ± 1.82% for the control group. This difference was insignificant (p = 0.38). However, after 72 hours, this number increased to 16.2 ± 2.49% for the treated group and 13.55 ± 1.79% for the controls, a statistically significant result, with p = 0.046.

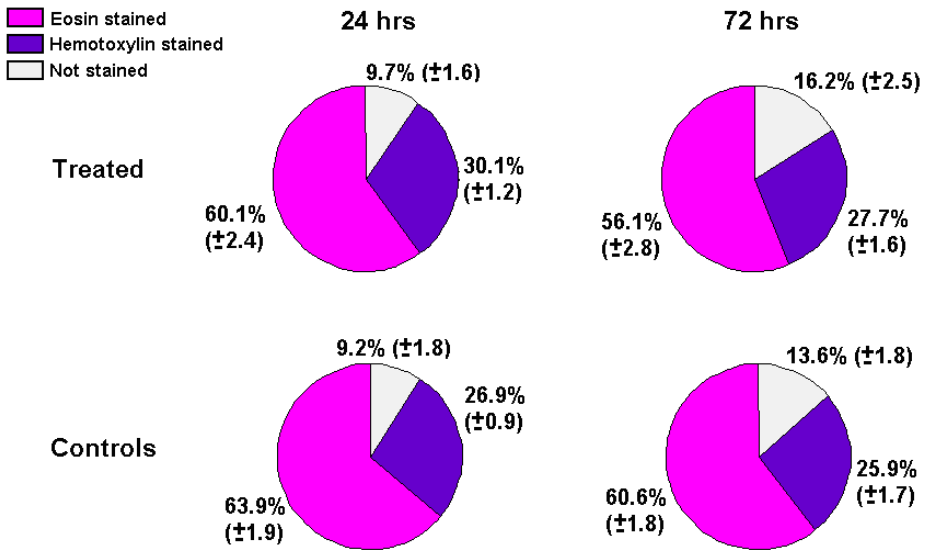

Figure 6.6. Pie charts demonstrating the relative area fractions of histological tissue stained with eosin, hemotoxylin, or no stain, in both treated animals and controls.

Finally, it was also determined that the hemotoxylin stained portion of the tissue sections was significantly different between the two groups, at both 24 hours and 72 hours following treatment. Twenty-fours following treatment, the area fraction for the treated group was 30.14 ± 1.15% compared to 26.87 ± 0.94% for the controls ($p = 0.002$), while after 72 hours, these numbers were 27.68 ± 1.61% for the treated animals and 25.86 ± 1.65% for the controls ($p = 0.02$). See Figure 6. These results may be consistent with increasing evidence that alkylating agents produce a form of programmed necrosis in tumor cells, with distinct morphological features differing from those induced by apoptosis (39-42).

Finally, we also measured the mean particle size for the hemotoxylin stained sections, as well as the nuclear/intracellular ratio, found by considering the hemotoxylin/eosin fraction. Although hemotoxylin does not solely stain the nucleus (it stains all nucleic acids, so it also attaches to cytoplasmic RNA), the

vast majority of this stain is intranuclear. The mean nuclear size (in square microns) of hemotoxylin stained regions were significantly larger in treated animals than controls. Twenty-four hours after treatment, the mean nuclear area was found to be $37.31 \pm 3.29\ \mu m^2$ in controls, compared to $39.98 \pm 2.49\ \mu m^2$ for treated animals ($p = 0.029$). After 72 hours, the mean nuclear size of the control group fell to $34.88 \pm 3.55\ \mu m^2$ for controls, while the treated group changed very little, with a mean of $39.26 \pm 2.12\ \mu m^2$ ($p = 0.047$).

The ratio of hemotoxylin to eosin stained area fractions showed statistical differences as well. For the control group, the ratio of the area fraction of hemotoxylin to eosin stained tissue was $42.06 \pm 1.93\%$, compared to $50.28 \pm 3.73\%$ for the treated animals, after 24 hours ($p = 0.012$). Seventy-two hours after treatment, controls showed a $42.71 \pm 1.94\%$ ratio, while the treated group was again only reduced slightly, to $49.49 \pm 4.77\%$ ($p = 0.008$).

Discussion

Our measurements and analysis reveal that OGSE techniques at moderately high frequencies may provide an earlier and more sensitive indicator of tumor treatment response than conventional, pulsed-gradient (PGSE) methods. The broader range of ADC values obtained with OGSE techniques provide greater contrast in corresponding ADC maps, and therefore reveal details of tissue microstructure obscured by conventional means. While PGSE methods have been shown to be sensitive to changes in tumor cellularity resulting from treatment response, their inability to measure diffusion processes

on an intracellular scale renders these methods less sensitive to microstructural variations that may precede changes in cellularity. Therefore, these results may be of particular interest for assessing the efficacy of therapeutic agents noninvasively, prior to changes in tumor size.

The difference in the mean ADCs measured by PGSE and OGSE methods implies that there is a significant difference in the number of restrictions encountered by water molecules during these two types of experiments. Given the relatively long diffusion time used in PGSE studies (here, 30 ms), an unrestricted water molecule would travel approximately 12 microns in that time, a distance comparable to a cell diameter. Since the ADC of water measured with PGSE methods in this study was far less than that of free water (~2.5 μm^2/ms at body temperature), this indicates that restrictions are occurring on scales smaller than 12 microns. However, given that an unrestricted water molecule would only move approximately 2 microns during the one millisecond effective diffusion time of the 240 Hz OGSE measurement, the much higher ADC in this case indicates much less restriction at the 2 micron spatial scale. It will therefore be of interest to measure biological samples at different and shorter effective diffusion times in order to glean information about the range of restrictions occurring in the intracellular environment.

These studies have shown that OGSE methods are capable of revealing significant differences in tumor ADC only 24 hours after treatment with an anti-neoplastic chemotherapeutic agent, whereas PGSE techniques showed no such effect. At 24 hours, the fraction of proliferating and/or apoptic cells as well as the

total fraction of extracellular space were not significantly different in treated vs control tumors,, as evidenced by quantitative histological analysis. These results appear to indicate that the significant differences in ADC measured by OGSE techniques arise from variations in intracellular structure preceding changes in cellularity. While PGSE measurements were capable of revealing such differences after 72 hours, these methods were incapable of resolving differences at an earlier time point.

Recent evidence suggests that nuclear volume may play a significant role in cancer diagnosis, as well as prognosis following treatment (43-45). Xu, et al, (46) recently reported the results of numerical simulations of the effects that differences in the nuclear/cytoplasmic volume ratio of cells would have on ADC measurements. This study reported that OGSE methods might reveal differences in ADC as large as 15% at oscillation frequencies up to 1 kHz, for two tissues with the same cell density but nuclear/cytoplasmic volume ratios of 6.2% and 22%, while PGSE showed little difference over a broad range of diffusion times (< 3.6%). We report here an approximate 4% increase in ADC using OGSE methods 24 hours following treatment, compared to approximately 1.5% with PGSE. While these differences are smaller than those reported by Xu. et al., our experiments were performed at much lower oscillation frequencies (120 Hz and 240 Hz), with smaller differences in the mean nuclear/cytoplasmic ratios between groups. Given the insignificant difference in extracellular space found between treated and control animals after 24 hours, indicating little to no difference in cellularity, these results indicate that OGSE methods may be capable of

detecting changes in ADC that result from chemotherapeutic effects on intracellular structure, such as nuclear volume.

While previous studies implementing OGSE methods in ischemic rat brain (47) and intracranial C6 tumors (15) were effective in their ability to measure ADC at diffusion times at, or below, a single millisecond, we report here the first results of these techniques in a model of tumor treatment response. Furthermore, while this study utilized only two gradient oscillation frequencies, with a maximum at 240 Hz, the availability of higher gradient amplitudes will allow such techniques to be pushed to higher oscillation frequencies, resulting in even shorter effective diffusion times. At such frequencies, we will be able to probe variations in tissue microstructure occurring on a submicron scale, which may provide an even more sensitive measure of the effects of chemotherapeutic agents on tumor microstructure *in vivo.*

Acknowledgements

We thank the National Institutes of Health for financial support through grants RO1CA109106, RO1NS034834, U24 CA 126588, and 1K25 EB005936. We also thank the Vanderbilt University Immunohistochemistry Core for assistance in histological sectioning and staining, as well as the Vanderbilt Center for Mass Spectrometry (directed by Dr Richard Caprioli) for assistance with digital imaging of histological data. Additionaly, we thank Mr. Jarrod True for assistance with animal care protocols.

References

1. Choyke PL, Dwyer JA, Knopp VM. Functional tumor imaging with dynamic contrast-enhanced magnetic resonance imaging. J Magn Reson Imaging 2003; 17:509-20.

2. Jordan BF, Runquist M, Raghunand N, et al. Dynamic contrast-enhanced and diffusion MRI show rapid and dramatic changes in tumor microenvironment in response to inhibition of HIF-1alpha using PX-478. Neoplasia 2005 May; 7:475-85.

3. Padhani AR, Leach MO. Antivascular cancer treatments: functional assessments by dynamic contrast-enhanced magnetic resonance imaging. Abdom Imaging 2005;30:324-42.

4. Yankeelov TE, Lepage M, Chakravarthy A, et al. Integration of quantitative DCE-MRI and ADC mapping to monitor treatment response in human breast cancer initial results. Magn Reson Imag 2007 Jan;25:1-13.

5. Sugahara T, Korogi Y, Kochi M, et al. Usefulness of diffusion-weighted MRI with echo-planar technique in the evaluation of cellularity in gliomas. J Magn Reson Imaging 1999 Jan;9:53-60.

6. Lyng H, Haraldseth O, Rafstad EK. Measurement of cell density and necrotic fraction in human melanoma xenografts by diffusion weighted magnetic resonance imaging. Magn Reson Med 2000;43:828-36.

7. Sinha S, Lucas-Quesada FA, Sinha U, DeBruhl N, Bassett LW. In vivo diffusion-weighted MRI of the breast: potential for lesion characterization. J Magn Reson Imaging 2002 Jun;15:693-704.

8. Humphries PD, Sebire NJ, Siegel MJ, Olsen ØE. Tumors in pediatric patients at diffusion-weighted MR imaging: apparent diffusion coefficient and tumor cellularity. Radiology 2007 Dec;245:848-54.

9. Zhao M, Pipe JG, Bonnett J, Evelhoch JL. Early detection of treatment response by diffusion-weighted 1H-NMR spectroscopy in a murine tumour in vivo. Br J Cancer 1996;73:61-4.

10. Seierstad T, Folkvord S, Røe K, Flatmark K, Skretting A, Olsen DR. Early changes in apparent diffusion coefficient predict the quantitative antitumoral activity of capecitabine, oxaliplatin, and irradiation in HT29 xenografts in athymic nude mice. Neoplasia 2007 May;9:392-400.

11. McConville P, Hambardzumyan D, Moody JB, et al. Magnetic resonance imaging determination of tumor grade and early response to temozolomide in a genetically engineered mouse model of glioma. Clin Cancer Res 2007 May 15;13:2897-904.

12. Morse DL, Galons JP, Payne CM, et al. MRI-measured water mobility increases in response to chemotherapy via multiple cell-death mechanisms. NMR Biomed 2007 Jan 30;20:602-14.

13. Theilmann RJ, Borders R, Trouard TP, et al. Changes in water mobility measured by diffusion MRI predict response of metastatic breast cancer to chemotherapy. Neoplasia 2004 Nov-Dec;6:831-7.

14. Schepkin VD, Chenevert TL, Kuszpit K, et al. Sodium and proton diffusion MRI as biomarkers for early therapeutic response in subcutaneous tumors. Magn Reson Imag 2006 Apr;24:273-8.

15. Colvin DC, Yankeelov TE, Does MD, Yue Z, Quarles C, Gore JC. New insights into tumor microstructure using temporal diffusion spectroscopy. Cancer Res 2008 July;68:5941-5947.

16. Laws ER, Parney IF, Huang W. Survival following surgery and prognostic factors for recently diagnosed malignant glioma: data from the Gliomas Outcome Project. J Neurosurg 2003 Sep;99:467-73.

17. Stupp R, Mason WP, van den Bent MJ, et al. Radiotherapy plus concomitant and adjuvant temozolomide for glioblastoma. N Engl J Med 2005 Mar;352:987-96.

18. Barker M, Hoshino T, Gurcay O, et al. Development of an Animal Brain Tumor Model and Its Response to Therapy with 1,3-Bis(2-chloroethyl)-1-nitrosourea. Cancer Res 1973 May;33:976-86.

19. Walker MD, Alexander E, Hunt WE, et al. Evaluation of BCNU and/or radiotherapy in the treatment of anaplastic gliomas. A cooperative clinical trial. J Neurosurg 1978 Sep;49:333:43.

20. Buckner JC, Brown LD, Kugler JW, et al. Phase II evaluation of recombinant interferon alpha and BCNU in recurrent glioma. J Neurosurg 1995 Mar;82:430-5.

21. Westphal M, Hilt DC, Bortey E, et al. A phase 3 trial of local chemotherapy with biodegradable carmustine (BCNU) wafers (Gliadel wafers) in patients with primary malignant glioma. Neuro-oncol 2003;5:79-88.

22. Fine HA, Wen PY, Maher EA, et al. Phase II Trial of Thalidomide and Carmustine for Patients With Recurrent High-Grade Gliomas. J Clin Oncol 2003;21:2299-2304.

23. Feun LG, Savaraj N, Moffat F, et al. Phase II trial of recombinant interferon-alpha with BCNU, cisplatin, DTIC and tamoxifen in advanced malignant melanoma. Melanoma Res 1995 Aug;5:273-6.

24. Phillips GL, Fay JW, Herzig GP, et al. Intensive 1,3-bis(2-chloroethyl)-1-nitrosourea (BCNU), NSC #4366650 and cryopreserved autologous marrow transplantation for refractory cancer. A phase I-II study. Cancer 1983 Nov;52:1792-802.

25. Tchekmedyian NS, Tait N, Van Echo D, Aisner J. High-dose chemotherapy without autologous bone marrow transplantation in melanoma. J Clin Oncol 1986 Dec;4:1811-8.

26. Elias AD, Ayash L, Frei E, Intensive combined modality therapy for limited-stage small-cell lung cancer. JNCI J Natl Cancer Inst 1993;85:559-66.

27. Turrisi AT, Sherman CA. The treatment of limited small cell lung cancer: a report of the progress made and future prospects. Eur J Cancer 2002;38:279-91.

28. Rosenblum ML, Wheeler KT, Wilson CB, Barker M, Knebel KD. In Vitro Evaluation of in Vivo Brain Tumor Chemotherapy with 1,3-Bis(2-chloroethyl)-nitrosourea. Cancer Res 1975 Jun;35:1387-91.

29. Rosenblum ML, Knebel KD, Vasquez DA, Wilson CB. In Vivo Clonogenic Tumor Cell Kinetics following 1,3-Bis(2-chloroethyl)-1-Nitrosourea Brain Tumor Therapy. Cancer Res 1976 Oct;36:2718-25.

30. Kim B, Chenevert TL, Ross BD. Growth kinetics and treatment response of the intracerebral rat 9L brain tumor model: a quantitative *in vivo* study using magnetic resonance imaging. Clin Cancer Res 1995 June;1:643-50.

31. Ross BD, Zhao YJ, Neal ER, et al. Contributions of cell kill and posttreatment tumor growth rates to the repopulation of intracerebral 9L tumors after chemotherapy: an MRI study. Proc Natl Acad Sci USA 1998 Jun;95:7012-7.

32. Neeman M, Freyer JP, Sillerud LO. A simple method for obtaining cross-term-free images for diffusion anisotropy studies in NMR microimaging. Magn Reson Med 1991 Sep;21:138-43.

33. Rasband WS. ImageJ, U.S. National Institutes of Health, Bethesday, Maryland, USA, http://rsb.info.nih.gov/ij, 1997-2005.

34. Taxt T, Lundervold A, Fuglaas B, Lien H, Abeler V. Multispectral analysis of uterine corpus tumors in magnetic resonance imaging. Magn Reson Med 1992;23:55-76.

35. Pham DL, Chenyang X, Prince JL. Current methods in medical image segmentation. Annu Rev Biomed Eng 2000;2:315-37.

36. Gurcan MN, Sahiner B, Petrick N, et al. Lung nodule detection on thoracic computed tomography images: Preliminary evaluation of a computer-aided diagnosis system. Med Phys 2002 Nov;29:2552-8.

37. Stejskal EO, Tanner JE. Spin diffusion measurements: Spin echoes in the presence of a time-dependent field gradient. J Chem Phys 1965;42:288-92.

38. Parsons EC, Does MD, Gore JC. Modified oscillating gradient pulses for direct sampling of the diffusion spectrum suitable for imaging sequences. Magn Reson Imag 2003;21:279-85.

39. Zong WX, Ditsworth D, Bauer DE, Wang ZQ, Thompson CB. Alkylating DNA damage stimulates regulated form of necrotic cell death. Gen Dev 2004;18:1272-82.

40. Guerriero JL, Ditsworth D, Fan Y, Zhao F, Crawford HC, Zong WX. Chemotherapy induces tumor clearance independent of apoptosis. Cancer Res 2008 Dec;68:9595-600.

41. Corcoran GB, Sidhartha DR. The role of the nucleus and other compartments in toxic cell death produced by alkylating hepatotoxicants. Toxicol Appl Pharmacol 1992;113:167-83.

42. Casiano CA, Ochs RL, Tan EM. Distinct cleavage products of nuclear proteins in apoptosis and necrosis revealed by autoantibody probes. Cell Death Differ 1998;5:183-90.

43. Arima K, Sugimura Y, Hioki T, Yamashita A, Kawamura J. Stereologically estimated mean nuclear volume of prostate cancer is a reliable prognostic parameter. Brit J Cancer 1997;76:234-237.

44. Hsu CY, Kurman RJ, Vang R, Wang TL, Baak J, Shih Ie M. Nuclear size distinguishes low- from high-grade ovarian serous carcinoma and predicts outcome. Hum Pathol 2005;36:1049–1054.

45. Zink D, Fischer AH, Nickerson JA. Nuclear structure in cancer cells. Nat Rev Cancer 2004;4:677–687.

46. Xu J, Does MD, Gore JC. Sensitivity of MR diffusion measurements to variations in intracellular structure: effects of nuclear size. Magn Reson Med 2009;61:828-33.

47. Does MD, Parsons EC, Gore JC. Oscillating gradient measurements of water diffusion in normal and globally ischemic rat brain. Magn Reson Med 2003;49:206-15

CHAPTER VII

CONCLUSION

Summary

The research reported in this dissertation has focused on the utility of temporal diffusion magnetic resonance spectroscopy techniques in evaluating biological tissue morphology. In contrast to conventional diffusion-weighted MRI techniques, which probe molecular displacements over an experimentally determined 'diffusion time', these methods isolate specific frequencies of the diffusion spectrum through appropriately modulated, oscillating magnetic field gradients. A thorough description of the diffusion spectrum and its connection to the molecular velocity auto-correlation function was outlined in Chapter III, along with the experimental techniques for quantifying the apparent diffusion coefficient as a function of oscillation frequency.

Chapter IV demonstrated the application of these oscillating gradient spin-echo methods for quantifying molecular water diffusion in a system of cultured human embronic kidney cells (293-EBNA). The ADC was measured with OGSE techniques at ten equally spaced frequencies between 200 Hz and 2000 Hz following actin/cytoskeleton depolymerization, microtubule depolymerization, and disruption of the intracellular Golgi apparatus, as well in control cells treated with PBS. Conventional, pulsed-gradient diffusion-weighted data, at a diffusion time of 30 ms, were also obtained. While the disruption of the Golgi apparatus with

Brefeldin A showed no effect on ADC compared to control cells, the disruption of the microtubule network with Nocodazole created a slight decrease in ADC at frequencies above 1 kHz. While the ADC decreased a maximum of approximately 2% at 2 kHz, a difference that was found to be insignificant compared to control values using a student t-test, the increasing divergence of ADC, between treated samples and controls, with increasing oscillation frequency suggests that a more pronounced effect may be detectable at higher frequencies. While this last statement is only speculative, it would imply that microtubules only have an effect on ADC values at very short diffusion times, and that microtubules play little or no role in the large ADC decreases measured in stroke at long diffusion times.

The third drug used in these packed cell studies, Cytochalasin D, did produce a significant difference in ADC values following treatment. This drug, which depolymerizes the actin cytoskeleton and inhibits cytoplasmic streaming, showed a similar divergence in ADC values, as compared to controls, with increasing oscillation frequency. These differences were found to be significant at 1.8 kHz ($p = 0.05$) and 2 kHz ($p = 0.04$), while ADC values measured with PGSE were found to be nearly identical ($p = 0.84$) between treated and control groups. While the disassociation of actin filaments in the intracellular environment would seemingly provide less barriers to diffusion and thereby increase ADC, these findings suggest that the cytoplasmic streaming perpetuated by the actin cytoskeleton may play a significant role in intracellular ADC at very short diffusion times. However, at longer diffusion times commonly implemented with PGSE

techniques, the reduction in ADC from free water values is dominated by the presence of other restrictions, such as those created by the presence of intracellular organelles. Experiments performed in samples of BSA validated this claim by showing that, although both methods showed a significant decrease in ADC with increasing protein content in BSA, only OGSE methods were capable of detecting viscous effects produced by actin disassociation in a structured cell system, implying that any such influence these effects have on PGSE measurements are obscured by other restriction effects.

Chapter V outlined the use of OGSE techniques for evaluating water diffusion rates in C6 tumors. To the best of our knowledge, these studies are the first reported application of OGSE methods to the study of cancer, and demonstrate the shortest diffusion times ever measured in a model of cancer *in vivo*. The results of this study were published in the journal *Cancer Research* in July 2008 (volume 68, pages 5941-47). These experiments showed that OGSE methods could provide additional information about tumor microstructure obscured by conventional PGSE techniques by measuring ADC over much shorter diffusion times, thereby providing greater sensitivity to variations in tissue structure on an intracellular scale. The resulting ADC maps of intracranial tumor, over a broad range of oscillation frequencies (30 Hz to 240 Hz), produced greater tissue contrast and revealed greater detail of tissue heterogeneity than ADC maps produced by PGSE. These findings suggested that OGSE methods may not only provide a more sensitive probe of tissue microstructure *in vivo*, but may

also serve as an earlier and/or more accurate biomarker of tumor treatment response.

Chapter VI is the realization of OGSE methods as a biomarker of treatment response. Following upon the work outlined in Chapter V, OGSE techniques were again implemented in the study of an intracranial tumor in rats *in vivo*. However, the purpose of this latter study was to evaluate the efficacy of OGSE methods for detecting tumor treatment response earlier than conventional PGSE techniques. Studies were performed in male Fischer 344 rats bearing intracranial 9L gliomas, prior to, as well as 24 and 72 hours following treatment with a common antineoplastic chemotherapy drug, Carmustine. Experiments were also performed in control animals. Animals from both groups were then sacrificed for tissue sectioning and stained with histological markers (caspase-3, Ki-67, and hemotoxylin and eosin). Tissue sections were digitally imaged and area fractions of histologically stained regions were quantified using a k-means clustering algorithm.

These studies revealed that OGSE methods were capable of detecting variations in tumor ADC in as little as 24 hours following treatment, when PGSE methods failed to detect such changes. Variations in ADC measured at both 120 Hz and 240 Hz were found to be significantly lower than pre-treatment values 24 hours following treatment ($p = 0.04$ and $p = 0.02$, respectively). Although ADC values measured with PGSE were also found to decrease after 24 hours, these variations were not found to be significant ($p = 0.13$). After 72 hours, both methods revealed significant decreases in ADC ($p < 0.05$ for both methods).

Histological examination of tissue sections provided additional insight into the pathophysiological mechanisms underlying these ADC variations. For example, area fractions of apoptic cells in treated animals were found to be higher than in controls at both 24 and 72 hours after treatment, yet these differences were found to be insignificant using a student t-test. The area fractions of proliferating cells were similar between groups after 24 hours, yet increased in treated animals to the level of statistical significance after 72 hours ($p = 0.004$). These results indicate that the antineoplastic effects of BCNU decreased the number of proliferating cells in treated animals, while the control animals experienced increasing tumor growth.

There was also a significant increase in extracellular space for both treated and control animals from the 24 hour to 72 hour time point. While mean area fractions of extracellular space were similar between groups after 24 hours, both groups showed an increase after 72 hours, though only the treated group showed a significant change ($p = 0.046$).

The most striking difference between groups was in the area fraction of hemotoxylin stained tissue. At both 24 hours and 72 hours following treatment, these area fractions were found to be significantly larger in treated animals than in controls. Furthermore, the ratio of hemotoxylin/eosin stained areas, which give some indication of the nuclear/cytoplasmic ratio, was also significantly different between groups at both time points, with the treated group displaying significantly larger values.

Given the insignificant difference in extracellular space found between treated and control animals after 24 hours, indicating little to no difference in cellularity between groups, these results indicate that OGSE methods may be capable of detecting changes in ADC resulting from chemotherapeutic effects on intracellular structure alone. This claim is further validated by the significant differences found in mean nuclear size and mean nuclear/cytoplasmic ratio between groups at this time point, contrasted with the insignificant differences found in the area fraction of apoptotic and proliferating cells between groups. Although further studies in other tumor models, and with other treatment methods, may be needed to further validate this finding, these studies have provided a first glimpse at the utility of OGSE techniques for detecting tumor response within 24 hours of treatment, and earlier than conventional DW-MRI methods.

In closing, the work outlined in this thesis has demonstrated the efficacy of oscillating gradient diffusion MRI techniques for evaluating variations in tissue microstructure that are obscured by conventionally employed techniques. Since these methods are sensitive to microscopic changes in tissue organization on an intracellular scale, these techniques provide additional insight into the pathophysiological factors influencing variations in ADC, such as those that occur following stroke, as well as those associated with tumor proliferation and/or response to therapy. While further work is needed, in other tissue models, as well as at higher oscillation frequencies, in order to explore the full utility of OGSE methods, the research described in this thesis has provided a solid

foundation for the application of these techniques to the study of biological tissue structure *in vivo*.